Power Converters for Piezoelectric and Pyroelectric Materials

Le Wang

Dissertation submitted to the faculty of the
Virginia Polytechnic Institute and State University
in partial fulfillment of the requirements for the degree of

Doctor of Philosophy
in Electrical Engineering

Rolando Burgos, Chair
Guo-Quan Lu
Dong Dong
Jaime De La Reelopez
Alfred L. Wicks

January 10, 2022
Blacksburg, Virginia

Keywords: Piezoelectric, pyroelectric, dc-dc converter

Power Converters for Piezoelectric and Pyroelectric Materials

Le Wang

Abstract

Dielectrics are materials that can be polarized by an applied electric field. As the essential property for dielectrics, the relationship between electric field and dielectric polarization, has been widely studied and used in the area of electrical engineering. Representative applications are insulators and electrical energy storage capacitors. For some types of dielectrics, the dielectric polarization is not only decided by the applied electric field, but also is affected by mechanical and thermal properties. This work studies the electro-mechanical and electro-thermal energy inter-conversions and proposes the design of power converters for these materials.

Piezoelectric effect is a cross-coupling between mechanical property and electrical property of dielectrics. It is a reversible process where external electric potential can generate internal mechanical force and vice versa. This effect is utilized to build a piezoelectric transformer (PT) by combining two sets of piezoelectric material together. One set is used as the input, to cause a geometric strain by applied electric field, while the other set is used as the output, to generate an electric charge by the coupled mechanical stress. Compared to traditional magnetic transformers, PTs store energy in mechanical inertia and compliance and therefore they do not generate electromagnetic noise. They are suitable for batch mass manufacturing since there is no winding requirement. Among many types of PTs, radial PT and Rosen-type PT are most widely used.

To provide a guide for the design of PT-based converters, the electrical characteristics of PTs are first analyzed. The accuracy and applicability of different levels of models of PTs are compared and discussed. The detailed universal attributes of PTs, which include the gain characteristic, the input impedance characteristic and the efficiency characteristic, are also derived. In addition, with the assistance of additional compensation component(s), PTs can provide better performance. The impacts of the input and output inductors and capacitors on gain and efficiency

characteristics of a PT are analyzed.

Tunable PT is a recently developed raidal PT with three ports: input, output, and control ports. When connected with different impedance at the control port, tunable PT has different voltage gain characteristics. It is proposed to use this property for output voltage regulation while keeping constant switching frequency to ensure high efficiency operation of the PT in PT-based power converters. A closed-loop control scheme is proposed, where the regulation is done by a duty cycle controlled switched capacitor at the tunable PT control port. Two types of output filter are also analyzed and compared. Dc-dc converters with power rating ranging from 30 W to 100 W are built to verify the proposed design.

Rosen-type PT features natural mechanisms for high transform ratio in a compact planar form, which provide an alternative solution for dc bus-fed high step-down voltage-ratio auxiliary power supplies in medium-/high-voltage systems without using bulky magnetic transformer with high turns numbers. The design procedure of the Rosen-type PT-based high step-down voltage-ratio dc-dc converter is presented. The proposed design is validated by a prototype with height of 1 cm, whose nominal output power is 5 W, input voltage ranges from 200 V to 1.5 kV, regulated output voltage is 5 V.

Pyroelectric effect is a reversible cross-coupling between thermal property and electrical property in some dielectrics. The pyroelectric effect refers to the polarization change caused by temperature change, while the reversed pyroelectric effect refers to a temperature change generated by a electric field change. The reversed pyroelectric effect can be used for building a environmentally friendly thermodynamic system. Electrical characterization of the pyroelectric material is executed to facilitate the design of the power converter needed in the corresponding thermodynamic system. Specifically, this work proposes an energy recovery circuit to increase the coefficient of performance of the system since during the thermodynamic cycle, part of the electrical driving work does not pump heat and may therefore be recovered. A prototype featuring 1 kV terminal voltages and providing 1.3 kW average recovering power is built and tested.

Power Converters for Piezoelectric and Pyroelectric Materials

Le Wang

General Audience Abstract

When a dielectric material is placed in an electric field, electric charges slightly shift from their average equilibrium positions, causing dielectric polarization. In the area of electromagnetism, dielectric material is widely used as an electrical insulator and to build capacitors. For some types of dielectrics, dielectric polarization is not only affected by electric field. Strong couplings between electrical and mechanical characteristics, and between electrical and thermal characteristic also exist and can be utilized in practical applications. Piezoelectric effect is a coupling between electrical and mechanical characteristics. It is a reversible process where external electric potential can generate internal mechanical force and vice versa. It can be utilized to build transformers, which do not require coil winding nor generate electromagnetic interference compared to their magnetic counterparts. This work analyzed the electrical characteristics of piezoelectric transformers and proposed the design of dc-dc converters based on different types of piezoelectric transformers for different applications, which include tunable radial piezoelectric transformer-based power converters and Rosen-type piezoelectric transformer-based step-down converter with high voltage conversion ratio. (Reversed) pyroelectric effect is a coupling between electrical and thermal characteristics in some dielectrics. An adiabatically applied or removal electric field results in an increase or decrease in the temperature of the corresponding material. This effect can be used to build a environmentally friendly thermodynamic system instead of the most prevalent vapor compression method which involves the use of hydro-fluorocarbon gases leading to global warming and ozone depletion. Electrical characterization is executed first to facilitate the design of the power converter needed by the thermodynamic system. In addition, during the thermal cycle, part of the work done to drive representative cycles does not pump heat and may therefore be recovered. This work proposed circuit featuring energy recovery to provide the desired electric field for driving the thermodynamic system and charge recycling to improve the system efficiency.

For My Parents, Yufu Wang and Xiuling Shan.

谨以此文献给我的父母, 王余富和单秀玲。

Acknowledgement

If life were a game, then personally speaking, my journey at Virginia Tech's Center for Power Electronics Systems (CPES) felt like a game level under "hard but safe" mode. This journey has been challenging for me in both aspects of work and life, whether it is learning, mastering and applying new academic knowledge and new engineering skills in a short period of time, or how to balance and manage life chores and work projects. However, when it comes to the end, I realize that even it is tough for me, I am "safe" at the same time. Of course, this does not mean that the academic committee would award me a Ph.D. degree no matter how badly my work is done. But I believe in my heart that no matter what happens, my life will go on well. There were many days in this journey when I was racing against various intertwined deadlines, and mentally I was like a cup placed on the edge of the table, feeling like it could fall at any moment. But I know, I wouldn't be shattered if I fell, because there is a high pile carpet under the desk. —And these rugs are made up of all kinds of company, encouragement, and help around me. Therefore, in this acknowledgment section, which is placed at the beginning of this dissertation, but is finished at the very end, I would like to sincerely thank the people who have supported, encouraged and helped me during this journey, and made me gradually realize that I am safe.

First of all, I would like to thank my advisor, Dr. Rolando Burgos, for providing me the opportunity to embark on this journey. Thanks for believing my words "I am relatively good at interdisciplinary study and will try my best" at the end of the year of 2016 and assigning me a series of interdisciplinary research topics for the next five years. At the very beginning, I always doubt whether my project "makes sense" since few people are spending effort on it. The first lesson that I learned from Dr. Burgos is that, it is my work to explore the meaning of this topic. "If you don't believe what you're doing is meaningful, how can you convince others that what you're doing is meaningful?" - This sentence is the starting point that I stopped swaying, calmed down and thought seriously about the project, which also runs through the entire process of completing the project. Compared with the serious

status of ”advisor”, Dr. Burgos is more like a comrade-in-arms who fights side by side with the students, and even goes all out more than the students. During the process of completing these topics, I have benefited a lot from Dr. Burgos, whether it is objective academic knowledge, research methods, or subjective research attitudes and work habits.

I am also grateful to my other committee members including Dr. Guo-Quan Lu, Dr. Dong Dong, Dr. Jaime De La Reelopez, and Dr. Alfred Wicks for their valuable comments and insightful suggestions. Thanks to Dr. Guo-Quan Lu for his guidance and suggestions in a respectful and gentle manner during each group meeting. Thanks to Dr. Dong Dong for willing to take the extra time to help me after the group meeting. Thanks to Dr. Jaime De La Reelopez and Dr. Alfred L. Wicks for acknowledging my work. Special thanks to Dr. Alfred L. Wicks for his corrections and suggestions in the field of mechanics. In addition, thanks to Dr. Khai Ngo for giving me guidance on the piezoelectric transformer topic. Also, I would like to thank Dr. Zhengming Zhao from Tsinghua University for guiding me into the world of power electronics and the guidance in the follow-up study process. I would like to thank Dr. Ian Galton from University of California San Diego for his guidance in my master's study. Although the content is not power electronics, the learning habits he taught me will benefit me for life.

I would like to thank CPES, an excellent research group, and every member who has created such a terrific learning and working environment: Dr. Fred Lee, Dr. Dushan Boroyevich, Dr. Qiang Li, Dr. Yuhao Zhang, Dr. Christina DiMarino, Dr. Igor Cvetkovic, Dr. Bo Wen, Dr. Boran Fan, Mr. David Gilham, Ms. Teresa Shaw, Ms. Trish Rose, Ms. Marianne Hawthorne, Ms. Na Ren, Ms. Yan Sun, Ms. Ling Li, Ms. Audri Cunningham, Ms. Linda Long, Mr. Matthew Scanland, Mr. Dennis Grove, Mr. Neil Croy, and all other CPES colleagues. Special thanks to Dr. Qiong Wang for his patient guidance and help when I first came to CPES. Special thanks to Dr. Keyao Sun for being my invisible mentoring senior after Dr. Qiong Wang left CPES. Thanks to Mr. Ahmed Nabih, Mr. Shuo Wang, and Mr. Cong Tu for their help in learning and designing planar transformers. Thanks to Mr. Xingchen Zhao, Mr. Jianghui Yu, and Dr. Boran Fan for their guidance in the

process of learning digital control. Thanks to Ms. Tianyu Zhao for her company. Thanks to Mr. Jian Liu, Mr. Yuliang Cao, Ms. Emma Raszmann, Mr. Xiang Lin, Dr. Yue Xu, Mr. Joshua Stewart, Dr. Slavko Mocevic, Ms. Ning Yan, Mr. Bo Li, Ms. Lakshmi Ravi, Mr. He Song, Mr. Nguyen Tam, Ms. Yu Rong, Mr. Vladimir Mitrovic, Dr. Zhengrong Huang, Dr. Ye Tang, Ms. Yingying Gui, Dr. Joseph Kozak, Dr. Zichen Miao, Dr. Lujie Zhang, Dr. Sungjae Ohn, Dr. Bingyao Sun, Dr. Junjie Feng, Dr. Chao Fei, Dr. Ting Ge, Dr. Zhengyang Liu, Dr. Chi Li, Mr. Ripun Phukan, Mr. Gibong Son, Dr. Jiewen Hu, Mr. Feng Jin, Ms. Qian Li, Mr. Zheqing Li, Mr. Boyan Wang, Mr. Ruizhe Zhang, Mr. Shengchang Lu, Mr. Feiyang Zhu, Mr. David Nam, Mr. Yinsong Cai and other colleagues who study with me.

With much love, I want to express sincere gratitude to my parents for their infinite tolerance, unconditional support and endless love. Their presence is my hardest armor in the face of all odds. I would like to thank my parents-in-law for their support for my choice to pursue a Ph.D. degree, and for pushing me forward when I was indecisive. Thanks to my son Yuanheng (Frank) Sun, who was born at the beginning of this journey, for his willingness to grow up with me together. I would like to thank my husband, Keyao Sun for accompanying me in my study and life since the beginning of the undergraduate studies. His doctoral dissertation title is *Protection, Control, and Auxiliary Power of Medium-Voltage High-Frequency SiC Devices*. Just like this topic, he gave me spiritual protection and urged me to learn how to self-manage and control. He is a crucial auxiliary power supply of my life :).

Furthermore, I would like to thank all the friends I met on douban.com for accompanying me in my spiritual world. Special thanks for encounter with Ms. Jessie Wang. She gave me great affirmation and encouragement of my personal value during the period when my will was the most depressed, like a pair of warm hands gently but powerfully grasping the sinking me.

Finally, I want to thank myself. Although I may not be able to have the label of "good at interdisciplinary learning" in the end, although it is a pity that due to various factors, I am not capable enough to be a student that makes my advisor

feel proud of, I am grateful that although I often say that I want to give up, I never really decide to quit, and as promised with my advisor at the very beginning of this journey, always try my best and go all out. - This paragraph has been revised by Dr. Rolando Burgos into: Finally, I want to thank myself, as I feel proud and grateful that although I often thought about giving up, I never did, and I kept the promise I made to my advisor at the very beginning of this journey, that I would always try my best and be all in, fully committed. And in the end, on his own words, he was: "very proud and grateful to have had the chance to work with you in all these highly interesting and challenging topics." - Please allow me to keep both original and revised versions. Thank you Dr. Burgos. I am much obliged for your recognition and encouragement.

Looking back at the whole path that I took, subjectively speaking, it was really a difficult road, and every second felt like that I would not be able to persist in the next second. Although it is a bit of a fuss to describe it like this, and from the perspective of others, I may have taken a lot of detours, I know that this is the only way for me. And on this road, if there is no support and help, maybe I can still go all the way, but it will no longer be in safe mode. Therefore, sincere thanks again to all people who have supported, encouraged and helped me during this journey.

致谢

如果将人生比作一场游戏，那么在 Virginia 理工大学电力电子中心（CPES）读博的这段经历对我个人而言则如同一段“安全的困难模式”下的关卡。在这段经历中，无论是在短时间内学习、掌握并且应用新的学术知识和新的工程技能，抑或是如何平衡并管理好生活琐事和工作项目，对我来说都是具有一定挑战性的。然而，随着时间的推移，在这段旅程即将结束的时候，我发现虽然身处困难模式（主观感受，并不一定客观），但同时我又是“安全”的。当然，这并不意味着无论我工作完成得有多糟糕，包括导师在内的学术委员会都会授予我博士学位（笑）。而是我在内心的深处相信，无论如何，我的人生都将好好地进行下去。这段旅程中，有很多日子我都在与各种交织在一起的截止日期赛跑，心理状态上我仿佛是一只被放置在桌子边缘的杯子，感觉随时都有掉下去的可能。旅程行将结束的时候，我意识到，即便掉下去也不会粉身碎骨，因为桌下铺着厚厚的地毯。——而这些地毯正由我身边的各种陪伴、鼓励与帮扶组成。因此，在这个虽然写在篇首、却是整本学位论文最终完成的致谢部分，我想由衷地感谢这段旅程中给予我支持、鼓励与帮助、让我逐渐意识到我很安全的人和事。

首先感谢我的导师 Dr. Rolando Burgos 给我提供了踏上这段旅程的机会。感谢在 2016 年年末，面对一个尚未受过完善的、系统的电力电子工程学的教育的我，他选择相信我所承诺的“我相对擅长跨学科学习并且会全力以赴”——然后在接下来的五年时间里给我布置了一系列的跨学科课题。在完成这些课题的过程起初，我经常质疑自己的课题是否“有意义”。Dr. Rolando Burgos 给我上的第一课就是让我明白，这些目前鲜有人问津的课题是否有意义、意义何在，需要我去探索、去发现。“如果你都不相信自己所做的事情是有意义的、那你又如何让别人相信你所做的是有意义的?”——这句话是我停止摇摆、沉下心来认真琢磨自己的课题的开始，也贯穿了整个课题完成的过程。比起“导师”这样严肃的身份，Dr. Rolando Burgos 更像是和学生们一起并肩作战、甚至比学生们更加全力以赴的战友。在完成这些课题的过程中，无论是客观的学术知识、科研方法，还是主观的科研态度、工作习惯，从 Dr. Rolando Burgos 那里我都获益良多。

其次感谢我的学术委员会中的其他所有教授：Dr. Guo-Quan Lu, Dr. Dong Dong, Dr. Jaime De La Reelopez, Dr. Alfred L. Wicks 在论文完成过程中给予我的指导与支持。感谢 Dr. Guo-Quan Lu 在每一次组会上以尊重和温和的方式给

我提的指导意见与建议。感谢 Dr. Dong Dong 愿意在组会后花费额外的时间给我提供指导。感谢 Dr. Jaime De La Reelopez 和 Dr. Alfred L. Wicks 对我的工作的肯定。尤其感谢 Dr. Alfred L. Wicks 在机械学领域给我提供的指正和建议。此外，感谢 Dr. Khai Ngo 对我的压电变压器感课题上给予我的指导。感谢清华大学 Dr. Zhengming Zhao 对我接触到电力电子工程学科的引导以及后续学习过程中的指导。感谢加州大学 San Diego 分校 Dr. Ian Galton 在我的硕士学习中给予我的帮助和指导，虽然学习内容并非电力电子，但是他所教予我的学习思路和习惯将使我终身受益。

再次，我想感谢 CPES 这个非常棒的科研团体，以及共同营造出这样的学习工作环境的每一位成员：Dr. Fred Lee, Dr. Dushan Boroyevich, Dr. Qiang Li, Dr. Yuhao Zhang, Dr. Christina DiMarino, Dr. Igor Cvetkovic, Dr. Bo Wen, Dr. Boran Fan，Mr. David Gilham, Ms. Teresa Shaw, Ms. Trish Rose, Ms. Marianne Hawthorne, Ms. Na Ren, Ms. Yan Sun, Ms. Ling Li, Ms. Audri Cunningham, Ms. Linda Long, Mr. Matthew Scanland, Mr. Dennis Grove，Mr. Neil Croy，以及 CPES 的所有同学。其中，特别感谢 Dr. Qiong Wang 前辈在我初来 CPES 时对我的耐心引导和帮助，特别感谢 Dr. Keyao Sun 在 Dr. Qiong Wang 离开 CPES 后成为我隐形的课题讨论对象和指导前辈，感谢 Mr. Ahmed Nabih、Mr. Shuo Wang 以及 Mr. Cong Tu 对我学习并设计平面变压器时的帮助，感谢 Mr. Xingchen Zhao, Mr. Jianghui Yu 以及 Dr. Boran Fan 对我学习数字控制过程中的指导，感谢 Ms. Tianyu Zhao 给予我的陪伴，感谢 Mr. Jian Liu，Mr. Yuliang Cao，Ms. Emma Raszmann，Mr. Xiang Lin，Dr. Yue Xu，Mr. Joshua Stewart，Dr. Slavko Mocevic, Ms. Ning Yan, Mr. Bo Li, Ms. Lakshmi Ravi, Mr. He Song, Mr. Nguyen Tam, Ms. Yu Rong, Mr. Vladimir Mitrovic，Dr. Zhengrong Huang, Dr. Ye Tang, Ms. Yingying Gui, Dr. Joseph Kozak, Dr. Zichen Miao, Dr. Lujie Zhang, Dr. Sungjae Ohn, Dr. Bingyao Sun, Dr. Junjie Feng, Dr. Chao Fei, Dr. Ting Ge, Dr. Zhengyang Liu, Dr. Chi Li, Mr. Ripun Phukan, Mr. Gibong Son, Dr. Jiewen Hu, Mr. Feng Jin, Ms. Qian Li, Mr. Zheqing Li, Mr. Boyan Wang, Mr. Ruizhe Zhang, Mr. Shengchang Lu, Mr. Feiyang Zhu, Mr. David Nam 以及 Mr. Yinsong Cai 等各位与我共同学习的同学同事。

另外，衷心感谢我的家人。感谢我的父母对我的无限包容、无条件支持和无尽的爱。他们的存在是我面对所有困难时最坚硬的铠甲。感谢我的公公婆婆对我

选择读博的支持，感谢婆婆在我犹豫不决时推我向前一步。感谢元衡，他出生于我读博旅程的开始，感谢他愿意和我一起成长。感谢我的丈夫孙可尧同学在自本科始的整个大学学习生涯中给予我的学习与生活上的陪伴。他的博士论文课题是 Protection, Control, and Auxiliary Power of Medium-Voltage High-Frequency SiC Devices，正如这个课题一样，他给予了我精神上的保护、敦促我自我管理与控制，是我人生里及其重要的辅助电源（笑）。

再者，感谢在豆瓣网站上认识的（包括现实生活中已经认识但又在豆瓣上再一次认识的）各位友邻在我精神世界里给予我的陪伴。其中特别感谢与 Ms. Jessie Wang 的相遇。她在我意志最为消沉的一段时期给予了我个人价值的极大肯定和鼓励，如同一双温暖的手柔和却又有力地捞住了下沉的我。

最后，我想要感谢自己。虽然最终我也许并不能拥有“擅长跨学科学习”的标签、虽然有些遗憾由于种种因素我并没有足够的能力成为令导师骄傲的学生，但是感谢自己虽然经常嘴上嚷嚷着要放弃但从未真正松手、一如当初和导师承诺的那样，一直全力以赴。——这篇论文提交前，我收到了导师 Dr. Burgos 对这段的修改：最后，我想要感谢自己，感谢自己虽然时常想要放弃但从未真正松手。我完全信守了我对导师的承诺，一直全力以赴。我为这样的自己感到骄傲。最后，用导师他自己的话说，“他为和我曾经共同完成这些非常有趣、挑战性的课题而感到自豪”。——请允许我保留原文和导师的修改稿。因为在这里我想再次感谢导师对我的认可和鼓励。

回头看整条读博所走的路，主观上来说实在有些筚路蓝缕艰苦卓绝、每一秒都觉得下一秒就无法坚持下去，却又神奇地每每绝处逢生柳暗花明。虽然对于旁人来说如此形容未免有些小题大做、从旁人的角度看我也许绕了很多弯路，但是我知道，这是我的必经之路。而这条路上，如果没有这些支持与帮助，也许我也可以走完全程，但那将不再是安全模式。因此，再次衷心感谢。

Contents

1 Introduction **1**

1.1 Electrical, Mechanical, and Thermal Energy Inter-Conversions in Dielectrics 1

1.2 Overview of the Piezoelectric Effect 5

1.3 Overview of the Pyroelectric Effect 11

1.4 Dissertation Outline 15

2 Working Principle and Electrical Characteristics of Piezoelectric Transformers (PTs) **19**

2.1 Introduction 19

2.2 Equivalent Circuit Models of PTs 24

2.3 Electrical Characteristics of PTs 28

2.3.1 Input-to-Output Voltage Gain 30

2.3.2 Input Impedance 32

2.3.3 Efficiency 33

2.3.4 Experimental Measurement 33

2.4 Impacts of Compensation Networks on Characteristics of PTs . . . 36

2.4.1 Impacts of the Series Output Compensation Inductor L_{os} . . 36

2.4.2 Impacts of the Parallel Output Compensation Inductor L_{op} 37

2.4.3 Impacts of the Extra Output Capacitor C_{oext} 40

2.4.4 Impacts of Input Inductors L_{ins} and L_{inp} and the Extra Capacitor C_{inext} 41

2.4.5 Application Example: LCCL Compensation 43

2.5 Summary and Conclusion 46

3 Tunable Radial PT-Based Power Converter 49

3.1 Introduction 49

3.2 Working Principle and Electrical Characteristics of Tunable Radial PT 51

3.2.1 Structure and Equivalent Circuit 51

3.2.2 Electrical Characteristics 52

3.3 Design and Control of Tunable Radial PT-Based Power Converter . 58

3.3.1 Input Side Design 58

3.3.2 Output Side Design 59

3.3.3 Control Side Design 66

3.4 Experimental Results 68

3.5 Conclusion 69

4 Rosen-type PT-Based High Step-Down Voltage-Ratio Dc-dc Converter 73

4.1 Introduction 73

4.2 Design Procedure 76

4.2.1 Selection of Compensation Network and Operation Frequency 77

4.2.2 Selection of Input Dc-ac Stage 79

4.2.3 Selection of Output Ac-dc Stage 80

4.2.4 Design Criteria of 1:1 Transformer 81

4.3 Experimental Results 82

4.4 Conclusion 87

5 Power Converter for the Reversed Pyroelectric Thermodynamic Systems **89**

5.1 Introduction 89

5.2 Electrical Characterization of the Material in Reversed Pyroelectric Effect 96

5.3 Design of the Power Converter for the Thermodynamic System . . . 102

5.3.1 Design and Operation of the Power Stage 102

5.3.2 Design of the Control 109

5.4 Experimental Results 112

5.5 Conclusion 113

6 Conclusions and Outlook **119**

6.1 Conclusion 119

6.2 Potential Future Work 121

Bibliography **123**

List of Figures

1.1 Electric field and polarization of a dielectric. 2

1.2 Centrosymmetric and non-centrosymmetric crystal structures with applied deformation. 2

1.3 Relation between piezo-, pyro- and ferroelectric point groups. . . . 3

1.4 Cross-couplings between electrical, mechanical and thermal properties of non-centrosymmetric crystals. 4

1.5 Poling process. 6

1.6 Representation of directions of mechanical and electric forces. . . . 8

1.7 Model of transverse and longitudinal piezoelectric elements. (At equilibrium, $F_1 = F_2$.) 10

1.8 Representation of the reversed pyroelectric cycle. 13

1.9 Comparison of different types of thermodynamic systems. 14

2.1 Different types of PTs. 23

2.2 General block-diagram of the behavior model of PTs. 24

2.3 Derivation of the equivalent circuit model of a single-layer Rosen-type PT. 25

2.4 Equivalent circuit model of a radial mode PT. 27

2.5 Equivalent circuit model of a radial mode PT. 27

2.6 Model of PTs with harmonic components considered. 29

2.7 Voltage gain, input impedance and efficiency characteristics of sample Rosen-type PT in step-down configuration: blue - behavior model circuit without any loss resistance; red - circuit model with only mechanical loss resistance; green - complete circuit model with both mechanical and dielectric loss resistances. 30

2.8 Gain curves of the sample PT under different load conditions. . . . 32

2.9 Test boards of PT in (a) step-up and (b) step-down configurations. 34

2.10 Impedance curves of PT in (a) step-up and (b) step-down configurations. 35

2.11 PT with possible compensation networks. 36

2.12 Normalized gain, input impedance and efficiency surfaces under different series output inductor L_{os}. 38

2.13 Normalized gain, input impedance and efficiency surfaces under different parallel output inductor L_{op}. 39

2.14 Normalized gain curve for $\omega^2 = L_{\text{op}}C_{\text{o}} = LC$. 40

2.15 Normalized gain and input impedance phase surfaces under different series input inductor L_{ins}. 41

2.16 Normalized gain and input impedance phase surfaces under different parallel input inductor L_{inp}. 42

2.17 Normalized gain surfaces under different C_{inext}: (a) $L_{\text{inp}} = \infty, C_{\text{inext}} = 0, L_{\text{ins}} = \frac{1}{\omega^2(C_{\text{inext}}+C_{\text{in}})}$, (b) $L_{\text{inp}} = \infty, C_{\text{inext}} = 5C_{\text{in}}, L_{\text{ins}} = \frac{1}{\omega^2(C_{\text{inext}}+C_{\text{in}})}$, and (c) $L_{\text{inp}} = \infty, C_{\text{inext}} = 10C_{\text{in}}, L_{\text{ins}} = \frac{1}{\omega^2(C_{\text{inext}}+C_{\text{in}})}$. 42

2.18 (a) LC tank and (b) CL tank. 43

2.19 Normalized gain and input impedance phase surfaces under different parallel input inductor L_{inp}. 44

2.20 Effects of nonidealities on the characteristics of LC tank under resonance. 45

2.21 Effects of nonidealities on the characteristics of CL tank under resonance. 46

3.1 Different control schemes of PT-based converter. 50

3.2 Structure and equivalent circuit model of the radial mode PT. . . . 53

3.3 Structure and equivalent circuit model of the tunable radial mode PT. 54

3.4 Equivalent circuits of the tunable radial mode PT. 55

3.5 Voltage gain of the sample tunable PT with different load resistance and control capacitance. 57

3.6 Voltage gain versus C_{ctrl} at fixed operation frequency and load resistance. 57

3.7 Overall block-diagram of the proposed tunable PT-based dc-dc converter. 58

3.8 Output side design with (a) Capacitvie filter, (b) DC output inductor, and (c) AC output inductor. 60

3.9 Tunable PT-based dc-dc converter with dc output inductor. 61

3.10 Normalized open-loop input-to-output voltage gain of power stage of design with dc output inductor. 62

3.11 Tunable PT-based dc-dc converter with ac output inductor. 64

3.12 Comparison of designs with dc and ac output inductors. 65

3.13 Implementation and instruction waveforms of duty cycle controlled switched capacitor. 67

3.14 Bode plots of (a) Open-loop and (b) closed-loop control-to-output gain. 67

3.15 Implementation of the control feedback loop. 68

3.16 Test board. 69

3.17 Experimental Waveforms. 70

3.18 Measured efficiency comparison. 71

4.1 High step-down voltage-ratio solution examples in previous literature. 75

4.2 Block diagram of proposed Rosen-type PT-based high input voltage, high step-down voltage-ratio dc-dc converter. 77

4.3 PT output power vs. equivalent load resistance. 80

4.4 Impacts of parameters of 1:1 planar transformer. 83

4.5 Schematic and prototype photo of proposed Rosen-type PT-based high step-down voltage-ratio dc-dc converter. 84

4.6 Customized 1:1 planar PCB winding transformer. 85

4.7 Operational waveforms of proposed converter. 86

4.8 Output voltage regulation under 350 V and 1 kV bus voltages. . . . 87

4.9 Dc bus voltage range with regulated output for different load conditions. 87

4.10 Overall efficiency under 1 kV bus voltage. 87

4.11 Working continuously at nominal 1 kV input, 5 W output at room temperature. 88

5.1 Active regenerator cycle with fluid regenerator. 95

5.2 Voltage profile of dual module system. 95

5.3 Drive circuit of the sample pyroelectric film. 97

5.4 Origin Sawyer-Tower circuit. 98

5.5 Measurement circuit of the sample pyroelectric film. 99

5.6 The behavior of the reversed pyroelectric material in the Brayton cycle. 100

5.7 Proposed equivalent circuit model of the material in the reversed pyroelectric Brayton cycle. 100

5.8 Measured voltage and current of the sample film in one Brayton cycle. 101

5.9 Power stage of proposed power converter for the thermodynamic system. 103

5.10 Operation of the power stage. 104

5.11 Simulated waveforms during initial charge step. 105

5.12 Simulated waveforms during heat transfer step. 107

5.13 Simulated waveforms during charge transfer step. 108

5.14 Control scheme of the proposed converter. 110

5.15 Circuit of analog control path. 111

5.16 Prototype of the proposed power converter: (a) overall converter and (b) lateral board (left: front side; right: back side). 114

5.17 Experimental waveforms. 115

5.18 Thermal picture under steady state wich charge-recycling power at 1.2 kW. 116

5.19 Loss breakdown of charge-recycling buck-boost at 1.2 kW. 116

List of Tables

2.1 Parameters of the sample PT used in this work. 29

2.2 Simulation vs. calculation results of characteristic gain points of the sample PT with $R_o = 30\,\Omega$. 32

3.1 Parameters of the sample tunable PT used in this work. 56

3.2 Lightest Load vs.Dc Output Inductance. 62

3.3 Comparison of designs with dc and ac output inductors. 66

3.4 Comparison of converter specifications. 69

Nomenclature

Electrical

ε_{e}	Absolute permittivity
D	Electric displacement
E	Electric field
I	Current
P	Electric polarization
q	Electric charge
V	Voltage

Mechanical

σ	Stress
Υ	Elastic modulus
ε_{m}	Strain
d	Piezoelectric constant
F	Force
k	Electromechanical coupling coefficient
s	Elastic compliance

Thermal

C	Heat capacity
Q	Heat

S Entropy

T Temperature

Others

ρ Mass density

Z Mechanical or electrical impedance

Chapter 1

Introduction

1.1 Electrical, Mechanical, and Thermal Energy Inter-Conversions in Dielectrics

A dielectric, or dielectric material is an electrical insulator that can be polarized by an applied electric field. When a dielectric material is placed in an electric field, electric charges do not flow through the material as they do in an electrical conductor but only slightly shift from their average equilibrium positions causing dielectric polarization. Because of dielectric polarization, positive charges are displaced in the direction of the field and negative charges shift in the direction opposite to the field. This creates an internal electric field that reduces the overall field within the dielectric itself, as depicted in Fig. 1.1. As the essential property for dielectrics, this relationship between electric field and dielectric polarization, has been widely studied and used in electronic and electrical engineering, such as insulators and electrical energy storage capacitors. For example, for the application of capacitors, between two metal plates, if dielectric is inserted, because of dielectric polarization, for a given external electric field, more charges will accumulate on the metal plates, which means larger charge storage is achieved.

From crystallographic point of view, dielectrics can be crystalline or amorphous. For some types of crystalline dielectric material, the dielectric polarization is not only decided by the applied electric field, but can also be affected by mechanical and thermal properties. Piezoelectricity linearly relates an induced polarization to an applied stress, which means that piezoelectric material can generate electric charge

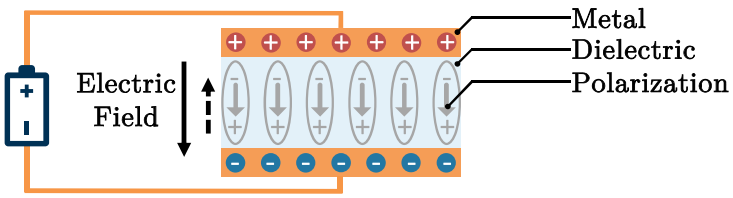

Figure 1.1: Electric field and polarization of a dielectric.

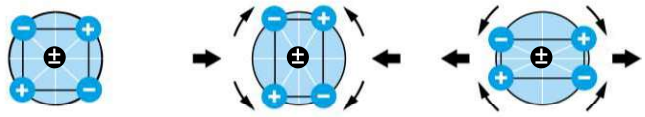

(a) Centrosymmetric.

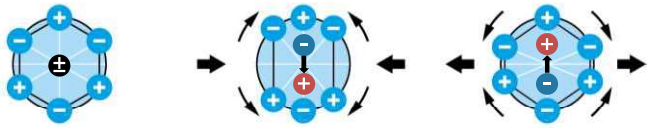

(b) Non-Centrosymmetric.

Figure 1.2: Centrosymmetric and non-centrosymmetric crystal structures with applied deformation.

proportional to the applied mechanical stress, or vice versa, which are referred as piezoelectric effect and inverse piezoelectric effect respectively. The pyroelectric effect is the change in polarization due to the change in temperature. The physical inverse of the pyroelectric effect describes a temperature or entropy change under externally applied electric field.

A non-centrosymmetric crystal structure (including those whose inversion symmetry is broke by an applied direct electric field or applied asymmetric electrodes [1]) is necessary for the existence of piezoelectric effect, as well as the pyroelectric effect and the reversed pyroelectric effect. Because for centrosymmetric structures, the positive charges and negative charges always cancel each other and the resultant charge is null no matter what the deformation is, as shown in Fig. 1.2a. While when

non-centrosymmetric crystals, for example, are compressed, the negative charge center moves up and the positive charge center moves down, as shown in Fig. 1.2b. This creates an accumulation of positive charges on one face and an accumulation of negative charges on the other face, which gives rise to a dipole moment. Therefore, the polarization, which is defined as the dipole moment per unit volume, is coupled with the stress.

Generally, there are 230 space groups among which 32 crystalline classes can be found in crystals. As summarized in [2, 3], also shown in Fig. 1.3, of the 32 crystallographic point groups, only 21 are non-centrosymmetric. Odd-rank tensor properties are symmetry forbidden in centrosymmetric structures, making piezoelectricity a null property for such materials. In the same way, in point group 432, the combination of symmetry elements eliminates piezoelectricity. The remaining 20 point groups are potentially piezoelectric. Of these 20 point groups, ten are polar, that is, they have a vector direction in the material that is not symmetry-related to other directions. Such materials can have a spontaneous polarization, which is typically a function of temperature. Thus, these materials are pyroelectric. Ferroelectric materials are a subset of pyroelectric materials in which the spontaneous polarization can be reoriented between crystallographically-defined directions by a realizable electric field.

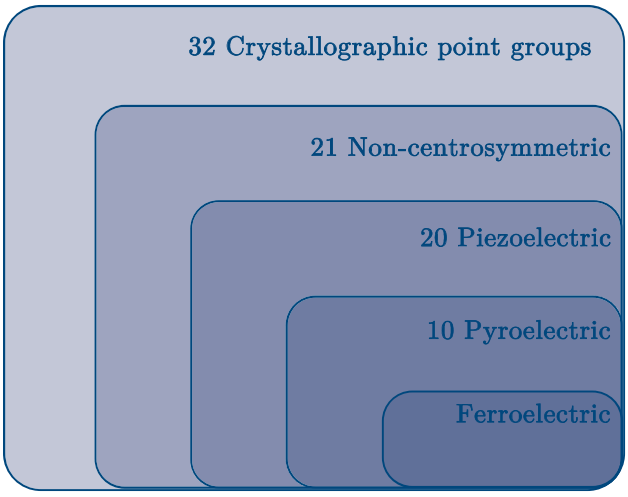

Figure 1.3: Relation between piezo-, pyro- and ferroelectric point groups.

Fig. 1.4 displays the cross-couplings between electrical, mechanical and thermal properties of non-centrosymmetric crystals. Piezoeletric effect and converse piezoelectric effect can be used to build sensors, generators, actuators, and transducers and are widely used in applications such as mechanical energy harvesting, crystal oscillators, ultrasonic devices, high voltage gas igniters, and so on. Pyroelectric effect is used for heat sensing, thermal energy harvesting, and nuclear fusion. The reversed pyroelectric effect can provide environmentally friendly thermodynamic system solutions without the use of greenhouse gas. Detailed description of these cross-couplings as well as their applications are presented in the following sections.

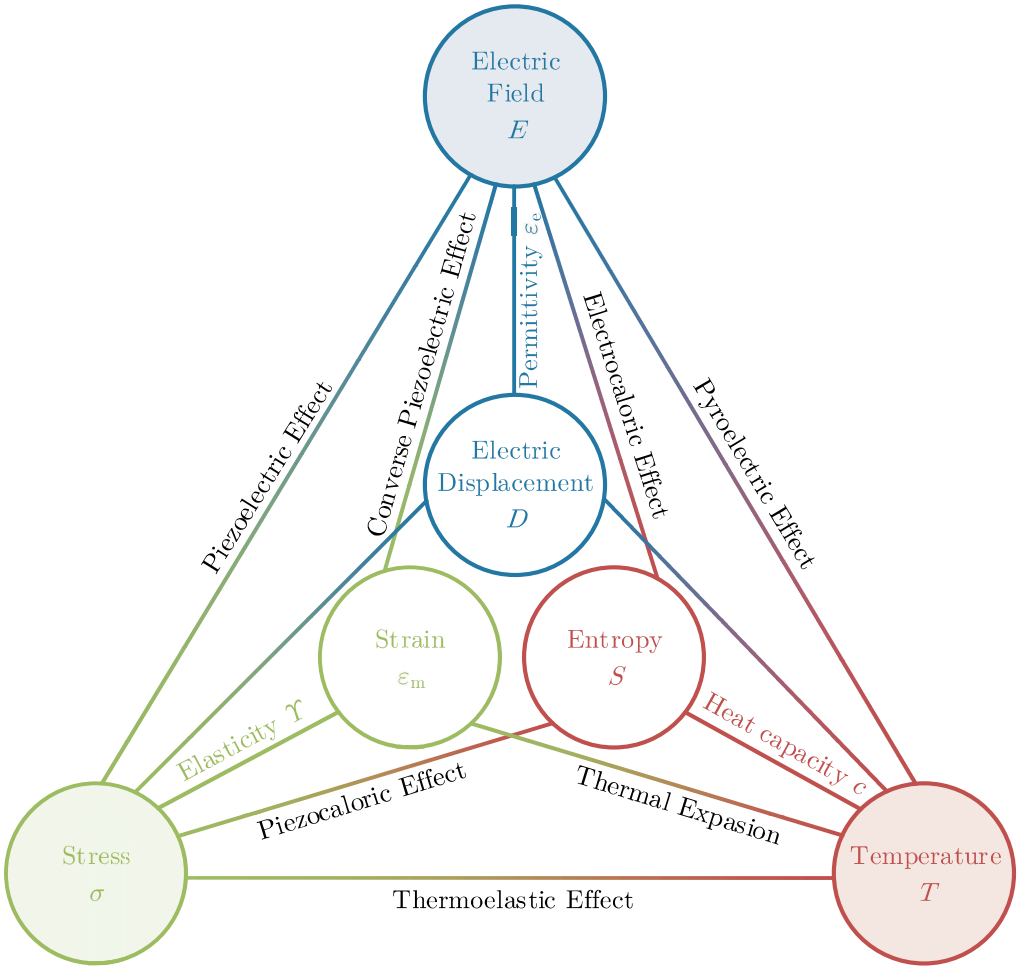

Figure 1.4: Cross-couplings between electrical, mechanical and thermal properties of non-centrosymmetric crystals.

In summary, cross-couplings between the electrical, mechanical, and thermal parameters in dielectrics create novel phenomena and bring benefits in many practical applications. Therefore, interdisciplinary studies and researches are necessary to take advantages of these phenomena, which are the motivation of this work. Especially, this work focuses on the electrical applications of piezoelectric and the reversed pyroelectric effects.

1.2 Overview of the Piezoelectric Effect

Piezoelectricity is the ability of certain crystalline materials to develop an electric charge proportional to a mechanical stress [4]. It also shows the converse, a geometric strain proportional to an applied voltage. By attaching electrodes to the appropriate surfaces of the piezoelectric material, piezoelectric elements can be retrieved.

As stated in Section 1.1, a non-centrosymmetric crystal structure is necessary for the existence of piezoelectric effect. In this way, when the pressure is applied, a charge will be generated along the principal direction. This characteristic is inherent for piezoelectric monocrystal. However, for polycrystal, because of the random orentation of crystallites, the net charge is zero. To offer piezoelectric properties more or less permanently, a process called poling is needed, in which a strong electric field is temporarily applied on the isotropic polycrystal. Fig. 1.5 presents the poling process. Prior to poling, the polar domains are randomly oriented. By being exposed to a strong, direct current electric field, usually, but not exclusively, at a temperature slightly below the Curie point, according to [5], domains most nearly align with the applied electric field if it is a ferroelectric polycrystal. As stated in Section 1.1, in ferroelectric materials, spontaneous polarization can be reversed by the application of an external electric field. After the electric field is removed, most of the dipoles are locked into this configuration of near alignment. This gives the material a permanent polarization, which is called the remnant polarization, and a permanent deformation that make it now anisotropic.

For ordinary solids, a stress σ merely causes a proportional strain ε_{m}, related

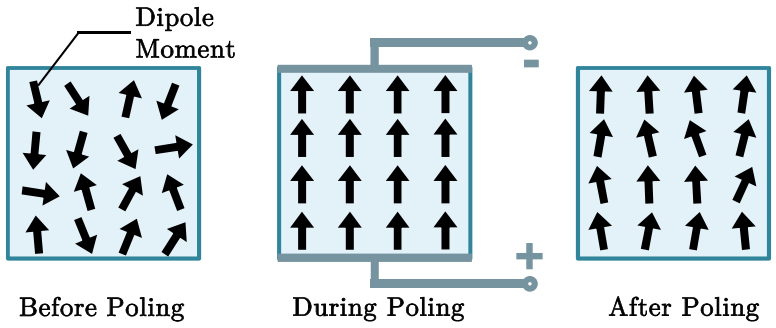

Figure 1.5: Poling process.

by the modulus of elasticity, that is $\varepsilon_{\mathrm{m}} = s\sigma$, where s is the inverse of the elastic modulus Υ, also called as elastic compliance. Similarly, for ordinary dielectrics, an applied electric field E merely causes a proportional electric displacement D, if it is linear, homogeneous, isotropic dielectric with instantaneous response to changes in the electric field, which is the simplest example, related by the permittivity, that is $D = \varepsilon_{\mathrm{e}} E$, where ε_{e} is the absolute permittivity.

For the direct piezoelectric effect, piezoelectricity contributes additional electric charge by the applied stress, with polarity depends on whether it is compression or tension, that is $D = d\sigma$, where D, the electric displacement, is defined as charge per unit area, and the proportionality constant d is expressed in coulombs/newton. Similarly, an applied electric field produces a proportional strain, expansion or contraction depending on polarity, that is $\varepsilon_{\mathrm{m}} = dE$, where d is expressed in meters/volt. For both effects, the proportionality constant d, which is also called as piezoelectric constant, is numerically identical for both direct and converse effects, that is $d = D/\sigma = \varepsilon_{\mathrm{m}}/E$. To be more rigorous, it is defined as partial derivative evaluated at constant stress (subscript σ) or constant electric field (subscript E), which is

$$d = (\frac{\partial \varepsilon_{\mathrm{m}}}{\partial E})_{\sigma} = (\frac{\partial D}{\partial \sigma})_{\mathrm{E}}. \tag{1.1}$$

The equations of state relating the electric and elastic variables can be written in a

general form as

$$D = d\sigma + \varepsilon_{\mathrm{e}}^{\sigma} E,$$

$$\varepsilon_{\mathrm{m}} = s^{\mathrm{E}}\sigma + dE, \tag{1.2}$$

where $\varepsilon_{\mathrm{e}}^{\sigma}$ is the permittivity at constant stress and s^{E} is the elastic compliance in constant electric field.

The single measurement of the coupling strength of a piezoelectric effect is the electromechanical coupling coefficient, which measures the fraction of the mechanical energy converted to the electrical energy or vice versa. The relationship is usually expressed in terms of k^2:

$$k^2 = \frac{\text{mechanical energy converted to electrical energy}}{\text{input mechanical energy}}$$

or

$$k^2 = \frac{\text{electrical energy converted to mechanical energy}}{\text{input electrical energy}}. \tag{1.3}$$

For example, a latest work [6] shows a 0.73 electromechanical coupling coefficient in the lead zirconate titanate type material.

In addition, the elastic, dielectric, and piezoelectric constants may differ along different axes in ceramics and crystals. Characteristics of the piezoelectric elements depend on the direction of the applied electric field, displacement, stress, and strain. The direction of positive polarization usually is made to coincide with the Z-axis of a rectangular system of X, Y, and Z axis. Direction X, Y, or Z is represented by the subscript 1, 2, or 3, respectively, and shear about one of these axes is represented by the subscript 4, 5, or 6, respectively, as displayed in Fig. 1.6. Subscripts of the constants are used to indicate direction. For example, k_{33} is the electromechanical coupling factor for both electric field and vibrations in direction 3. k_{31} is the electromechanical coupling factor for vibrations in direction 1 (electric field is always marked as 3). In addition, k_{t} is used to represent the factor for both electric field and vibrations in direction 3 but whose surface dimensions are large relative to thickness, which is smaller as k_{33}. And k_{p} is used to represent the factor for radial vibrations in direction 1 and 2.

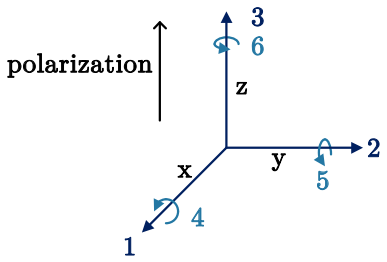

* Will be referred by Fig. 1.7.

Figure 1.6: Representation of directions of mechanical and electric forces.

The rigorous derivation of the model of the piezoelectric elements can be found in many references [7–10]. In general, any piezoelectric element can be modeled as electrical port(s) coupled with mechanical port(s). Fig. 1.7 shows the models of two basic piezoelectric element as the example. In Fig. 1.7, V is applied voltage, I is the current, F represents force, v represents velocity, l, w, and h are dimensions of length, width, and height respectively, $Z_{\mathrm{E}}^{\mathrm{LC}}$ is electrical clamped impedance, Z_0 is mechanical characteristic impedance, β is wavenumber and ϕ represents the electromechanical coupling. Fig. 1.7a is the model for the piezoelectric element whose strain (or stress) is in direction 2 (or direction 1). In Fig. 1.7a,

$$
\begin{aligned}
Z_{\mathrm{E}}^{\mathrm{LC}} &= \frac{1}{j\omega} \cdot \frac{h}{wl\varepsilon_{\mathrm{e33}}^{\sigma}(1-k_{31}^2)}, \\
k_{31}^2 &= \frac{d_{31}^2 \Upsilon_1^{\mathrm{E}}}{\varepsilon_{\mathrm{e33}}^{\sigma}}, \\
\beta &= \omega\sqrt{\frac{\rho}{\Upsilon_1^{\mathrm{E}}}}, \\
Z_0 &= wh\sqrt{\rho\Upsilon_1^{\mathrm{E}}}, \\
\phi &= wd_{31}\Upsilon_1^{\mathrm{E}}.
\end{aligned}
\tag{1.4}
$$

Fig. 1.7b is the model for the piezoelectric element whose pstrain (or stress) is in direction 3. In Fig. 1.7b,

$$
Z_{\mathrm{E}}^{\mathrm{LC}} = \frac{1}{j\omega} \cdot \frac{l}{wh\varepsilon_{\mathrm{e33}}^{\sigma}(1-k_{33}^2)},
$$

$$
\begin{aligned}
k_{33}^2 &= \frac{d_{33}^2 \Upsilon_3^{\mathrm{E}}}{\varepsilon_{\mathrm{e}33}^{\sigma}}, \\
\beta &= \omega \sqrt{\frac{\rho}{\Upsilon_3^{\mathrm{E}}}}, \\
Z_0 &= wh\sqrt{\rho \Upsilon_3^{\mathrm{E}}}, \\
\phi &= w\frac{h}{l} d_{33} \Upsilon_3^{\mathrm{E}}.
\end{aligned} \tag{1.5}
$$

Ideally a piezoelectric system can be constructed for any application for which any other type of electromechanical transducer can be used. For any particular application, however, limiting factors include the size, weight, and cost of the piezoelectric system.

The direct piezoelectric effect can be utilized to construct piezo-generators, piezo-sensors. Piezo-generators can generate voltages sufficient to spark across an electrode gap when mechanically activated with pressure or vibration, and thus can be used as ignitors in fuel lighters, gas stoves, welding equipment, and other such apparatuses [11, 12]. In addition, piezoelectric genertors are widely used in mechanical energy harvesting applications [13]. A piezoelectric sensor converts a physical parameter, such as acceleration or pressure, into an electrical signal, and thus can be used for Flow sensors and flow meters, thickness gages, accelerometers, hydrophones, microphones, and so on [14].

The converse piezoelectric effect can be used to construct piezo-actuators and piezo-transducers. A piezo-actuator converts an electrical signal into a precisely controlled physical displacement, to finely adjust precision machining tools, lenses, or mirrors. Due to the advantages of small size, simple design, high reliability and independence of lubrication, various piezo-actuators are implemented, for example, loudspeakers, hydraulic valves controllers, and special-purpose motors [15]. Piezo-transducers convert electrical energy into vibrational mechanical energy, often sound or ultrasound, that is used for cleaning, atomizing liquids, drilling or milling ceramics or other difficult materials, welding plastics, medical diagnostics, or for other purposes [16].

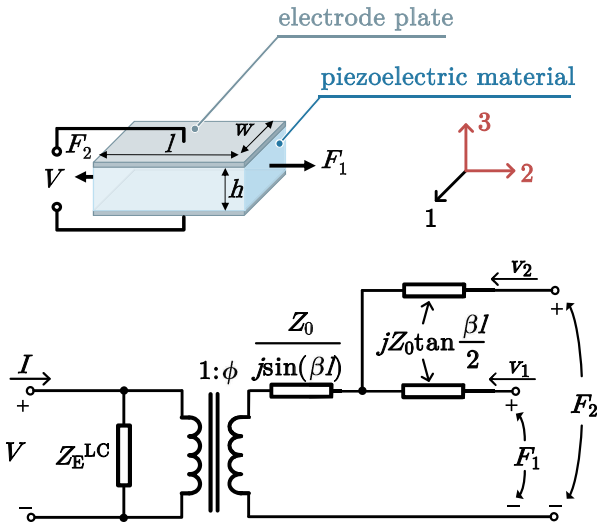

(a) Transverse piezoelectric element.

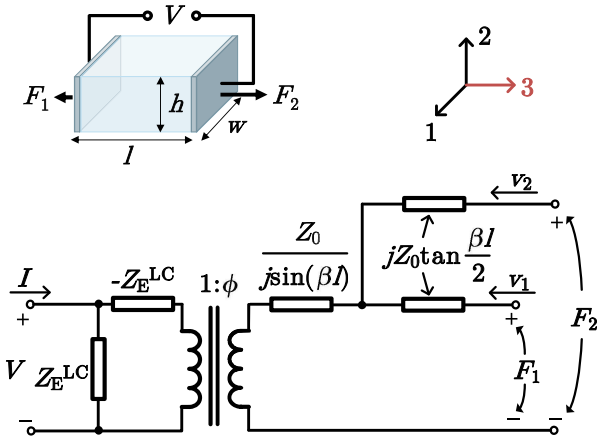

(b) Longitudinal piezoelectric element.

Figure 1.7: Model of transverse and longitudinal piezoelectric elements. (At equilibrium, $F_1 = F_2$.)

The direct and converse piezoelectric effects can be utilized simultaneously, for example, to build piezoelectric transformers (PTs). PTs are composed of two sets of piezoelectric elements. One set is used as the input, to build geometric stress by the applied voltage, while the other set is used as the output, to generate electric charge by the coupled mechanical stress. Different types of PTs can be manufactured by utilizing electro-mechanical coupling in different directions, which provide different advantages, which provide alternative or better solution for magnetic transformers in power converters. PTs have been widely used in different applications, such as ballast for fluorescent lamp [17], driver for light-emitting diodes or cold-cathode fluorescent lamps [18, 19], and adapter [20]. However, PTs have not been fully studied nor utilized yet, for example, lacking of the research on PTs with power higher than 20 W and in step-down voltage conversion applications. One of the objectives of this work is to explore and implement PT based applications which have not been fully studied.

1.3 Overview of the Pyroelectric Effect

Considering the crystal classes mentioned in Section 1.1, 20 classes can show piezoelectricity, among which 10 classes contain spontaneous polarization. In addition to piezoelectric charges resulting from stress, crystals from such classes can develop and electric charge when uniformly heated owing to change in magnitude of the spontaneous polarization with temperature. It should be noted that any piezoelectric crystal can develop an electric charge when non-uniformly heated solely as a result of the piezoelectric stresses created by thermal expansion if unconstrained. But for non-pyroelectric piezoelectric crystal, uniform heating is similar as uniform hydro-static stress, which will affect each direction equally, and the net charge will be zero.

Pyroelectric effect is the physically reversible. Pyroelectric effect is described as the ability of certain dielectric materials to generate a temporary voltage when they are heated or cooled while the reversed pyroelectric effect is a phenomenon in which a certain dielectric material shows a reversible temperature change under an applied

electric field. These two effects should not be confused with the thermoelectric effect, in which the electromotive force is developed across two points of an electrically conducting material when there is a temperature difference between them, and a temperature difference occurs when a current is driven through an electric junction with two dissimilar conductors. The term "thermoelectric effect" encompasses three separately identified effects: the Seebeck effect, Peltier effect, and Thomson effect. The Seebeck and Peltier effects are different manifestations of the same physical process and the Thomson effect is an extension of the Peltier–Seebeck model.

On the macroscopic scale, the phenomenological description of the reversed pyroelectric effect revolves around the entropy exchange between the two energy or entropy reservoirs, that is, dipolar and thermal entropy subsystems, enforced by the changes in the external electric field performed under adiabatic conditions. Specifically, variations in the electric field cause change of the dipolar state in a dielectric material, from the less ordered to a more ordered one, and vice versa, when an electric field is removed [21, 22]. Typical reversed pyroelectric cycle is displayed in Fig. 1.8, which is called as the Brayton cycle. From status 1 to status 2, a electrical field is applied to the material. If this change is performed on a time scale in which the heat flow from the material to the surrounding bath can be neglected, the change can be considered as adiabatic. Under this circumstance, the total entropy of the whole system remains constant as an adiabatic process. Therefore, this adiabatically applied electric field results in an increase in the temperature of the material due to the lattice vibration entropy compensation of the reduction of the dipolar subsystem entropy. From status 2 to status 3, heat is released due to the temperature difference. Correspondingly, the temperature of the material decreases, which leads to increased electric displacement. The reason for this increase is that lower temperature slows the motion of molecules and atoms and dipoles trend to align in the direction of the applied electric field, which therefore leads to higher polarization. In reverse, from status 3 to status 4, the adiabatic removal of the field causes cooling of the material; that is, the temperature of the material decreases as a result of the decrease of the lattice vibration entropy, which compensates for the increase of the dipolar subsystem entropy. Subsequently, the material will absorb

heat from the surrounding bath to be back to the origin state during the process from status 4 back to status 1. The suitability of the material for the thermodynamic system application is typically measured by the product of temperature change and entropy change [21].

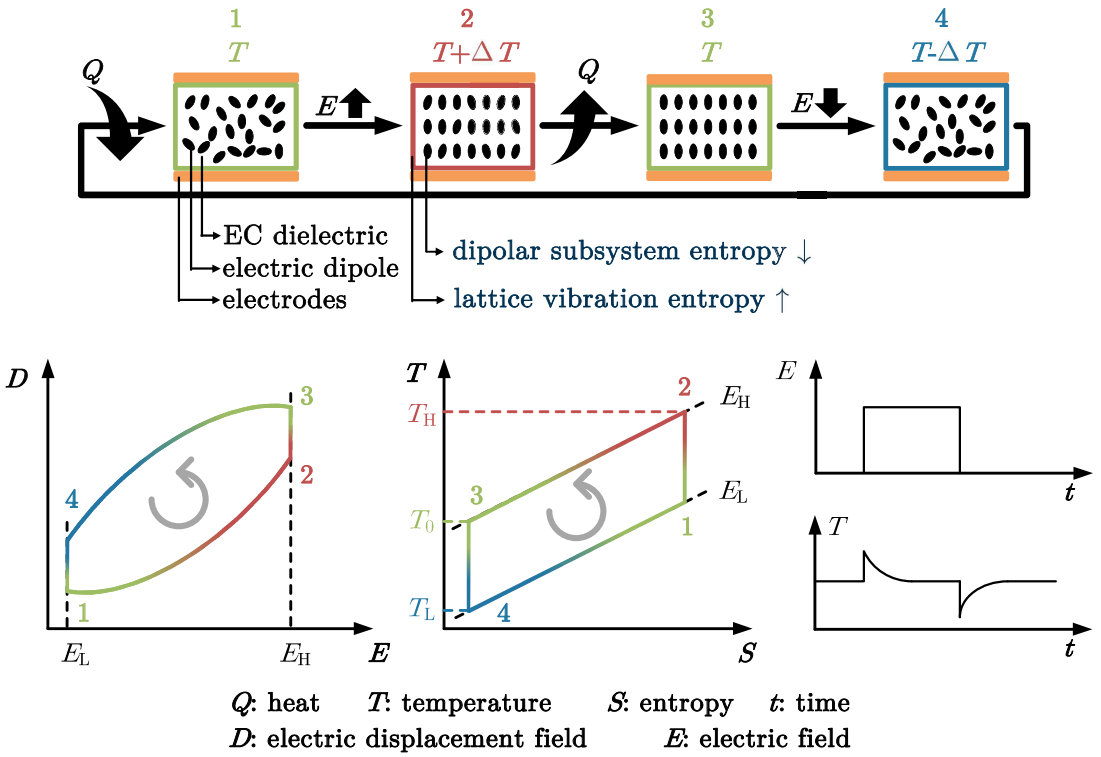

Figure 1.8: Representation of the reversed pyroelectric cycle.

Such reversed pyroelectric cycle is comparable to a corresponding thermodynamic cycle taking place in a classical compressor with a difference in coolant material and the field applied, which is depicted in Fig. 1.9. In traditional vapor-compression heating/cooling system, the heat transfer is realized based on the compression and expansion of the vapor. The vapor is compressed to a higher pressure, resulting a higher temperature. The heat is released due to the temperature difference. Similarly, the vapor is expended to a lower pressure and so a lower temperature and will absorb heat to go back to the origin state. This vapor compression method has been the most prevalent technology used in heating/cooling systems. However, the hydro-fluorocarbon gases used in this method come with the severe drawbacks of leading to global warming and ozone depletion [21, 23, 24]. Several non-vapor-

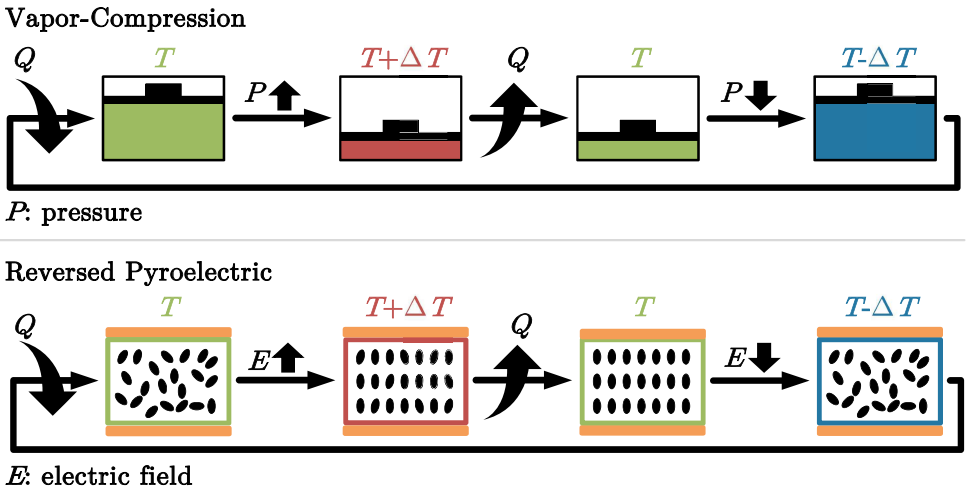

Figure 1.9: Comparison of different types of thermodynamic systems.

compression-based cooling technologies have been developed. External stimuli are utilized to heat or cool the materials, generating limited hysteresis energy loss and providing efficient and environmentally friendly solution. Among these techniques, the reversed pyroelectric technology has the advantages of high efficiency, direct electricity-utilization, low cost, and mature processes for mass production, benefited from its nature as an electricity-driven capacitor. Specifically, instead of gas, the pyroelectric polar material serves as the working coolant medium and instead of pressure, the electric field is used to change the state of the coolant material. For instance, the gas temperature change is achieved by changing the gas pressure in vapor-compression heating/cooling system. In contrast, the pyroelectric material temperature change is achieved by a change of the electric field. By doing so, an environmentally friendly thermodynamic system can be achieved.

During the reversed pyroelectric thermal cycle, according to [25], part of the work done to drive representative cycles does not pump heat, and may therefore be recovered to increase the coefficient of performance. This can also be found from Fig. 1.8. The electric energy absorbed by the material is proportional to the the

line integral of E with respect to D, which is

$$W_{\mathrm{E}} = \int_{\text{status 1}}^{\text{status 3}} V(t)I(t)\,\mathrm{d}t \;= \text{volume} \cdot \int_{\text{status 1}}^{\text{status 3}} E(t)\,\mathrm{d}D(t)\ . \tag{1.6}$$

Similarly, the electric energy released by the material is

$$W_{\mathrm{E}} = \text{volume} \cdot \int_{\text{status 3}}^{\text{status 1}} E(t)\,\mathrm{d}D(t)\ . \tag{1.7}$$

This portion of energy can be re-used to drive the next Brayton cycle with additional supplement energy. The other objective of this work is to design the power converter to drive the reversed pyroelectric thermodynamic cycle as well as recycle the electric energy for the corresponding thermodynamic system.

1.4 Dissertation Outline

In Chapter I, the research motivations and background are introduced. Dielectrics are materials that can be polarized by an applied electric field. As the essential property for dielectrics, the relationship between electric field and dielectric polarization, has been widely studied and used in electronic engineering and electrical engineering, such as insulators and electrical energy storage capacitors. For some types of dielectrics, the dielectric polarization is not only affected by he applied electric field, but also is influenced by mechanical and thermal properties. This work studies the electromechanical and electrothermal energy inter-conversions and proposes the design of power converters for these materials.

In Chapter II, the electrical characteristics of PTs are analyzed. The accuracy and applicability of different levels of models of PTs are compared and discussed. The detailed universal attributes of PTs, which include gain, input impedance, and efficiency characteristics, are also derived. In addition, with the assistance of additional compensation component(s), PTs can provide better performance. The impacts of the input and output inductors and capacitors on gain and efficiency characteristics of a PT are analyzed.

In Chapter III, the design of tunable PT-based power converter is presented.

Tunable PT is a recently developed raidal PT with three ports: input, output and control ports. When connected with different impedance at the control port, it has different voltage gain characteristics. It is proposed to use this property for output voltage regulation while keeping constant switching frequency to ensure high efficiency operation of the PT in PT-based power converters. A closed-loop control scheme is proposed, where the regulation is done by a duty cycle controlled switched capacitor at the tunable PT control port. Two types of output filter are also analyzed and compared. Dc-dc converters with power rating ranging from 30 W to 100 W are built to verify the proposed design.

In Chapter IV, Rosen PT-based high step-down voltage-ratio dc-dc converter is designed. Rosen PT features natural mechanisms for high transform ratio in a compact planar form, which provide an alternative solution for dc bus-fed high step-down voltage-ratio auxiliary power supplies in medium-/high-voltage systems, i.e., power electronics building blocks and renewable energy applications, without using bulky magnetic transformer with high turns numbers. The design procedure of the Rosen PT-based high step-down voltage-ratio dc-dc converter is presented. To verify the design, a planar prototype with 10 mm height, 5 W full output power, 200 V to 1.5 kV input voltage, and 5 V regulated output voltage is built and tested.

In Chapter V, the power converter, providing desired driving electric field and charge recycling, for reversed pyroelectric effect based thermodynamic system is proposed. Electrical characterization of the corresponding dielectric material is firstly executed to facilitate the design. A bi-directional buck-boost stage is used to complete the charge recycling, with two capacitor banks, the pyroelectric material connected to the two ports of the buck-boost stage. A front-end boost converter with precharge function is connected across the stacked capacitor banks to provide the initial charge as well as the supplementary charge. The controls for these two stages are independent of each other so that out of phase voltages of these two capacitor banks can be achieved with neglectable distortions. A prototype featuring 1 kV terminal voltages and providing 1.3 kW average recovering power is built and tested.

In Chapter VI, the dissertation is summarized and concluded, and some research topics are provided as the future work.

Chapter 2

Working Principle and Electrical Characteristics of Piezoelectric Transformers (PTs)

2.1 Introduction

As stated in Chapter 1, piezoelectric material is a type of dielectrics that exhibits electro-mechanical coupling. It can generate electric charge proportional to the applied mechanical stress, or vice versa, which are referred as piezoelectric effect and converse piezoelectric effect respectively. If two sets of piezoelectric material are built such that one set is used as the input, to build geometric stress by the applied voltage, and the other set is used as the output, to generate electric charge by the coupled mechanical stress, a PT can be built. The concept of the PT was firstly proposed by Alexander McLean Nicolson in 1931 even with limited applicability due to the piezoelectric material with limited performance [26]. And the first invention on PTs has been traditionally associated withe the patent of Charles A. Rosen in 1958 [27]. Since then, many PTs with different structures haven been proposed. Fig. 2.1 lists several main types of PTs, which are categorized by the vibration mode.

- Longitudinal mode PT (see Fig. 2.1a to Fig. 2.1c)

  Longitudinal mode PTs vibrate along the length direction. They are usually

in a shape of rectangular cuboids, whose length are considerably larger than the width and thickness.

- Rosen-type PT [9, 27–43] (see Fig. 2.1a)

  Rosen-type PTs have one section where the directions of electrical field and stress are the same (k_{33} coupling) and the other one section where the direction of the electrical field is perpendicular to the direction of stress (k_{31} coupling). These two sections are mechanically coupled by the cross section, as shown in Fig. 2.1a so that a voltage ratio proportional to l/h can be achieved. Usually, the section where the direction of the electrical field is perpendicular to the direction of stress is manufactured in a multi-layer structure. Therefore, the voltage conversion ratio is increased by n times, where n is the number of layers. However, the small side electrodes leads to the low power level of Rosen-type PT. In addition, the electromechanical coupling factor of the section where the direction of the electrical field is perpendicular to the direction of stress, which is k_{31}, is the lowest of the main coupling factors in most piezoelectric materials. This also the reason that Rosen-type PTs tend to be applicable for low power applications.

- Longitudinal mode with k_{33} coupling [44, 45] (see Fig. 2.1b)

  Longitudinal mode PT with both input and output sections utilizing k_{33} coupling (Fig. 2.1b) is attractive since k_{33} is usually the strongest electromechanical coupling factor of a piezoelectric material. However, this design still suffers from small electrode size which limits the power level.

- Longitudinal mode with k_{31} coupling [46] (see Fig. 2.1c)

  Longitudinal mode PT with both input and output sections utilizing k_{31} coupling provides large electrode size as shown in Fig. 2.1c, which is desirable for high power design. However, k_{31} coupling still limits the power.

- Thickness mode PT [7, 47–68] (see Fig. 2.1d and Fig. 2.1e)

  In both sections of the thickness mode PTs, the direction of the electrical field is in parallel with the direction of stress, both in thickness direction, as shown

in Fig. 2.1d. The thickness dimension of thickness mode PTs is much less than the other dimensions, therefore they are with k_t coupling which is smaller than k_{33} coupling. Thickness mode PTs can operate at high frequency (e.g., several megahertz), which is inversely proportional to the thickness, and high power level, which contributes by the relatively large electrodes. However, the main issue with thickness mode PTs is that, high order length and width or radius extensional resonances occur in the vicinity of the thickness resonances because the direction of wave propagation is not the largest dimension [69]. These spurious modes increase the loss of the PTs and attenuate the main vibration mode, which is not desired in practical applications. To avoid this, without changing the geometry and vibration mode, a piezoelectric material with relatively small coupling factors of other modes can be used. In addition, since the largest dimension of the PT will define the lowest resonant frequency, modifying the dimensions will also help to suppress spurious modes. For example, if each layer of the PT in Fig. 2.1d is modified to a ring-shaped one, as shown in Fig. 2.1e and the ratio of the inner radius to outer radius is set to be sufficiently small, then the frequency of the radial mode will tend to infinity so that spurious mode will not affect the main vibration mode. Nevertheless, the cost is the decreased power level due to reduced electrodes size.

- Radial mode PT [70–85] (see Fig. 2.1f to Fig. 2.1h)

  Radial mode PTs are polarized along the thickness direction and vibrate along the radial direction, as shown in Fig. 2.1f. And the coupling factor that corresponds to this geometry and vibration mode is k_p, which is one of the largest coupling factors. In addition, the geometry of the radial mode PT contributes to electrodes with large area. These factors help radial mode PTs achieve high power level. Also, since the radius is much larger than the thickness of each layer, the first radial resonance does not incur interference from other vibration modes. Therefore,a radial mode PT can provide clean frequency response. Besides the radial mode PT shown in Fig. 2.1f, which is disc-shaped, it can also be a ring-dot-shaped or ring-shape one, as shown in Fig. 2.1g and Fig. 2.1h respectively. However, the disc-shaped one is the most promising

design because it has an overall shape and electrode profile that is simple to manufacture, especially for multi-layer design [69]. Since a PT transfers energy electromechanically, it is important that the method by which the device is mounted to the PCB does not damp its motion. Disc-shaped radial mode PTs in have a nodal point (a point where the amplitude of the displacement is zero) at the centre of the disc. Thus, a simple adhesive pad can be placed in the center of one of the PTs major surfaces to securely mount the device without noticeably affecting its electromechanical behaviour.

- Contour mode PT [86, 87] (see Fig. 2.1i)

  Contour mode PT consists of a square piece of piezoelectric material with circular electrodes stacked in the thickness direction, as shown in Fig. 2.1i. They are polarized in the thickness direction and vibrate in contour-extensional direction. Compared to the disc-shaped radial mode PTs, the corners of the contour mode PTs only lead to extra mechanical losses without aiding power handling [69].

- Thickness-shear mode PT [88–94] (see Fig. 2.1j)

  The thickness-shear mode PT differs from the designs previously described, where the electric fields are applied and generated orthogonally to, rather than parallel to, the direction of poling in the input and output sections of the PT, as shown in Fig. 2.1j. Excitation of the input section causes a shear strain to develop throughout the PT body, which in turn generates a voltage in the output section. Most piezoelectric materials suitable for use in PTs have a large shear mode electromechanical coupling factor k_{15}, allowing high power densities to be achieved with this type of PT. However, like thickness mode devices, it can be difficult to obtain a clean frequency response from a thickness-shear mode device due to interference from high order length and width modes.

Among aforementioned PTs, the Rosen-type PT and the disc-shaped radial PT are the most widely used. Rosen-type PTs have been extensively used in applications that do not require high power but require high voltage conversion ratio. For

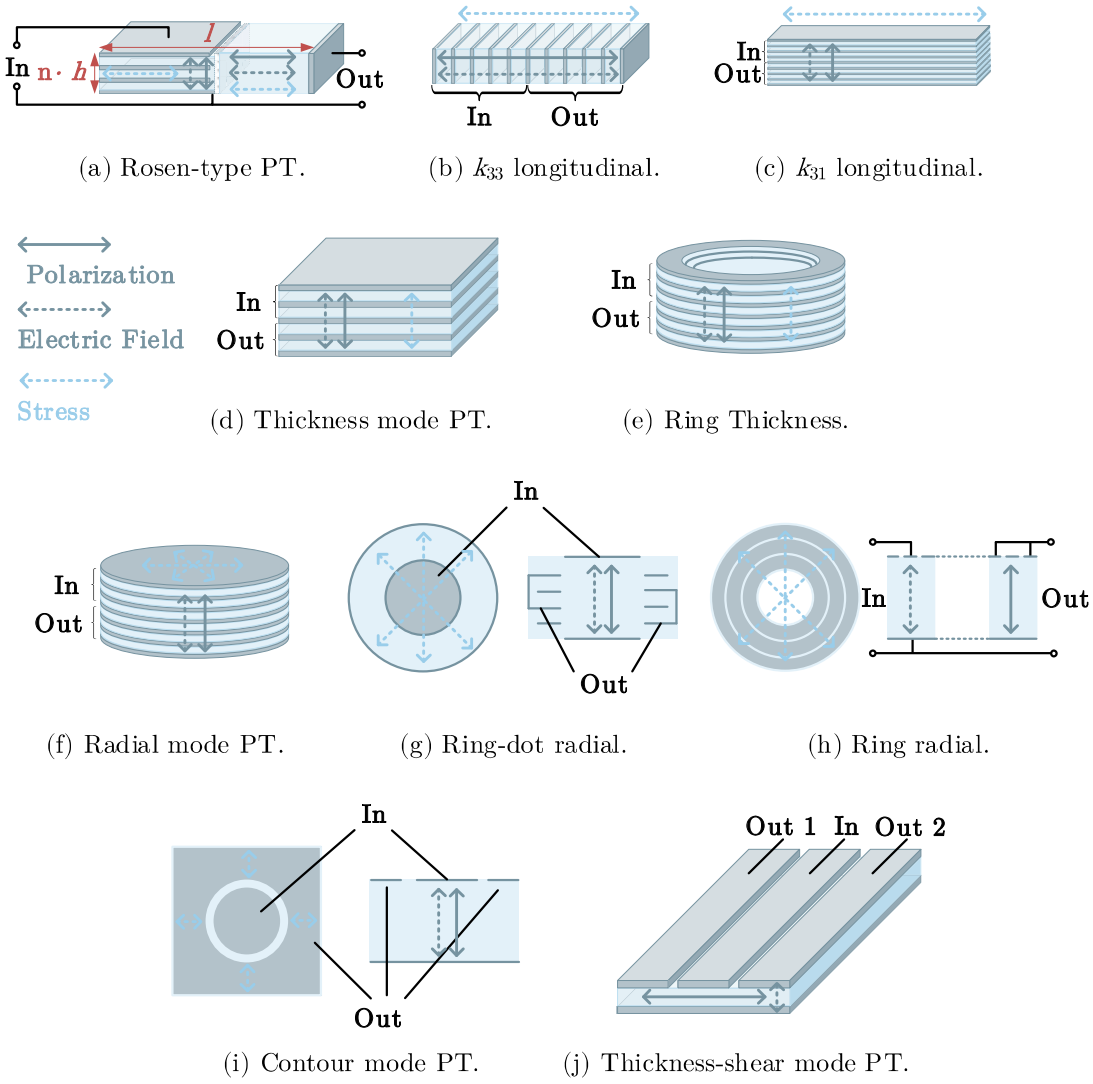

(a) Rosen-type PT. (b) k_{33} longitudinal. (c) k_{31} longitudinal.

(d) Thickness mode PT. (e) Ring Thickness.

(f) Radial mode PT. (g) Ring-dot radial. (h) Ring radial.

(i) Contour mode PT. (j) Thickness-shear mode PT.

Figure 2.1: Different types of PTs.

example, it has been used in applications, such as ballast for fluorescent lamp [17], driver for light-emitting diodes or cold-cathode fluorescent lamps [18,19], and plasma generator [95], providing high output voltage ranging from several kilovolts to tens of kilovolts, given a low input voltage ranging from several volts to tens of volts. Radial PTs are usually used in power applications because they have geometry that naturally results in a clean frequency response around the first radial resonance, relatively large coupling factor, layout that allows for large electrode radius and force factors, an overall shape and electrode profile that is simple to manufacture,

and a conveniently located nodal point, which are all beneficial for power transmission and mass production. Radial PTs have been employed in applications such as electronics lamp ballasts and ac-dc adapter [17, 45, 67, 70, 96–98]. It can provide advantages such as no electromagnetic interference source and no requirement for winding compared to its magnetic counterparts.

However, there is still much to be studied in this field. For example, for Rosen-type PTs, they are usually considered to be less suitable for use in step-down applications [7, 69, 70]. However, the high voltage conversion ratio and high voltage insulation naturally provided by the Rosen-type PT is a significant advantage in some specific applications, e.g., high step-down auxiliary power supplies in medium-/high-voltage systems such as solar power equipment and electric charging station. In addition, the driving and control for radial mode PTs-based power converters have been extensively discussed [7, 69, 70] and there is always more to explore. These are all research objectives of this work. To better utilized the advantages provided PTs, the analysis of the characteristics of PTs, which is presented in this chapter, is necessary.

2.2 Equivalent Circuit Models of PTs

As far as electrical applications are concerned, an equivalent circuit model is needed for the PT to be better understood and utilized. The interaction between the electrical energy and mechanical energy needs to be illustrated in a more circuit-oriented manner. No matter which type the PT is, the inter-conversion between the electrical energy and mechanical energy in the PT can be represented by Fig. 2.2.

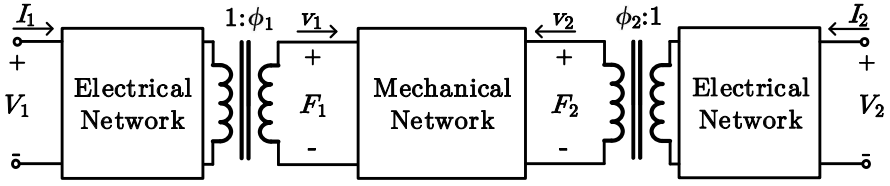

Figure 2.2: General block-diagram of the behavior model of PTs.

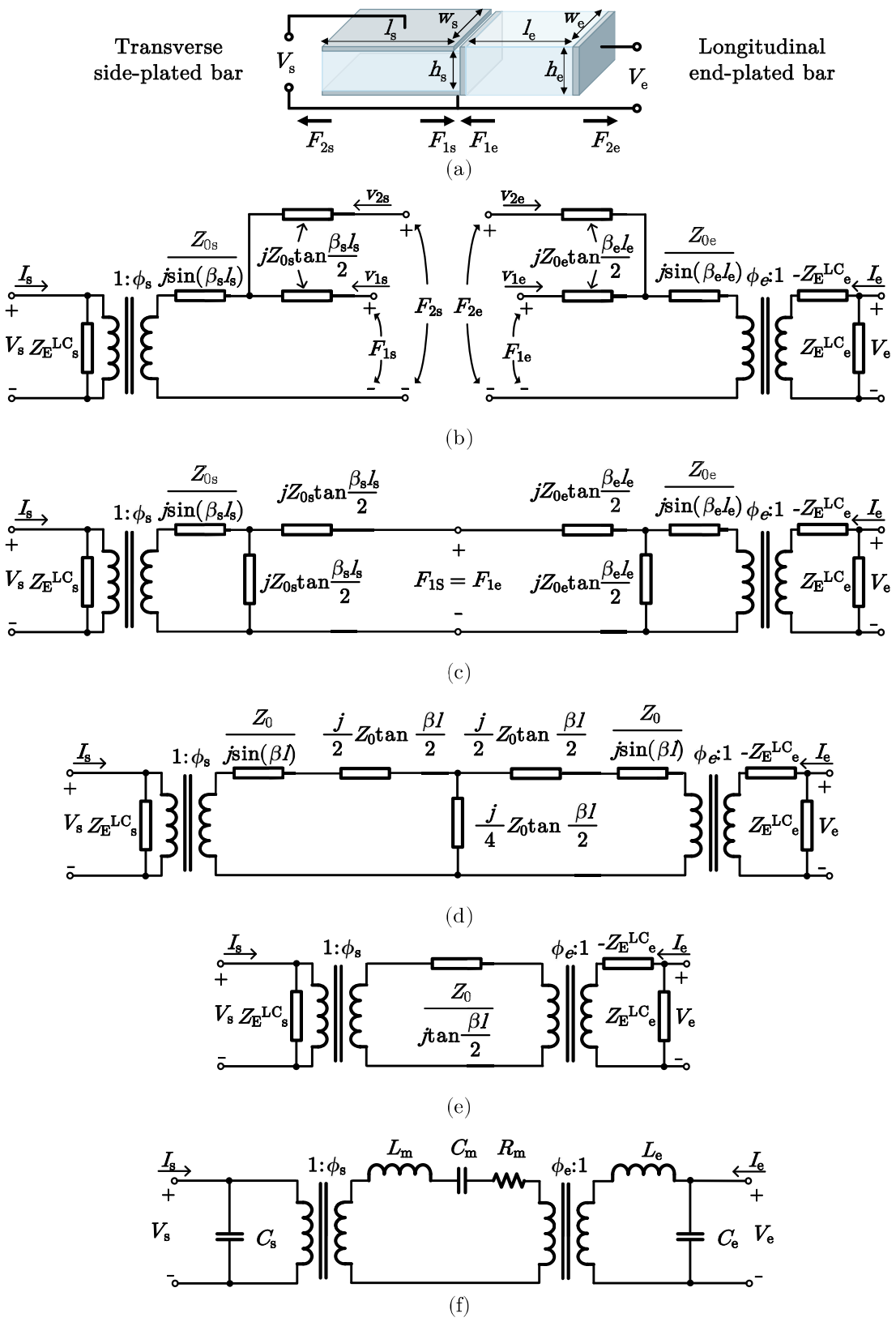

Figure 2.3: Derivation of the equivalent circuit model of a single-layer Rosen-type PT.

The general derivation of the equivalent behavior model of a single-layer Rosen-type PT is presented as follows as an example. Detailed and rigorous derivation has been completed by [4,7–9]. A single-layer Rosen-type PT, as presented in Fig. 2.3a is composed by one section with k_{31} coupling, which is also called as a side-plated bar, and the other one section with k_{33} coupling, which is also called as a end-plated bar. The models of electromechiancal couplings of the side-plated bar and the end-plated bar have been shown in Fig. 1.7 and are re-drawn in Fig. 2.3b, where force is analogous to the voltage and velocity is analogous to the current.

For Rosen-type PT shown in Fig. 2.3a, the two sides of the PT are free to move, therefore,

$$F_{2s} = F_{2e} = 0. \tag{2.1}$$

In addition, the transverse side-plated bar and the longitudinal end-plated bar are bonded together, therefore,

$$F_{1s} = F_{1e}. \tag{2.2}$$

Based on (2.1), the F_{2s} and F_{2e} terminals can be treated as short-circuit connection. And base on (2.2), the F_{1s} and F_{1e} terminals can be treated as parallel-circuit connection. Therefore, Fig. 2.3b can be redrawn as Fig. 2.3c.

By designing the parameters of the side-plated bar and the end-plated bar so that

$$\beta_s l_s = \beta_e l_e = \beta l = n\pi (n = 1, 2, 3, ...), \tag{2.3}$$

and

$$Z_{0s} = Z_{0e} = Z_0, \tag{2.4}$$

Fig. 2.3c can be redrawn as Fig. 2.3d by using Δ-Y (Π-Y) conversion.

Since $\beta l = n\pi (n = 1, 2, 3, ...)$ according to (2.3), the value of the middle parallel mechanical impedance is infinity, Fig. 2.3d can be further simplified to Fig. 2.3e. Keeping the fundamental components while neglecting high order components of the Taylor expansion of the series mechanical branch and with the electrical impedance calculated, Fig. 2.3e can be redrawn in an electrical form, which is Fig. 2.3f, where L_m, C_m, and R_m are analogies for mass, compliance, and mechanical damping re-

spectively.

The equivalent circuit model of the disc-shaped radial mode PT can be derived in a similar manor, which is depicted in Fig. 2.4. Detailed and rigorous derivation can be found in [69, 99].

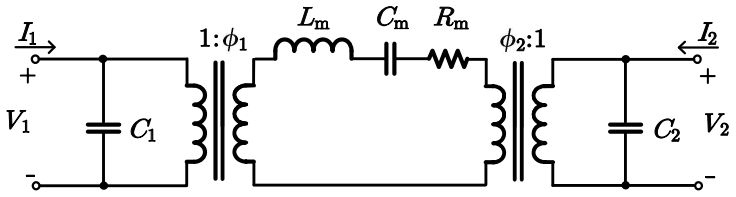

Figure 2.4: Equivalent circuit model of a radial mode PT.

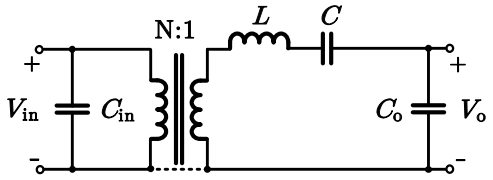

(a) w/o loss resistances

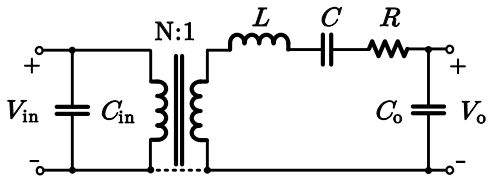

(b) w/ R, w/o R_d

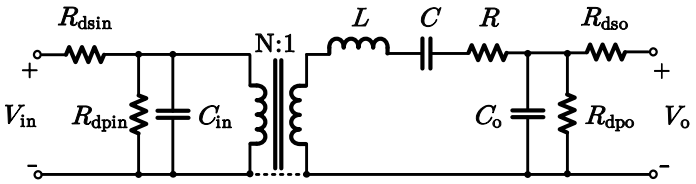

(c) w/ R and R_d

Figure 2.5: Equivalent circuit model of a radial mode PT.

No matter the PT is Rosen-type or radial mode, its equivalent circuit model (Fig. 2.3f or Fig. 2.4) can be re-drawn as Fig. 2.5. A PT can be constructed into a

common-ground type or a isolated type if insulation layer is used. The circuit model in Fig. 2.5a is an ideal behavior model without considering any loss while the circuit model in Fig. 2.5b includes the mechanical damping transformed into electrical magnitude by the piezoelectric effect, which is the most significant loss in PTs operated near the fundamental resonance. However, according to the experimental results shown in [42] and [100], the efficiency characteristic analysis based on the model in Fig. 2.5b is not accurate. Except the mechanical loss, dielectric loss in PTs also needs to be considered. Dielectric loss was first proposed to be represented by the parallel resistances R_{dpin} and R_{dpo}, shown in Fig. 2.5c. To be more accurate, [42] proposed to add the series resistances R_{dsin} and R_{dso}. This gives the complete accurate model near fundamental frequency, the circuit model in Fig. 2.5c. In piezoelectric material, the dielectric loss is strongly frequency dependent and can be modeled as

$$R_{\mathrm{dpx}} = \frac{1}{\omega C_{\mathrm{x}} \delta_{\mathrm{px}}}, \quad R_{\mathrm{dsx}} = \frac{\delta_{\mathrm{sx}}}{\omega C_{\mathrm{x}}}, \quad (\mathrm{x} = \mathrm{in}, \mathrm{o}), \tag{2.5}$$

where δ_{p} and δ_{s} are dielectric loss angle constants of the piezoelectric material, and ω is the operation angular frequency.

Besides the three models near the fundamental resonance stated above, [70] proposed a model over a wider frequency range, where odd harmonic branches are added, shown in Fig. 2.6. However, this model is not widely used in practice because PTs are preferred to be operated near the fundamental resonance in real applications to avoid large mechanical damping so that high efficiency can be maintained.

2.3 Electrical Characteristics of PTs

This section analyzes the gain, input impedance, and efficiency characteristics of the PT respectively. However, the four non-constant dielectric loss resistances in the accurate model in Fig. 2.5c increase the complexity when analyzing the electrical characteristics of the PT. Simplification is needed to provide an intuitive understanding of the electrical characteristics of the PT. Taking the Rosen-type PT used in this work (LNA3207A, Micromechatronics Inc.) for example, whose parameters

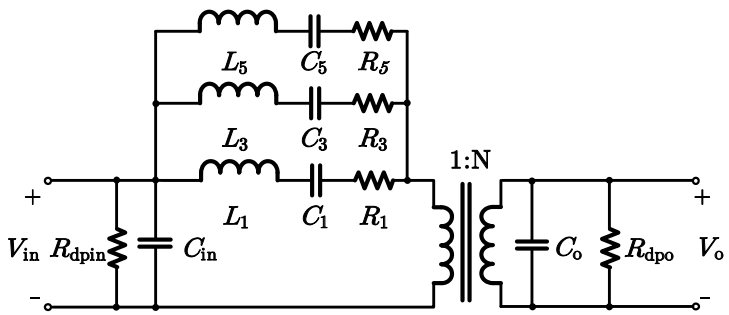

Figure 2.6: Model of PTs with harmonic components considered.

are listed in Table. 2.1 corresponding to Fig. 2.5, Fig. 2.7 compares the calculated normalized gain, input impedance, and efficiency surfaces versus the operation frequency f and the load resistance R_o under three conditions: the behavior model circuit without any loss resistance in Fig. 2.5a; circuit model with only mechanical loss resistance as shown in Fig. 2.5b; and complete circuit model including both mechanical loss resistance and dielectric loss resistance as shown in Fig. 2.5c. It can be found that all the three circuit models provide similar results except for efficiency surfaces. Therefore, the behavior model without any loss resistance in Fig. 2.5a can be used for the analysis of gain and input impedance characteristics. A circuit model with only mechanical loss resistance in Fig. 2.5b can be used for efficiency approximation when the PT is operated very near the maximum efficiency point. A complete circuit model in Fig. 2.5c is needed to locate the maximum efficiency point.

Table 2.1: Parameters of the sample PT used in this work.

L [mH]	C [nF]	R [Ω]	C_o [μF]	C_{in} [pF]	N	$\delta_{pin,o}$	$\delta_{sin,o}$
1.2	8.7	0.85	0.19	16	50	0.001	0.01

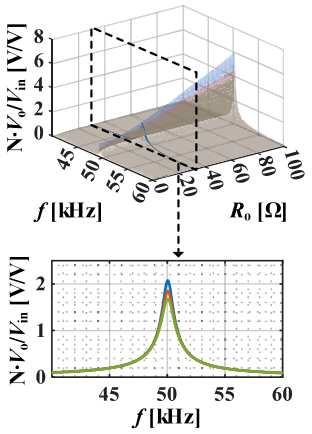

(a) Normalized voltage gain.

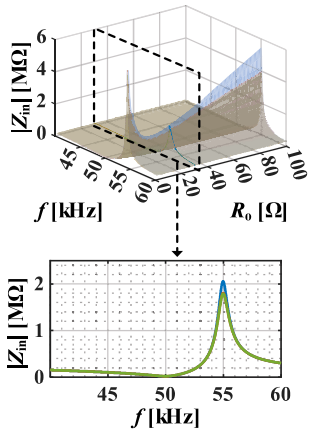

(b) Amplitude of input impedance.

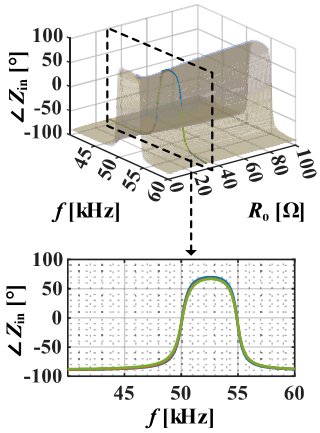

(c) Phase angle of input impedance.

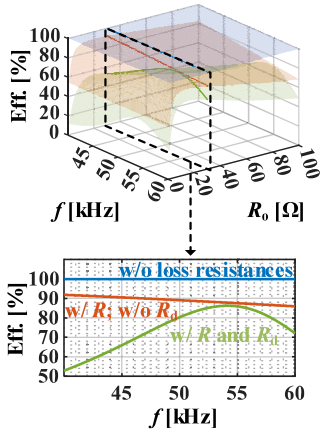

(d) Efficiency.

Figure 2.7: Voltage gain, input impedance and efficiency characteristics of sample Rosen-type PT in step-down configuration: blue - behavior model circuit without any loss resistance; red - circuit model with only mechanical loss resistance; green - complete circuit model with both mechanical and dielectric loss resistances.

2.3.1 Input-to-Output Voltage Gain

Loaded with resistor R_o, by neglecting both electrical and mechanical loss resistances, the normalized input-to-output voltage gain can be calculated as

$$\left|\frac{NV_o}{V_{in}}\right| = \left|\frac{\frac{R_o}{1+j\omega R_o C_o}}{j\omega L + \frac{1}{j\omega C} + \frac{R_o}{1+j\omega R_o C_o}}\right|. \tag{2.6}$$

In general, there are two types of characteristic gain points as a resonant tank: the unity gain point(s) and the maximum gain point. By setting (2.6) equal to 1, which can be rewritten as

$$(\omega^2 L - \frac{1}{C})[(C_o^2 + \frac{1}{\omega^2 R_o^2})(\omega^2 L - \frac{1}{C}) - 2C_o] = 0, \tag{2.7}$$

the two unity gain points can be solved as

$$\omega_{1L} = \frac{1}{\sqrt{LC}} = \omega_{sr}, \tag{2.8}$$

$$\omega_{1R} = \frac{1}{\sqrt{L\left(\frac{1}{\frac{1}{C}+\frac{2}{C_{os,1R}}}\right)}}, C_{os,1R} = C_o + \frac{1}{\omega_{1R}^2 C_o R_o^2}. \tag{2.9}$$

It can be found that the frequency of the left unity gain point ω_{1L} locates at the series resonant frequency ω_{sr}, which depends only on values of L and C. While the frequency of the right unity gain point ω_{1R} depends not only on PT's parameters but also on load resistance R_o.

In addition, the mechanical resonant frequency is defined as

$$\omega_{mr} = \frac{1}{\sqrt{L_m C_m}}. \tag{2.10}$$

It should be noticed that the definition of mechanical resonant frequency ω_{mr} is different from that of series resonant frequency ω_{sr}. For radial mode PTs, $\omega_{mr} = \omega_{sr}$. For Rosen-type PTs, they are two different points even their locations may be close to each other.

By setting the derivation of (2.6) with respect to frequency equal to zero, the frequency of the maximum gain point can be solved as

$$\omega_{mg} \approx \frac{1}{\sqrt{L\left(\frac{1}{\frac{1}{C}+\frac{1}{C_{os,mg}}}\right)}}, C_{os,mg} = C_o + \frac{1}{\omega_{mg}^2 C_o R_o^2}. \tag{2.11}$$

Table. 2.2 compares the calculation results of (2.8), (2.9), and (2.11) with the corresponding simulation results based on the complete circuit model with one

example R_o equal to 30 Ω, which verifies the correctness of the equations. Based on gain curves under different loads, which are displayed in Fig. 2.8, with increased load resistance, ω_{1L} maintains unchanged, while ω_{1R} and ω_{mg} increase. When R_o approaches infinity, $C_{os,mg}$ in (2.11) approaches C_o, consequently the maximum gain frequency approaches parallel resonant frequency, which is

$$\lim_{R_o \to \infty} \omega_{mg} = \omega_{pr} = \frac{1}{\sqrt{L\left(\frac{1}{\frac{1}{C}+\frac{1}{C_o}}\right)}}. \tag{2.12}$$

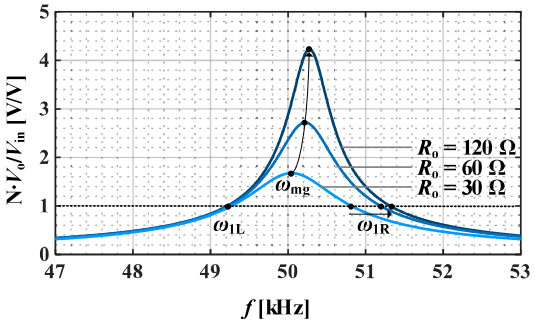

Figure 2.8: Gain curves of the sample PT under different load conditions.

Table 2.2: Simulation vs. calculation results of characteristic gain points of the sample PT with $R_o = 30\,\Omega$.

	f_{1L} [kHz]	f_{mg} [kHz]	f_{1R} [kHz]
Simulation	49.27	50.05	50.82
Calculation	49.19	50.04	50.89

2.3.2 Input Impedance

The calculation and analysis of the input impedance characteristic is also be based on the model without any loss resistance in Fig. 2.5a. Fig. 2.7b and Fig. 2.7c are the typical input impedance Z_{in} curve and the phase angle curve of Z_{in}. There are three special points: maximum Z_{in} phase point, minimum $|Z_{in}|$ point ("resonant point") and maximum $|Z_{in}|$ point ("anti-resonant point"). Inductive input impedance is necessary for zero-voltage turn-on. When neglecting both electrical and mechanical

loss resistances, in order to achieve inductive input impedance, the load resistance and the operation frequency need to meet

$$(\omega^2 LC - 1)(C_{\text{in}} + C - \omega^2 LCC_{\text{in}}) + \omega^2 R_{\text{o}}^2 (C_{\text{o}} + C - \omega^2 LCC_{\text{o}})$$

$$(\omega^2 LCC_{\text{in}}C_{\text{o}} - CC_{\text{in}} - C_{\text{o}}C_{\text{in}} - CC_{\text{o}}) > 0 \tag{2.13}$$

2.3.3 Efficiency

For the operation frequency near the frequency that renders the maximum PT's efficiency, the efficiency of the PT can be approximated by neglecting the dielectric loss while only considering the mechanical loss as

$$\eta = \frac{1}{1 + \frac{R}{R_{\text{os}}}}, R_{\text{os}} = \frac{R_{\text{o}}}{1 + (\omega C_{\text{o}} R_{\text{o}})^2}, \tag{2.14}$$

where R_{os} is the equivalent series resistance of the output impedance, which physically is the output capacitor C_{o} in parallel with output resistor R_{o}. Equation (2.13) indicates that the larger R_{os} leads to higher efficiency. For a given operating frequency, the maximum efficiency lies at the maximized R_{os} when

$$R_{\text{o}} = \frac{1}{\omega C_{\text{o}}}. \tag{2.15}$$

2.3.4 Experimental Measurement

Fig. 2.9a and Fig. 2.9b are the test boards and corresponding schematics for the sample Rosen PT in step-up and step-down configurations respectively. The size of the sample Rosen PT is 32 mm × 6.75 mm × 2.5 mm. Fig. 2.10 is the plot of input resistance R_{in} versus reactance X_{in}. If we mark out the aforementioned unity-gain, peak-gain, series and parallel resonant, maximum input impedance phase, resonant, anti-resonant, and the maximum efficiency points, it can be found that all the special points are different from each other, even they may be close to each other. Therefore, none of these special points can be simply referred as "resonant point" .

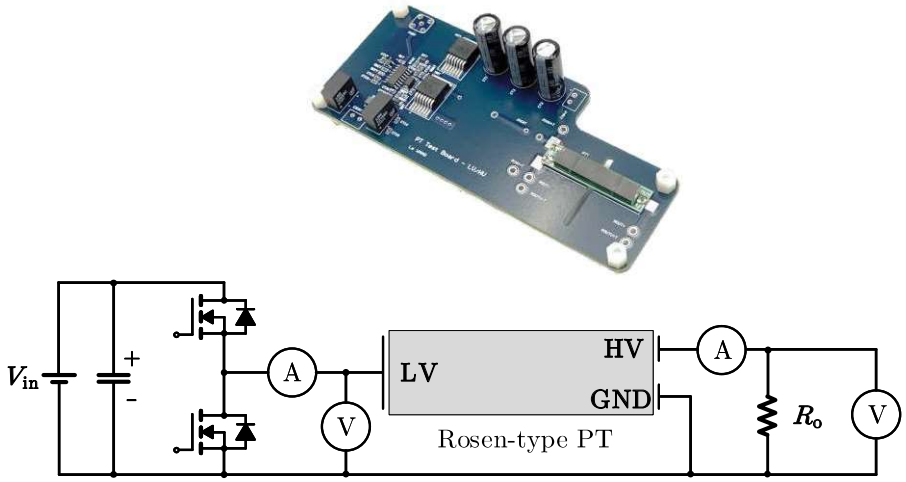

(a)

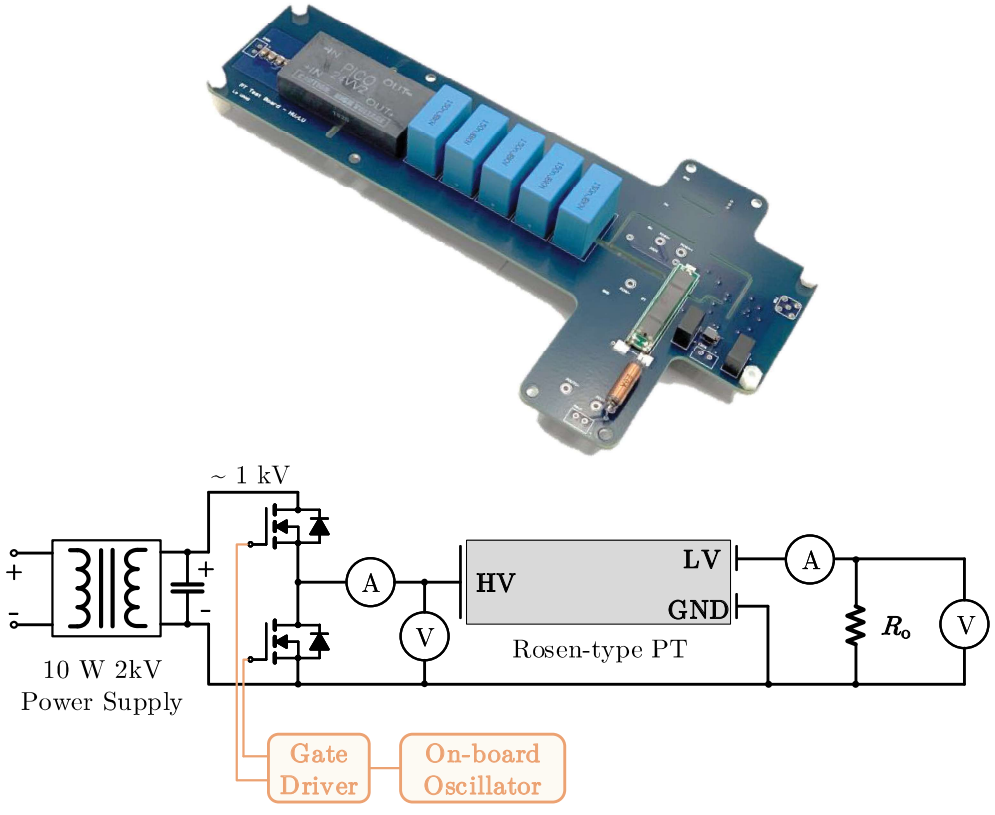

(b)

Figure 2.9: Test boards of PT in (a) step-up and (b) step-down configurations.

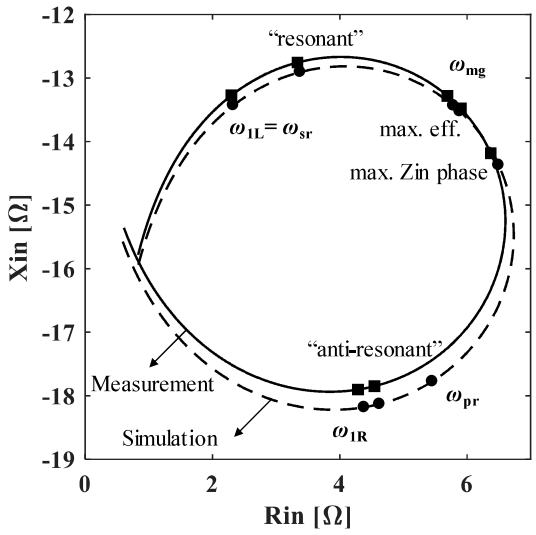

(a)

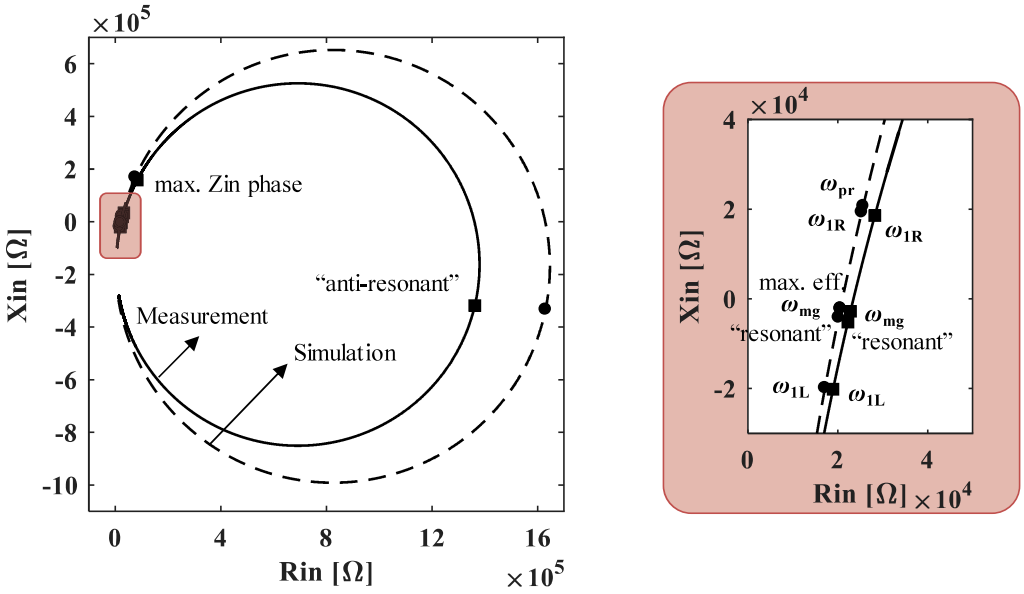

(b)

Figure 2.10: Impedance curves of PT in (a) step-up and (b) step-down configurations.

2.4 Impacts of Compensation Networks on Characteristics of PTs

To provide a better performance, i.e., higher efficiency, inductive input impedance, desired voltage gain, etc., compensation component(s) may be required. A series or parallel output inductor can be used to compensate the reactive power of the output capacitor of the PT so that the efficiency of the PT can be improved. A series or parallel input inductor can be used to achieve inductive input impedance if the input impedance of the PT itself is capacitive in desired operation range, which is necessary for zero-voltage turn-on for pre-stage's switches. Fig. 2.11 presents the aforementioned compensation components, which includes the series output inductor L_{os}, the parallel output inductor L_{op}, the extra output capacitor C_{oext}, the series input inductor L_{ins}, the parallel input inductor L_{inp}, and the extra input capacitor C_{inext}. Impacts of each compensation component are analyzed separately in the following parts. In addition, an application example that utilizes the combination of different compensation components is presented at the end of this section. The analysis uses the parameters of the aforementioned sample Rosen-type PT in step-down configuration as an example, but the derivation is generally applicable for all types of PTs.

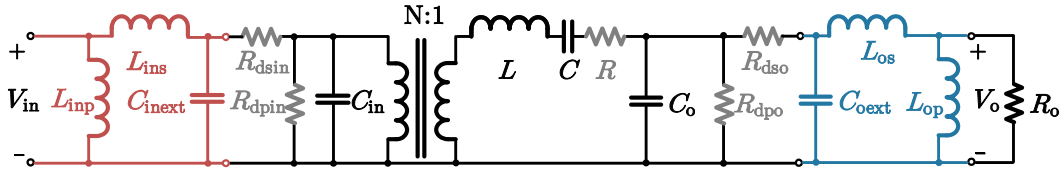

Figure 2.11: PT with possible compensation networks.

2.4.1 Impacts of the Series Output Compensation Inductor L_{os}

In this subsection, only the series output inductor L_{os} is considered, which means $L_{\mathrm{ins}} = C_{\mathrm{inext}} = C_{\mathrm{oext}} = 0$ and $L_{\mathrm{inp}} = L_{\mathrm{op}} = \infty$. From physical point of view, L_{os} with a value in resonance with the output capacitor C_{o} can compensate the reactive power of C_{o} so that the overall efficiency can be improved. To mathematically verify

this statement, the equivalent circuit with only mechanical loss, while all dielectric loss resistors are neglected for simplicity, is used to calculate the efficiency. With L_{os} added, the efficiency of the PT can still be calculated in the form same as (2.14), but with R_{os} in (2.14) changed to $R_{os,Los}$, which is

$$\eta = \frac{1}{1 + \frac{R}{R_{os,Los}}},$$

$$R_{os,Los} = \frac{R_o}{(1 - \omega^2 C_o L_{os})^2 + (\omega C_o R_o)^2}. \tag{2.16}$$

For each pair of ω and R_o, the best efficiency can be achieved at the maximized $R_{os,Los}$ when

$$L_{os} = \frac{1}{\omega^2 C_o}, \tag{2.17}$$

$$R_{os,Los,max} = \frac{1}{\omega^2 C_o^2 R_o}. \tag{2.18}$$

Fig. 2.12 compares the gain, input impedance, and efficiency surfaces with $L_{os} = 0$ and $L_{os} = 1/(\omega^2 C_o)$. In the case that the compensation inductor is in series with the load resistor, L_{os} has weak impact on the electrical characteristics when the impedance of the L_{os} is much smaller than the load resistance R_o. L_{os} mainly affects the electrical characteristics for heavy load cases, which reduces the voltage gain, reduce the amplitude and phase of the input impedance, and increases efficiency. It can be verified that, the efficiency is improved when R_o is small by comparing (2.18) and (2.14). When R_o is sufficiently large, the $R_{os,Los,max}$ in (2.18) will be close to R_{os} in (2.14). That means $L_{os} = 1/(\omega^2 C_o)$ will not help improving efficiency a lot any more, which can also been verified in Fig. 2.12.

2.4.2 Impacts of the Parallel Output Compensation Inductor L_{op}

Besides the series output inductor L_{os}, a parallel output inductor L_{op} can also compensate the reactive power of the output capacitor C_o so that the efficiency can be improved. In this subsection, only the parallel output inductor L_{op} is considered, which means $L_{ins} = L_{os} = C_{inext} = C_{oext} = 0$ and $L_{inp} = \infty$. For this case, similar to subsection 2.4.1, with L_{op} added, the efficiency of the PT can still be calculated

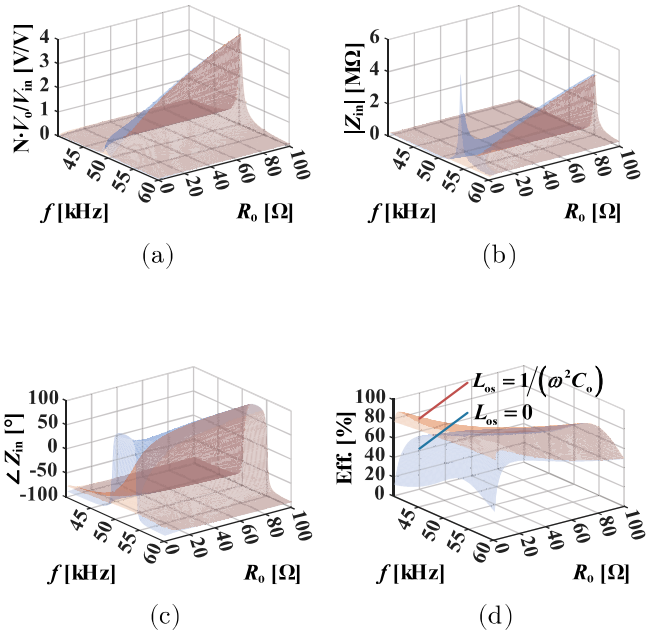

Figure 2.12: Normalized gain, input impedance and efficiency surfaces under different series output inductor L_{os}.

by (2.14), but with R_{os} changed to $R_{os,Lop}$, which is

$$\eta = \frac{1}{1 + \frac{R}{R_{os,Lop}}},$$

$$R_{os,Lop} = \frac{1}{\frac{1}{R_o} + \frac{R_o(1-\omega^2 C_o L_{op})^2}{\omega^2 L_{op}^2}}. \tag{2.19}$$

For each pair of ω and R_o, the best efficiency can be achieved when

$$L_{op} = \frac{1}{\omega^2 C_o}, \tag{2.20}$$

$$R_{os,Lop,max} = R_o. \tag{2.21}$$

Fig. 2.13 compares the gain, input impedance, and efficiency surfaces with $L_{op} = \infty$ and $L_{op} = 1/(\omega^2 C_o)$. In the case that the compensation inductor is in parallel with the load resistor, L_{op} has weak impact on the electrical characteristics when the impedance of the L_{op} is much larger than the load resistance R_o. L_{op} mainly affects the electrical characteristics for light load cases, which reduces the

voltage gain, reduce the amplitude and phase of the input impedance, and increases efficiency.

Both L_{os} and L_{op} can improve the efficiency. By comparing Fig. 2.12 and Fig. 2.13, two differences between L_{os} and L_{op} can be found. One is that the best efficiency is achieved at smaller R_o when L_{os} is applied compared to the L_{op} case. With L_{op} applied, wider high efficiency operation range can be achieved compared to the L_{os} compensation case. By calculating with (2.18) and (2.21), L_{op} compensation can provide higher efficiency for $R_o > 1/(\omega C_o)$, while L_{os} compensation can provide higher efficiency for $0 < R_o < 1/(\omega C_o)$.

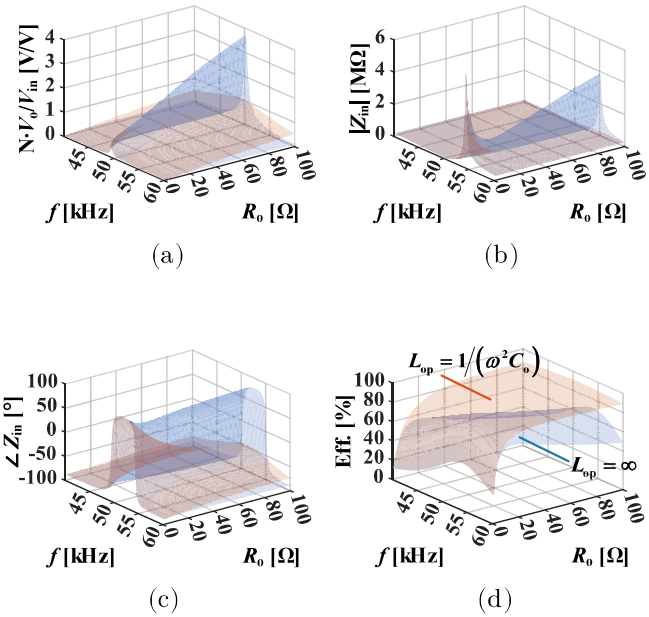

Figure 2.13: Normalized gain, input impedance and efficiency surfaces under different parallel output inductor L_{op}.

The other difference is that the parallel compensation significantly modifies the gain surface compared to the series compensation case for the sample PT used in this work. The reason is that, for parameters of the sample PT, the impedance magnitude of the output capacitor, which equals to that of the resonant compensation inductor, ranges from 20 Ω to 13 Ω for the operation frequency ranging from 40 kHz to 60 kHz. For load resistance much larger than this value, magnitude of the output impedance is dominated by the the load resistor and the output capacitor.

Therefore, series compensation inductor L_{os} has little impact on the voltage gain, especially when load resistance is larger than 20 Ω. However, the parallel compensation inductor L_{op} cancels the output capacitor of the PT C_{o}. This leads to an output impedance only determined by the load resistance, which causes the significant change in the voltage gain characteristic of the PT. Especially, when resonant L_{op} is applied, when operating at series resonant frequency, with L_{op} also in resonance with C_{o}, the PT can provide constant voltage gain when R_{o} is much lager than the loss resistance, as indicated in Fig. 2.14.

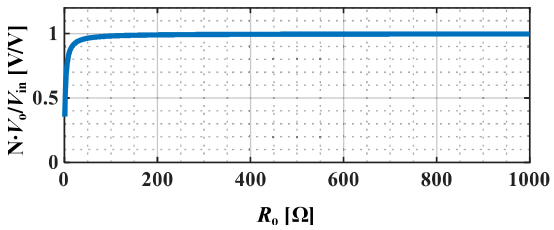

Figure 2.14: Normalized gain curve for $\omega^2 = L_{\mathrm{op}}C_{\mathrm{o}} = LC$.

2.4.3 Impacts of the Extra Output Capacitor C_{oext}

For some types of PTs, the internal output capacitor C_{o} might be very small, which leads to a large compensation inductor. Under these circumstances, an extra output capacitor C_{oext} can help to reduce the size of the compensation inductor.

When the series compensation L_{os} and the extra output capacitor C_{oext} are applied, C_{o} in (2.16), (2.17), and (2.18) needs to be replaced by $C_{\mathrm{o}} + C_{\mathrm{oext}}$, which leads to smaller $R_{\mathrm{os,Los,max}}$. This means that an extra output capacitor leads to a lower efficiency.

When the parallel compensation L_{op} and the extra output capacitor C_{oext} are applied, C_{o} in (2.19) and (2.20) needs to be replaced by $C_{\mathrm{o}} + C_{\mathrm{oext}}$. But $R_{\mathrm{os,Lop,max}}$ is independent on the output capacitance as shown in (2.21). This means that an extra output capacitor C_{oext} will not change the efficiency.

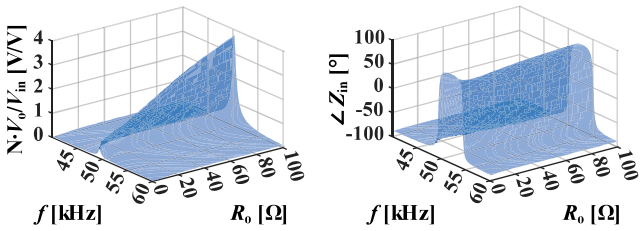

(a) $L_{\text{ins}} = \frac{0}{\omega^2 C_{\text{in}}}$.

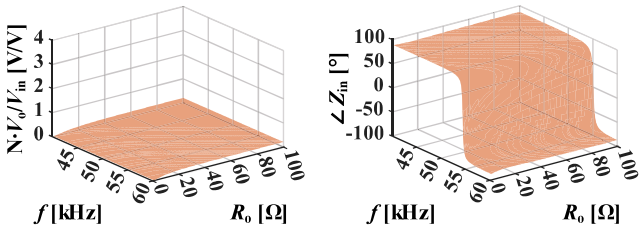

(b) $L_{\text{ins}} = \frac{1}{\omega^2 C_{\text{in}}}$.

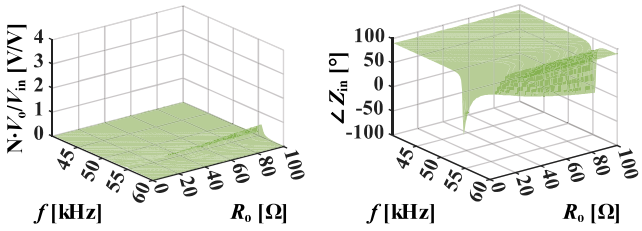

(c) $L_{\text{ins}} = \frac{10}{\omega^2 C_{\text{in}}}$.

Figure 2.15: Normalized gain and input impedance phase surfaces under different series input inductor L_{ins}.

2.4.4 Impacts of Input Inductors L_{ins} and L_{inp} and the Extra Capacitor C_{inext}

In this subsection, only input compensation components are considered, which means $L_{\text{os}} = C_{\text{oext}} = 0$ and $L_{\text{op}} = \infty$. Theoretically, ideal input compensation components do not change the efficiency characteristic since they do not have impacts on the calculation of R_{os}. Both L_{ins} and L_{inp} modify the input impedance characteristic, shown in Fig. 2.15 and Fig. 2.16. L_{inp} does not affect the gain characteristic while L_{ins} does.

Similar to the extra output capacitor C_{oext}, an external input capacitor C_{inext} can be used to reduce the size of the resonant input inductor. When the resonant L_{inp} is applied, C_{inext} does not change the voltage gain. While when the resonant L_{ins} is applied, the voltage gain increases with increased C_{inext} as shown in Fig. 2.17.

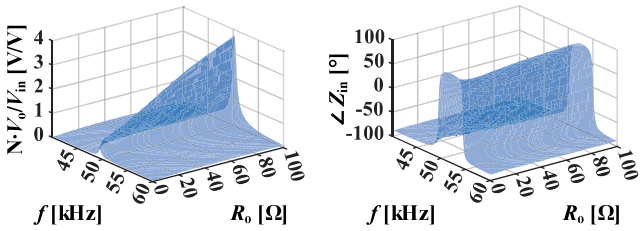

(a) $L_{\text{inp}} = \frac{\infty}{\omega^2 C_{\text{in}}}$.

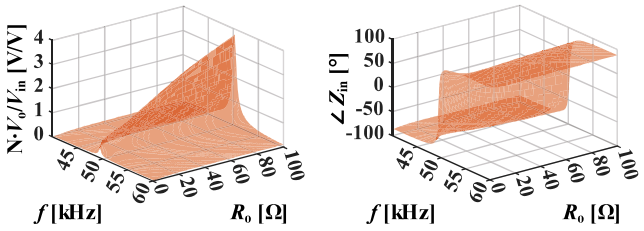

(b) $L_{\text{inp}} = \frac{1}{\omega^2 C_{\text{in}}}$.

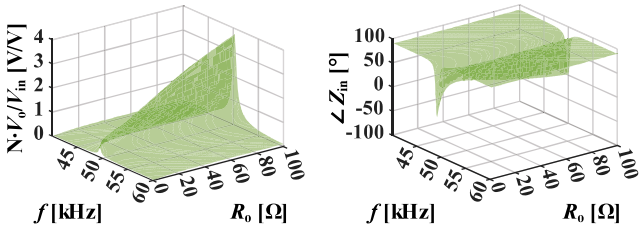

(c) $L_{\text{inp}} = \frac{0.1}{\omega^2 C_{\text{in}}}$.

Figure 2.16: Normalized gain and input impedance phase surfaces under different parallel input inductor L_{inp}.

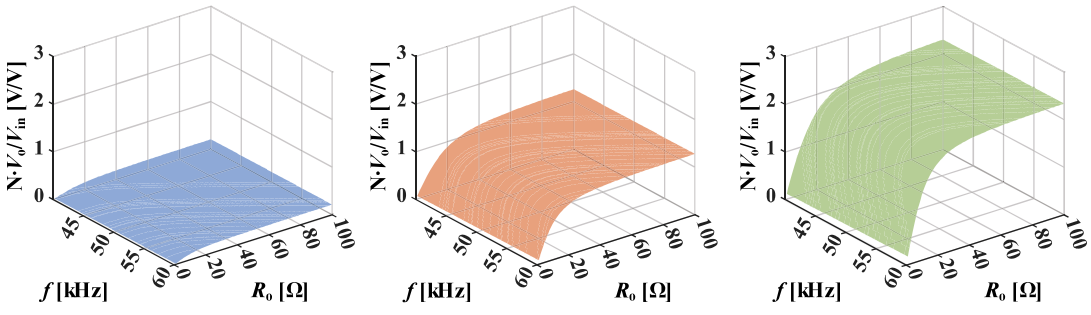

(a) (b) (c)

Figure 2.17: Normalized gain surfaces under different C_{inext}: (a) $L_{\text{inp}} = \infty, C_{\text{inext}} = 0, L_{\text{ins}} = \frac{1}{\omega^2(C_{\text{inext}}+C_{\text{in}})}$, (b) $L_{\text{inp}} = \infty, C_{\text{inext}} = 5C_{\text{in}}, L_{\text{ins}} = \frac{1}{\omega^2(C_{\text{inext}}+C_{\text{in}})}$, and (c) $L_{\text{inp}} = \infty, C_{\text{inext}} = 10C_{\text{in}}, L_{\text{ins}} = \frac{1}{\omega^2(C_{\text{inext}}+C_{\text{in}})}$.

2.4.5 Application Example: LCCL Compensation

As stated in subsection 2.4.2, when resonant L_{op} is applied and the PT is operated at series resonant frequency, with L_{op} also in resonance with C_{o}, that is, when $\omega^2 = L_{\text{op}}C_{\text{o}} = LC$, the PT can provide constant voltage gain when R_{o} is much lager than the loss resistance. This is not the only way to achieve constant voltage gain.

An LC tank, as depicted in Fig. 2.18a, provides constant-voltage-in-constant-current-out characteristic if the operation frequency equals to the LC resonant frequency [101] since

$$I_{\text{o}} = \frac{V_{\text{in}}}{Z(1-\omega^2 LC) + j\omega L} = \frac{V_{\text{in}}}{j\omega L}, \text{ if } \omega^2 LC = 1. \tag{2.22}$$

Similarly, a CL tank shown in Fig. 2.18 provides constant-current-in-constant-voltage-out characteristic if operated at the resonant frequency since

$$V_{\text{o}} = \frac{ZI_{\text{in}}}{(1-\omega^2 LC) + j\omega CZ} = \frac{I_{\text{in}}}{j\omega C}, \text{ if } \omega^2 LC = 1. \tag{2.23}$$

If an LC tank is cascaded by a CL tank, then a load-independent voltage gain can be achieved.

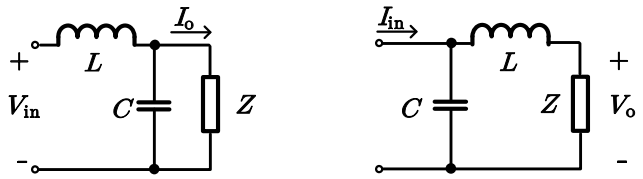

(a) (b)

Figure 2.18: (a) LC tank and (b) CL tank.

That is to say, for the application of the PT, as shown in Fig. 2.11, if only series resonant compensation inductors and extra compensation capacitors, i.e., L_{ins}, L_{os}, C_{inext}, and C_{oext}, are used, then a input LC tank is in series with the output CL tank. Therefore, if the parameters of the compensation network are selected as

$$L_{\text{ins}}(C_{\text{inext}} + C_{\text{in}}) = L_{\text{os}}(C_{\text{oext}} + C_{\text{o}}) = \omega^2, \tag{2.24}$$

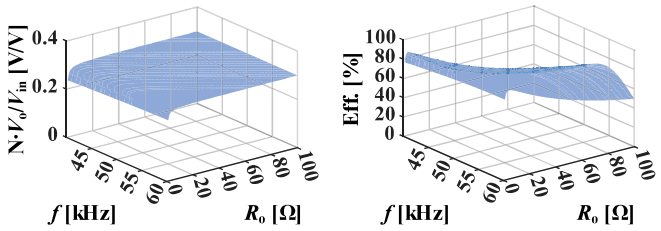

(a) $\frac{N^2 L_{\text{os}}}{L_{\text{ins}}} = 0.3, C_{\text{oext}} = 0.$

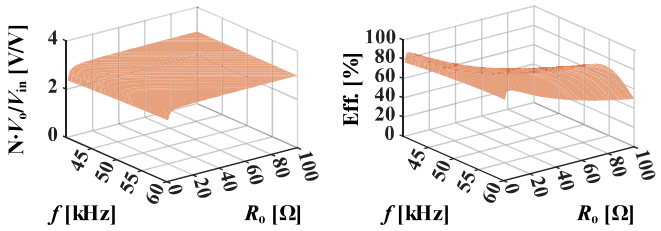

(b) $\frac{N^2 L_{\text{os}}}{L_{\text{ins}}} = 3, C_{\text{oext}} = 0.$

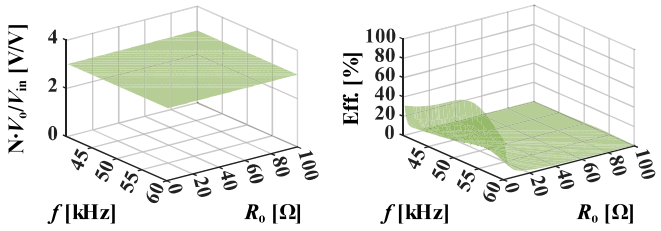

(c) $\frac{N^2 L_{\text{os}}}{L_{\text{ins}}} = 3, C_{\text{oext}} = 10C_{\text{o}}.$

Figure 2.19: Normalized gain and input impedance phase surfaces under different parallel input inductor L_{inp}.

then a constant-voltage-gain of

$$\frac{NV_{\text{o}}}{V_{\text{in}}} = \frac{N^2 L_{\text{os}}}{L_{\text{ins}}} \tag{2.25}$$

can be achieved theoretically.

Fig. 2.19 shows the gain and efficiency surfaces with different compensation network parameters. By comparing Fig. 2.19a and Fig. 2.19b, it can be verified that the normalized voltage gain equals to $\frac{N^2 L_{\text{os}}}{L_{\text{ins}}}$. The gain surface is not flat as calculated by (2.25). It drops when R_o approaches zero, which is caused by the dielectric loss.

By comparing Fig. 2.19b and Fig. 2.19c, it can be found that, with larger C_{oext} (as well as C_{inext}), the gain surface becomes flatter, but the efficiency drops. The reason for the efficiency drop has been explained in subsection 2.4.3.

Fig. 2.20 and Fig. 2.21 show the effects of nonidealities on the characteristics of LC and CL tanks under resonance, where R represents the loss resistor. For parallel loss resistance in the LC tank,

$$I_{\mathrm{o}} = \frac{V_{\mathrm{in}}}{j\omega L(1+\frac{Z}{R})}, \text{ when } \omega^2 LC = 1. \tag{2.26}$$

For series loss resistance in the LC tank,

$$I_{\mathrm{o}} = \frac{V_{\mathrm{in}}}{j\omega L + R(1+j\omega CZ)}, \text{ when } \omega^2 LC = 1. \tag{2.27}$$

For parallel loss resistance in the CL tank,

$$V_{\mathrm{o}} = \frac{I_{\mathrm{in}}}{j\omega C + \frac{Z+j\omega L}{ZR}}, \text{ when } \omega^2 LC = 1. \tag{2.28}$$

For series loss resistance in the CL tank,

$$V_{\mathrm{o}} = \frac{I_{\mathrm{in}}}{j\omega C(1+\frac{R}{Z})}, \text{ when } \omega^2 LC = 1. \tag{2.29}$$

Based on the equations (2.26) and (2.27), it can be found that, for LC tank, both parallel and series loss resistors affect the output-current-to-input-voltage gain. But only the series loss resistance in the LC tank, shown in Fig. 2.20b, makes the nonideality of the gain also affected by the value of C. Similarly, based on the equations (2.28) and (2.29), for CL tank, both parallel and series loss resistors affect the output-current-to-input-voltage gain. But only the parallel loss resistance in the CL tank, shown in Fig. 2.21b, makes the nonideality of the gain also affected by the value of C.

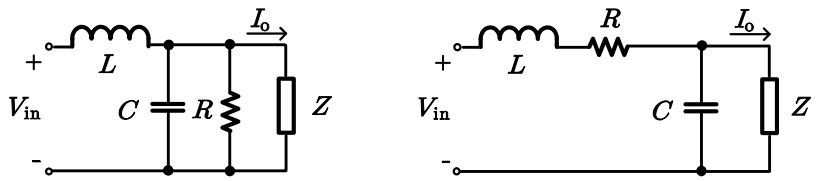

(a) Parallel R in LC tank. (b) Series R in LC tank.

Figure 2.20: Effects of nonidealities on the characteristics of LC tank under resonance.

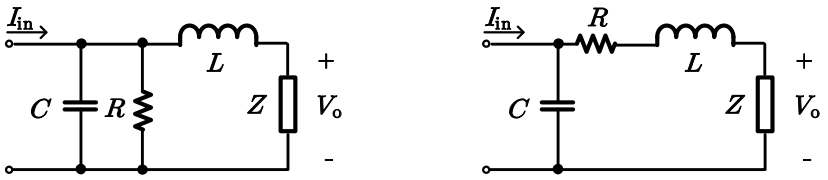

(a) Parallel R in CL tank. (b) Series R in CL tank.

Figure 2.21: Effects of nonidealities on the characteristics of CL tank under resonance.

Based on the above the analysis, the gain should become even more non-flat with larger C_{oext} (as well as C_{inext}). But in this subsection, external output and input capacitors C_{oext} and C_{inext} are assumed to be lossless to simplify the analysis. Larger ideal C_{oext} and C_{inext} weak the effect from the dielectric loss resistors, thus make the LCCL structure more ideal. In real applications, whether the gain surface will become flatter depends on whether the nonideality of external C_{oext} (as well as C_{inext}) is smaller than that of internal C_{o} (as well as C_{in}).

2.5 Summary and Conclusion

This chapter reviewed and compared different models of PT. The behavior model without any loss resistance can be used for the analysis of gain and input impedance characteristics. A circuit model with only mechanical loss resistance can be used for efficiency approximation when the PT is operated very near the maximum efficiency point. A complete circuit model with both mechanical and dielectric losses modeled is needed to locate the maximum efficiency point.

The electrical characteristics of, by not limited to, the sample Rosen-type PT are analyzed. Closed-form expressions of characteristic points are given, which include mechanical resonant, series resonant, parallel resonant, unity-gain, peak-gain, maximum input impedance, minimum input impedance, maximum input impedance phase, and maximum efficiency points. They have different expressions even their locations may be close to each other and may merge together in some special cases.

Impacts of the compensation components are also derived to improve the per-

formance of a standalone PT. The impacts of aforementioned compensation components are summarized as follows:

- Output compensation inductor L_{os} or L_{op} is utilized mainly to improve the efficiency of the PT. L_{os} provides higher efficiency for $0 < R_{\mathrm{o}} < 1/(\omega C_{\mathrm{o}})$ while L_{op} provides higher efficiency for $R_{\mathrm{o}} > 1/(\omega C_{\mathrm{o}})$. Especially, with L_{op} compensation, if $\omega^2 = L_{\mathrm{op}}C_{\mathrm{o}} = LC$, approximately constant voltage gain can be achieved.

- The utilization of C_{oext} helps reducing the size of required L_{os} or L_{op} at the trade-off of higher current of L_{os} or L_{op}. In addition, for L_{os} compensation case, C_{oext} leads to lower PT's efficiency.

- Input compensation inductor L_{ins} or L_{inp} is utilized mainly to modify the input impedance of the PT so that inductive input impedance can be achieved in desired operation range.

- C_{inext} helps reducing the size of required L_{ins} or L_{inp} at the trade-off of higher current of L_{ins} or L_{inp}.

In addition, when both input and output series resonant inductors are used, an approximate constant voltage gain characteristic can be achieved. The non-idealities have also been analyzed.

Based on studies of this work, the selection of compensation network can be decided according to the design specifications, such as output voltage requirement, load resistance range, etc., in real applications.

Chapter 3

Tunable Radial PT-Based Power Converter

3.1 Introduction

As stated in section 2.1, for power applications, radial mode PTs are considered as the most promising PTs to be alternatives for traditional magenetic transformers in some power converters. Because as a PT, it can provide advantages such as no electromagnetic interference source and no requirement for winding compared to its magnetic counterparts. Among many different types of PTs, radial mode PTs have geometry that naturally results in a clean frequency response around the first radial resonance, relatively large coupling factor, layout that allows for large electrode radius and force factors, an overall shape and electrode profile that is simple to manufacture, and a conveniently located nodal point. They have been employed in applications such as electronics lamp ballasts and ac-dc adapter [17,45,67,70,96–98].

For the control of PT-based converters, since the equivalent circuit of the PT can be treated as resonant tank, frequency control, where the operation frequency is adjusted so that the gain of the resonant tank is adjusted based on different input and/or load conditions to achieve regulation, as shown in Fig. 3.1a, is the most widely used in many applications. Besides aforementioned [17, 45, 67, 70, 96–98], [102–105] are also PT-based converters which employ frequency control. However, due to the frequency-dependent dielectric loss in PTs, they would suffer from low

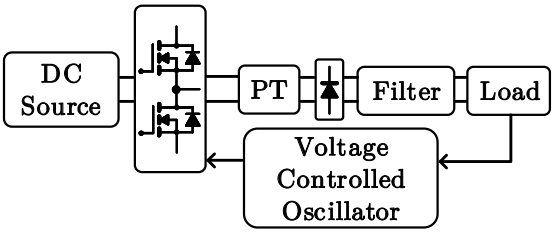

(a) PT-based converter with frequency control.

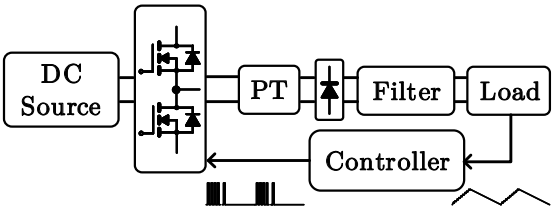

(b) PT-based converter with "quantum mode" control.

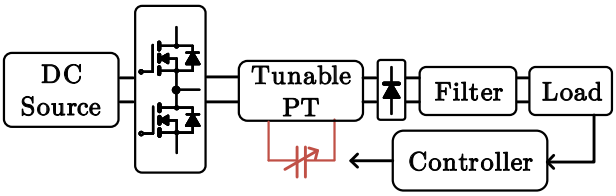

(c) Control scheme of tunable PT-based converter.

Figure 3.1: Different control schemes of PT-based converter.

efficiency when operated far away from the frequency rending peak efficiency, which has been presented in section 2.3. That happens when large load variations and/or wide input range present. For example, the experimental results in [102–105] shown narrow efficient control ranges. Therefore, for PT-based converters, narrow operation frequency range becomes a conflict against wide variations from load and/or input. To solve this issue, [106, 107] proposed a quantum mode control scheme, as presented in Fig. 3.1b. Under this control scheme, the PT will be operated under fixed frequency first to charge the load. Once the output voltage reaches the upper bound, then the power stage will stop working until the output voltage drops to the lower bound of the design. However, by doing so, the drawback is the presence of the low frequency ripple in the output voltage which requires a large filter capacitor.

To solve the issue, a radial mode PT with new structure, namely tunable PT has been proposed. Different from the conventional PT, which only has input and output ports, the tunable PT has an auxiliary control port, and the mechanical characteristic can be modified by connecting different impedance to this control port [108, 109]. Therefore, desirable voltage gain can be achieved by connecting proper impedance to the control port without changing switching frequency as shown in Fig. 3.1c. This chapter introduces the working principle and the electric characteristics of a tunable radial PT and presents the design and control of tunable PT-based converters, as continuation and extension of the work in [108,109].

3.2 Working Principle and Electrical Characteristics of Tunable Radial PT

3.2.1 Structure and Equivalent Circuit

Fig. 3.2a shows the structure of a typical radial mode PT. The piezoelectric material and copper electrodes in the input and output section are of the same radius. Whilst in reality the isolation layer is made slightly larger than the ceramic and electrode layers in order to improve the breakdown voltage, the amount of material in the section that extends past the radius of the ceramic and electrode layers is very

small and can be neglected. Hence, all layers in the PT can be assumed to be of equal radius. Since the layers of the device are stacked and bonded together in the thickness direction, whereas the motion being considered is radial, the PT can be modelled as a single piece of composite material whose structural properties are defined by its constituents. Therefore radial strain is assumed constant with thickness and a single equation of radial motion can be used for the whole device. And the corresponding only force is the one acting on the outer circumference of the PT, which is represented by F_{a} in Fig. 3.2b. The input and output voltages are linked with F_{a} by the electrical and mechanical impedances shown in Fig. 3.2b. Detailed expressions and derivations of these impedances have been presented in [69, 99]. Applying standard network theorems, the circuit of Fig. 3.2b can be simplified to that shown in Fig. 3.2c, where C_{d1} and C_{d2} are input and output dielectric capacitance, ϕ_1 and ϕ_2 represent the electro-mechanical couplings, and L_{m}, C_{m}, and R_{m} are analogies for mass, compliance, and mechanical damping respectively.

Tunable PT has a similar structure as Fig. 3.2a, but with an additional piezoelectric section (control layer) sandwiched between the input and the output section, which is depicted in Fig. 3.3a. The layers of the tunable PT are still stacked and bonded together in the thickness direction, whereas the motion being considered is radial, which is same as the ordinary radial mode PT. Therefore, the tunable PT still can be modelled as a single piece same as the ordinary radial mode PT but with one more electrical port, as shown in Fig. 3.3b. Fig. 3.3b can be further simplified to the circuit of Fig. 3.3c. From the circuit' point of view, as shown in Fig. 3.3c, the control port is analogy for the second output winding in a magnetic transformer with multi-winding configuration.

3.2.2 Electrical Characteristics

The circuit in Fig. 3.3c can be redrawn as Fig. 3.4a. With the control port referred to the input side, Fig. 3.4a can be further redrawn as Fig. 3.4b. From circuit's point of view, external impedance connected at the control port modifies the resonant tank between input and output, which provides opportunity to achieve different voltage

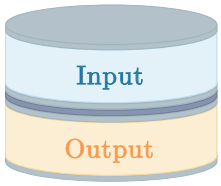

(a) Structure layout.

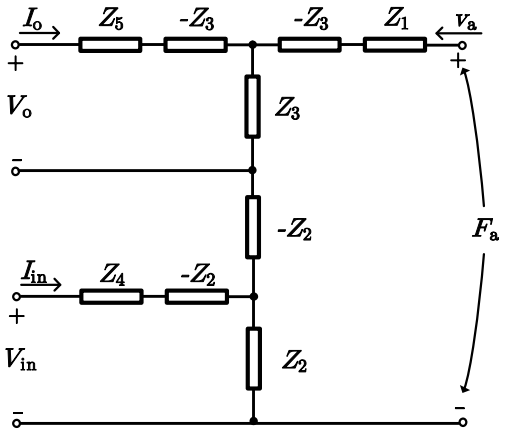

(b) Equivalent circuit representation of electro-mechanical coupling.

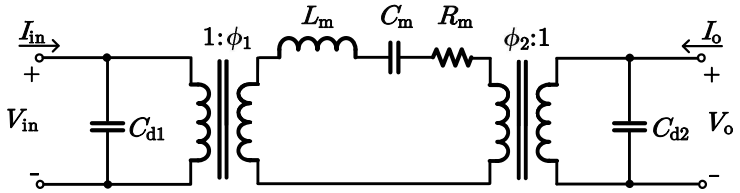

(c) Simplified equivalent circuit model.

Figure 3.2: Structure and equivalent circuit model of the radial mode PT.

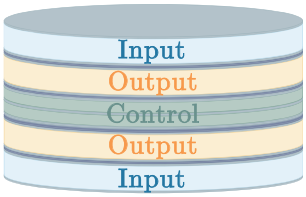

(a) Structure layout.

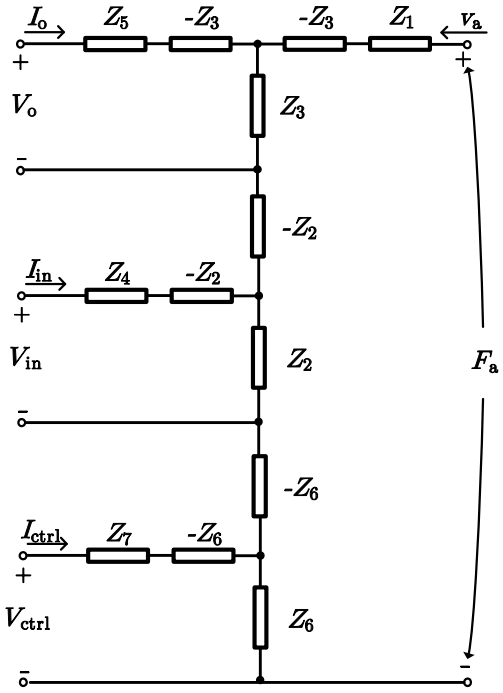

(b) Equivalent circuit representation of electro-mechanical coupling.

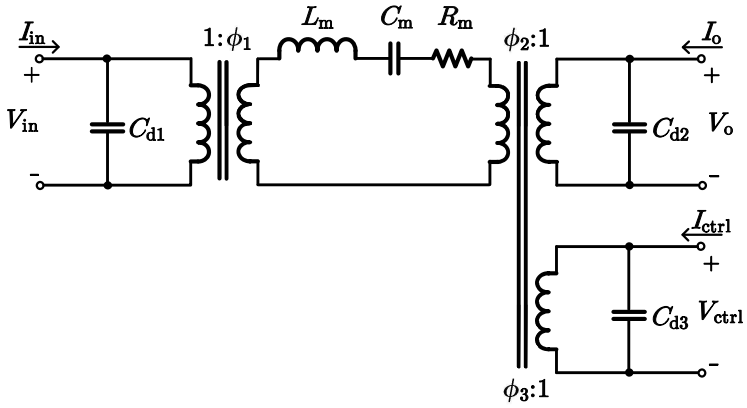

(c) Simplified equivalent circuit model.

Figure 3.3: Structure and equivalent circuit model of the tunable radial mode PT.

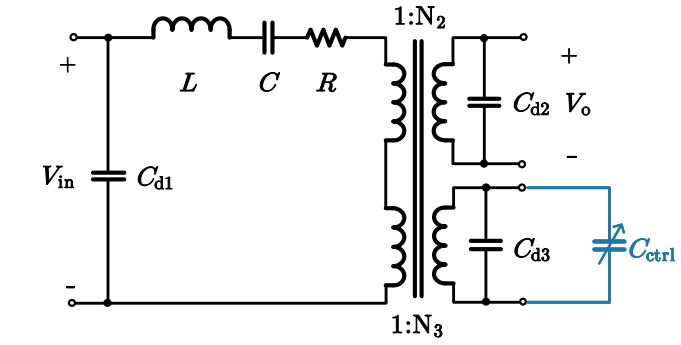

(a)

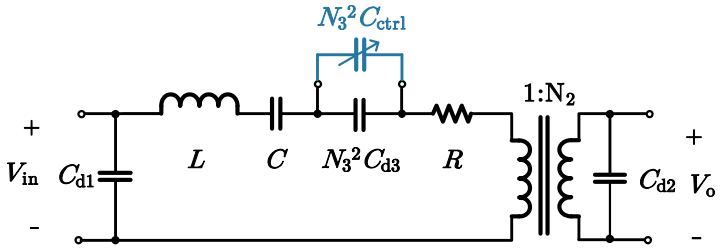

(b)

Figure 3.4: Equivalent circuits of the tunable radial mode PT.

gain for different input and/or load conditions while maintain constant operation frequency. A capacitor is selected as the tuning impedance at the control port since if the control port is connected with other passive elements, such as resistor or inductor, it will cause extra loss or lead to a higher order system. The existence of the capacitance connected at the control port C_{ctrl} modifies the resonance capacitance of the series LC tank from a fixed one for ordinary two-port PT to a variable one, which is

$$C_{\text{s}} = \frac{CN_3^2(C_{\text{d3}} + C_{\text{ctrl}})}{C + N_3^2(C_{\text{d3}} + C_{\text{ctrl}})}, \tag{3.1}$$

if C_{ctrl} is variable.

The only difference between the three-port tunable PT and the ordinary two-port PT is that tunable PT has a third port designed to be connected in series with the output port so that the resonance capacitance of the series LC tank is variable if a variable capacitor is connected to the control port. Therefore, for a specific control capacitance, the electrical characteristics of the tunable PT, which include the input-to-output voltage gain, the input impedance and the efficiency, are similar

to those of an ordinary two-port PT, which have been stated in section 2.3. For a specific control capacitance, the curves(surfaces) of the input-to-output voltage gain, the input impedance and the efficiency of a radial PT resemble the curves(surfaces) in Fig. 2.7.

The impacts of the control port connected with an extra capacitor on the input-to-output voltage gain can be reflected by

$$\left|\frac{V_\mathrm{o}}{N_2 V_\mathrm{in}}\right| = \left|\frac{\frac{R_\mathrm{o}}{(1+j\omega R_\mathrm{o} C_\mathrm{d2})N_2^2}}{R + j\omega L + \frac{1}{j\omega C_\mathrm{s}} + \frac{R_\mathrm{o}}{(1+j\omega R_\mathrm{o} C_\mathrm{d2})N_2^2}}\right|, \tag{3.2}$$

where C_s is expressed in (3.1), if a resistive load R_o is connected at the output port.

Taking one of the tunable PTs used in this work as an example, based on the parameters listed in Table. 3.1, the normalized input-to-output voltage gain curve is plotted in Fig. 3.5. For example, for $R_\mathrm{o} = 10\,\Omega$, if the operation frequency is 59 kHz, then the corresponding normalized voltage gain is 1.1. Now if R_o is increased to $50\,\Omega$, the gain curve shifts, and the gain increases to around 4 at the same operation frequency. But now if the control capacitance C_ctrl is increased from 0 to 70 nF, the gain curve shifts back and the gain is pulled back to 1.1, which means constant gain at constant operation frequency for different load and/or input conditions can be achieved with the help of a variable control capacitor.

Table 3.1: Parameters of the sample tunable PT used in this work.

L [mH]	C [nF]	R [Ω]	C_{d1} [nF]	C_{d2} [nF]	C_{d3} [nF]	N_2	N_3
5.9	1.5	4.3	23.2	352.8	20.2	0.2	0.9

In addition, it should be noticed that the effect of increased C_ctrl will saturate due to the series connection of C and the capacitors at the control port. The maximum value of C_s is limited by the value of C. This can also been verified by Fig. 3.6, the curve of the normalized voltage gain versus C_ctrl at fixed operation frequency and load resistance. It can be found that, with increased C_ctrl, the voltage gain decreases. However, the voltage gain is almost unchanged when C_ctrl further increases.

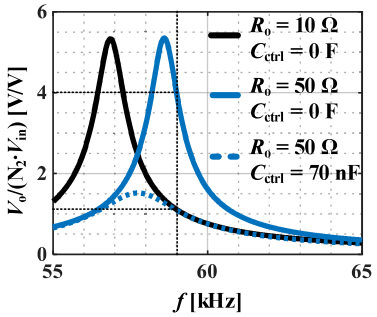

Figure 3.5: Voltage gain of the sample tunable PT with different load resistance and control capacitance.

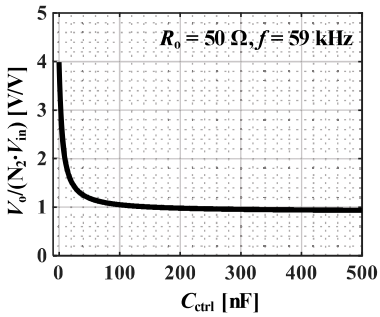

Figure 3.6: Voltage gain versus C_{ctrl} at fixed operation frequency and load resistance.

3.3 Design and Control of Tunable Radial PT-Based Power Converter

Taking advantage of the characteristic of the tunable PT stated above, a dc-dc converter is proposed as shown in Fig. 3.7. An inverter is used after the dc input to generate an AC voltage with desirable frequency. A rectifier is used at the output port of the PT to provide dc output voltage. Following the rectifier, a filter is needed to reduce the ripple of output voltage. A variable capacitor is used to realize voltage regulation for different load and/or input conditions at the constant operation frequency so that the high efficiency of PT is ensured. The detailed design procedure is given as follows.

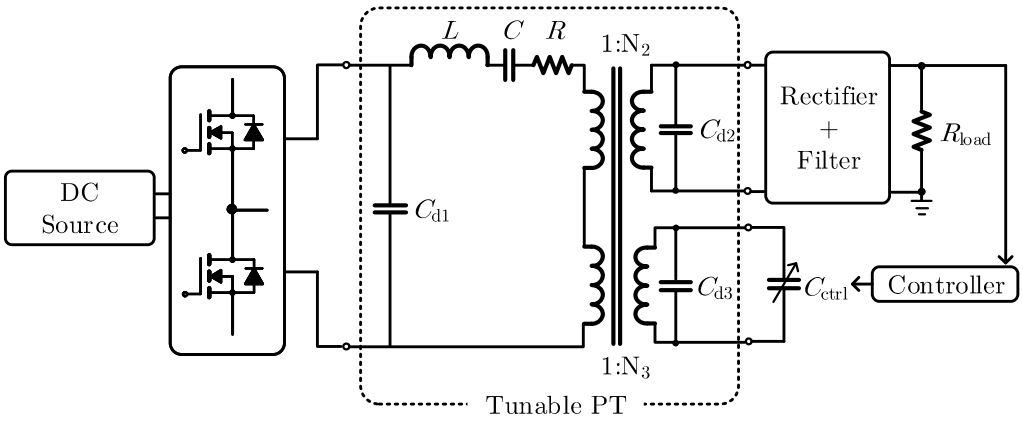

Figure 3.7: Overall block-diagram of the proposed tunable PT-based dc-dc converter.

3.3.1 Input Side Design

The input side is built with a half bridge and a series inductor. The half bridge is driven at constant frequency with complementary gate signals for the top and bottom switches. It provides AC input voltage for the PT with a simple and low-cost structure. The series input inductor blocks the high order input harmonics and can achieve inductive loading for the half bridge so that zero voltage switching (ZVS) of the switches of the half bridge can be realized.

3.3.2 Output Side Design

For the output side, a rectifier and a filter are needed. A synchronous rectifier can be used here instead of a diode rectifier to improve the system efficiency. For the filter design, there are several options, which are presented in Fig. 3.8. The first one, shown in Fig. 3.8a, is to use a full bridge rectifier with a capacitor as the filter, which can be seen in a few works, for example, [105]. However, this design suffers from the low efficiency because only when the voltage across the output capacitor of the PT C_{d2} is higher than the load voltage V_{load}, the energy can be transferred from the source to the load. In other words, C_{d2} requires current sink load to avoid freewheeling current.

To meet this requirement, one method is to add an output inductor after the full bridge rectifier, which forms a second-order low-pass LC filter along with the output capacitor, as shown in Fig. 3.8b. The average current of such inductor is non-zero, which is a dc current, therefore this output inductor is marked as dc output inductor.

The other method is to add the output inductor before the full bridge rectifier, as shown in Fig. 3.8c. For this case, the average current of the inductor zero, which is an AC current, so this inductor is denoted as AC output inductor.

Both circuits in Fig. 3.8b and Fig. 3.8c can provide better efficiency than the one in Fig. 3.8a. The design of both cases and the comparison of the difference between these two are presented as follows.

3.3.2.a Dc Output Inductor

With dc output inductor, the block diagram of the converter can be drawn as Fig. 3.9a. If only fundamental frequency component is considered and the inductance of L_{o} is infinity, the input voltage of the rectifier V_{rect} can be considered as a sinusoidal wave and the input current of the rectifier I_{rect} can be considered as a square wave and they are in phase [110]. This means the equivalent load resistance

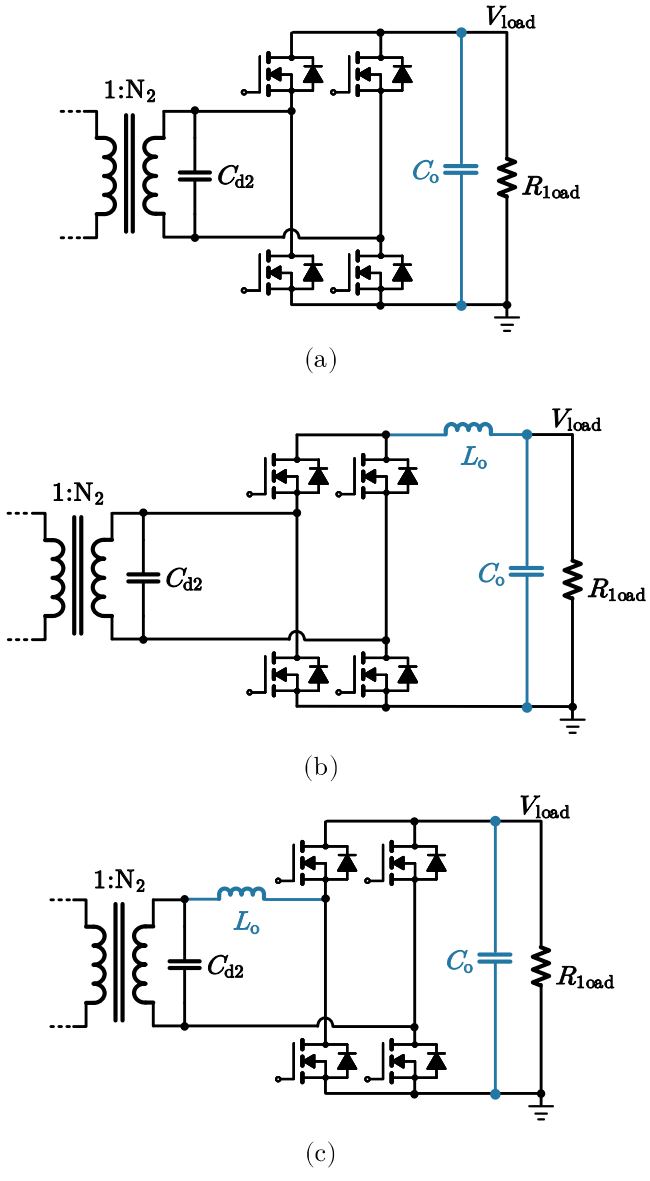

Figure 3.8: Output side design with (a) Capacitvie filter, (b) DC output inductor, and (c) AC output inductor.

seen by the tunable PT, R_o can be calculated as

$$R_{\mathrm{o}} \approx \frac{\pi^2}{8} \cdot R_{\mathrm{load}}. \tag{3.3}$$

Then the power stage of tunable PT based converter with dc output inductor can be simplified as Fig. 3.9b.

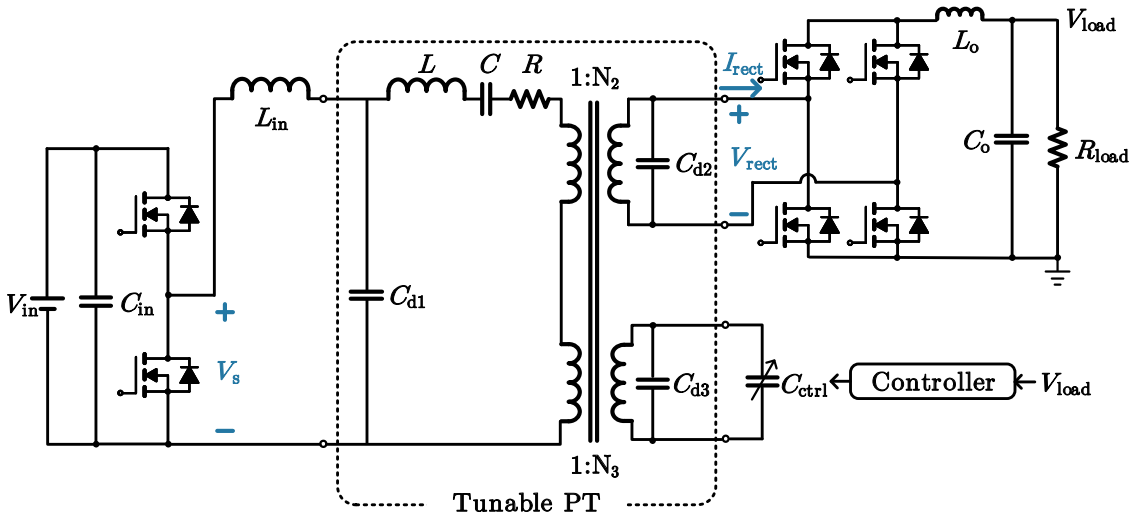

Figure 3.9: Tunable PT-based dc-dc converter with dc output inductor.

The criteria of selecting the input inductance is to achieve inductive load impedance for the half bridge with minimal inductance. For the sample tunbale PT with prameters listed in Table. 3.1, the inductance of L_{in} is selected to be 150 µH.

Then, based the normalized open-loop input-to-output (V_{s}-to-V_{o}) gain of the power stage versus C_{ctrl} curves under different load conditions with fixed selected

operation frequency can be drawn, as shown in Fig. 3.10. The solid line is the open-loop gain for full load condition while the dotted line is the gain curve for no load condition. In the final closed-loop system, under nominal input line voltage, the value of C_{ctrl} for full load will be zero to achieve maximum input and/or load range. It can be read out that, the gain at full load is 1.4 when C_{ctrl} is zero. Therefore, under nominal input line voltage, the gain should be regulated at 1.4 when load changes. It can be also read out that, to regulate the output voltage, that is to say, to keep the gain as 1.4, a 37 nF C_{ctrl} is needed for no load condition. In other words, ideally, the sample tunable PT-based dc-dc converter can regulate the output from full load to no load based on the calculation results shown in Fig. 3.10.

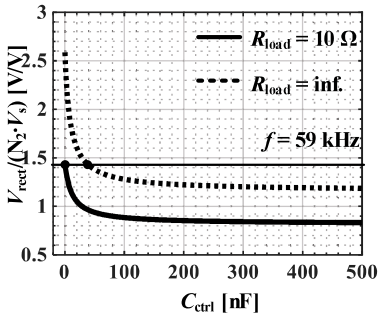

Figure 3.10: Normalized open-loop input-to-output voltage gain of power stage of design with dc output inductor.

However, in reality, the inductance of L_{o} cannot be infinity. Smaller L_{o} means more distortion of the current of I_{rect} from ideal square wave. In addition, larger the distortion is, less accurate the approximation in (3.3) will be. In fact, limited L_o decreases the regulation ability. Table. 3.2 shows the measured lightest load of the converter under different values of dc L_{o}.

Table 3.2: Lightest Load vs.Dc Output Inductance.

Dc output inductor [μF]	330	220	100	39
Lightest load	2.8%	3%	6%	10%

The value of L_{o} in the final design is selected based on the trade-off between the size of L_{o} and the regulation ability of the converter. For the sample tunable

PT listed in this section, L_o is selected as 220 µH.

3.3.2.b AC Output Inductor

With AC output inductor, the block diagram of the converter can be drawn as Fig. 3.11a. Similar as the one with dc output inductor, if only fundamental frequency component is considered and the inductance of L_o is infinity, the input voltage of the rectifier V_{rect} can be considered as a square wave and the input current of the rectifier I_{rect} can be considered as a sinusoidal wave and they are in phase [110]. Then the equivalent load resistance seen by the tunable PT, R_o can be calculated as

$$R_o \approx \frac{8}{\pi^2} \cdot R_{load}. \tag{3.4}$$

Then the power stage of tunable PT based converter with AC output inductor can be simplified as Fig. 3.11b.

By comparing Fig. 3.9b and Fig. 3.11b, it can be found that with AC output inductor, the simplified power stage has an extra output inductor compared to the one with dc output inductor. This output brings two benefits. One benefit is that the AC L_o compensates the reactive power of C_{d2}, therefore the efficiency of the PT can be improved, which has been mathematically analyzed in section 2.4.1. The other one is that, with AC output inductor, a CL tank is formed at the output, which is connected in series with the input LC tank. Based on the analysis in section 2.4.5, load-independent voltage gain characteristic can be achieved if the following equation is met:

$$L_{in}C_{d1} = L_oC_{d2} = \frac{1}{\omega^2} \tag{3.5}$$

For the sample tunable PT with parameters listed in Table. 3.1, L_{in} is 330 µH and L_o is 22 µH.

It should be noted that, the value of series resonant capacitor C_s is dependent on the variable C_{ctrl}, which means the resonant frequency of L and C_s are not fixed at the operation frequency. However, as long as the LC tank and the CL tank are in series, it will not affect the load-independent voltage gain characteristic.

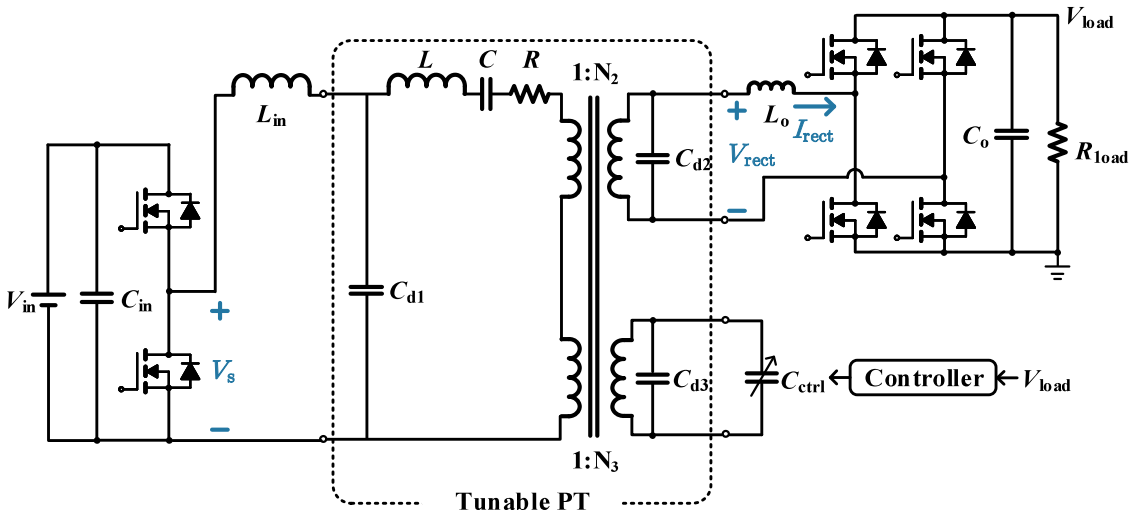

(a)

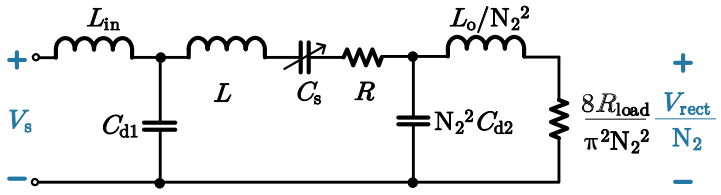

(b)

Figure 3.11: Tunable PT-based dc-dc converter with ac output inductor.

In addition, even though ideally the AC L_o case has the load-independent voltage gain characteristic, a closed-loop control is still needed to achieve exact regulated output in real applications due to the nonidealities caused by the damping of the system. However, this characteristic contributes to smaller control capacitor at the control port. It also helps the system to have wider load regulation range.

3.3.2.c Comparison of Dc vs. Ac Output Inductors

Fig. 3.12 compares the simulation results of power stages with dc and ac output inductors, based on parameters derived above, which are also listed in Table. 3.3. It can be verified by Fig. 3.12a, with AC output inductor, PT stage has higher efficiency since the output inductor L_o compensates the reactive power of the C_{d2}. In addition, AC output inductor provides constant gain along with the input LC tank and output capacitor, which means smaller range of the control capacitance will be required. As it can be seen from Fig. 3.12b, for the load resistor ranges from 10 Ω to 100 Ω, for the dc L_o case, the normalized open-loop gain of the power stage ranges from 1.44 to 2.55 while that of the AC L_o case ranges from 1.52 to 1.53, which means larger range of the control capacitance will be required for the dc L_o case. The comparison in Table. 3.3 shows that the design with AC output inductor requires larger L_{in} than the one with dc output inductor but smaller L_o.

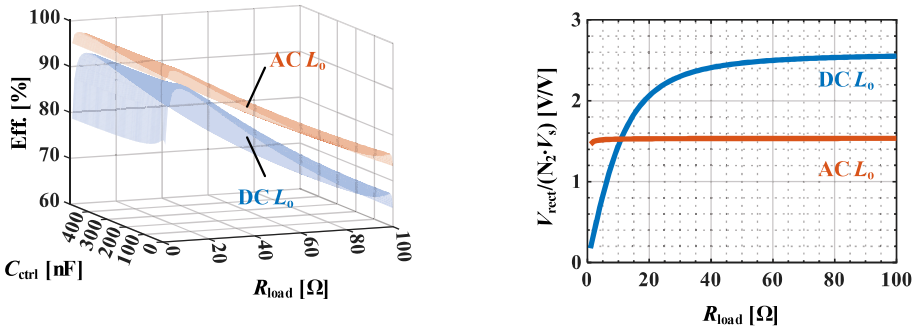

Figure 3.12: Comparison of designs with dc and ac output inductors.

Table 3.3: Comparison of designs with dc and ac output inductors.

	L_{in} [μH]	L_{o} [μH]
Design with dc output inductor	150	220
Design with ac output inductor	330	22

3.3.3 Control Side Design

To take advantage of the tunability of the tunable PT, a variable external capacitor is needed such that for each load or input condition it may afford a proper capacitance to regulate the output voltage. This idea can be realized by a switched capacitor [111], shown in Fig. 3.13a. Fig. 3.13b illustrates the operation principle of the switched capacitor. The turn on time of the switch S_{ctrl} is synchronized to t_1, the zero crossing time of the current I_{Cext}. C_{ext} is then charged until S_{ctrl} is turned off at t_1. After t_1, C_{ext} is float but C_{d3} continues to follow the input voltage. Once the voltage across C_{d3} drops below the voltage across C_{ext} at t_3, the body diode of S_{ctrl} conducts and C_{ext} starts to discharge. Once I_{Cext} reaches zero, the next switching period starts and the whole process will repeat again. By controlling the duty cycle of the corresponding control switch, the effective capacitance connected into the control port can be controlled. The equivalent control capacitance can be approximated as

$$C_{\text{ctrl}} = C_{\text{ext}} \cdot \frac{1 - \cos(2\pi D)}{2}. \tag{3.6}$$

Ideally, For the duty cycle of S_{ctrl} D varying from 0 to 0.5, a full range of equivalent external capacitance C_{ctrl} from 0 to C_{ext} can be achieved. In addition, the body diode of S_{ctrl} always conducts before the turn on of S_{ctrl} in this operation. Therefore, ZVS is ensured for S_{ctrl}.

Based on this control method, the open-loop control-to-output gain can be ploted in Fig. 3.14a, where one pole and one double pole can be observed. Based on the open-loop gain, a type II compensator using operational transconductance amplifier (OTA) can be utilized to complete the closed-loop PWM control, shown in Fig. 3.15. The output voltage is sensed and then compared with a reference

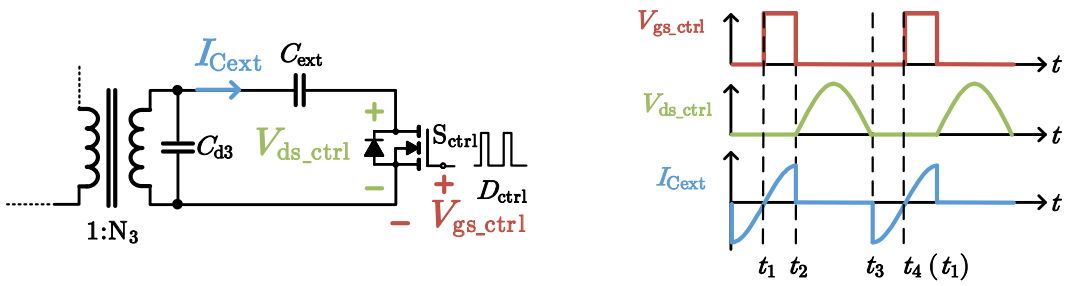

(a) (b)

Figure 3.13: Implementation and instruction waveforms of duty cycle controlled switched capacitor.

voltage using an OTA. The output of OTA is connected to the PWM comparator in Fig. 3.15. A compensation RC network is employed at the output of the OTA to improve the stability of the closed loop system. This RC network combines a pole/zero pair plus an origin pole for a high dc gain. Fig. 3.14b shows the loop gain. Phase marge of and gain margin of can be achieved based on simulated closed-loop gain.

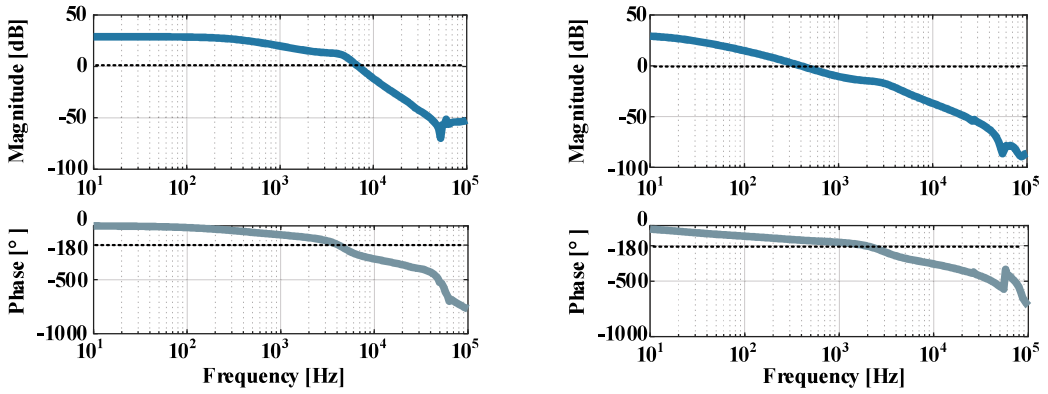

(a) (b)

Figure 3.14: Bode plots of (a) Open-loop and (b) closed-loop control-to-output gain.

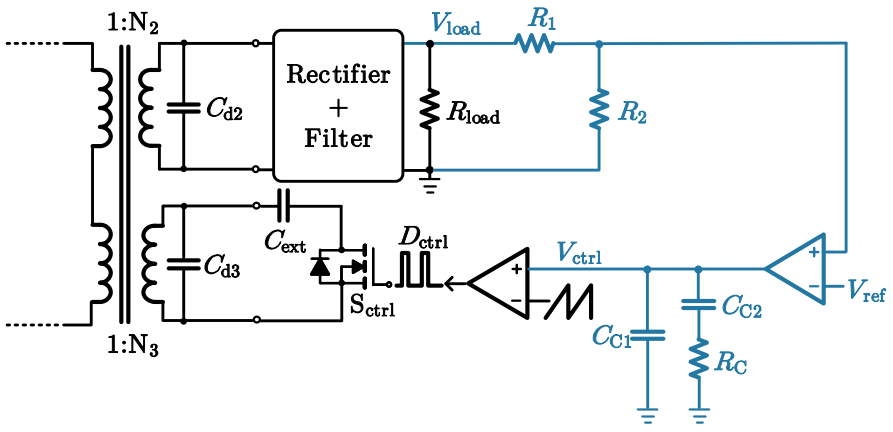

Figure 3.15: Implementation of the control feedback loop.

3.4 Experimental Results

A hardware (8.5 cm × 6.2 cm × 1.7 cm) is built to verify the analysis stated above, shown in Fig. 3.16. Fig. 3.17 displays the waveforms for control switch at different input and output conditions. Fig. 3.17a shows the gate signal of the control switch V_{gsctrl}, the drain to source voltage V_{dsctrl}, and the voltage across the load resistor V_{load} under 230 V input voltage and 100 W output power. For this case, the duty cycle for the control switch is 0.025. Fig. 3.17b shows the waveforms under 230 V input voltage and 50 W output power. For this case, the duty cycle for the control switch is adjusted by the control loop to 0.28 so that the load voltage is still regulated at 28 V. Fig. 3.17c shows the waveforms under 150 V input voltage and 50 W output power. For this case, the duty cycle for the control switch is adjusted by the control loop to 0.05. Both line regulation and load regulation are verified.

Table. 3.4 compares values of the components and the converter specifications of designs with dc output inductor and AC output inductor. For both design, the optimal switching frequency is decided by doing frequency sweep. Fig. 3.18 shows the comparison of the measured efficiency. It can be verified that, the AC L_{o} case has better regulation ability and requires less control capacitance. The AC L_{o} case has better efficiency than the dc L_{o} case in the full load range, which fully shows

Figure 3.16: Test board.

the advantages of the AC L_o. Moreover, the output inductance value of the AC L_o case is smaller than that in dc L_o case, while the trade-off is that the value of the L_{in} of AC L_o case is larger than that in dc L_o case.

Table 3.4: Comparison of converter specifications.

	C_{ext} [nF]	V_{in} [V]	V_o [V]	Frequency [kHz]	Regulation	Full Load Eff.	10% Load Eff.
Dc L_o	1000	230	28	58	100% - 3%	93.20%	71.10%
AC L_o	10	180	28	59	100% - 0.15%	93.40%	90.00%

3.5 Conclusion

This chapter illustrates the working principle of the tunable PT and provides the design method of tunable PT-based dc-dc converters. The gain characteristic of tunable PT changes with the impedance connected at the auxiliary control port. A PWM controlled switched capacitor is connected at the control port. For different load or input conditions, this switched capacitor presents proper capacitance at the control port to regulate the output without the need for changing the operation frequency. The fixed frequency operation allows the tunable PT to be operated near its optimum switching frequency, and renders the highest efficiency. A closed-loop control scheme for output voltage regulation is presented. Four tunable PTs with power rating ranging from 30 W to 100 W are tested with the proposed dc-dc

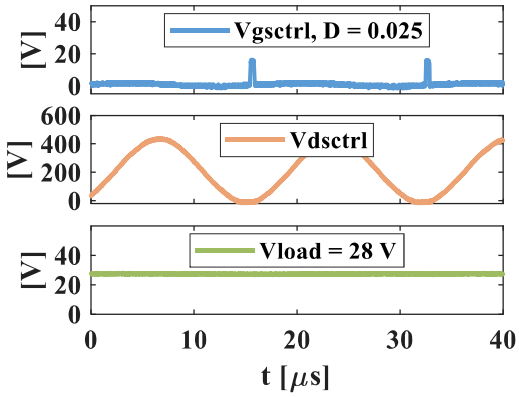

(a) Vin = 230 V, Po = 100 W

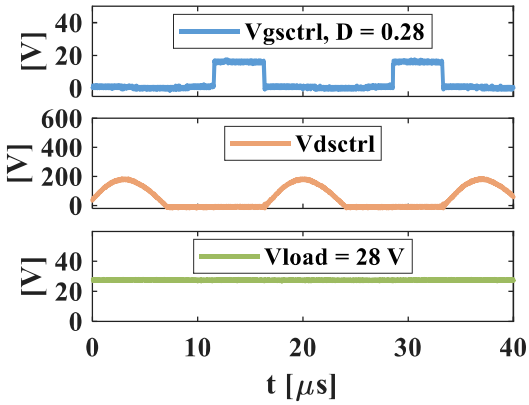

(b) Vin = 230 V, Po = 50 W

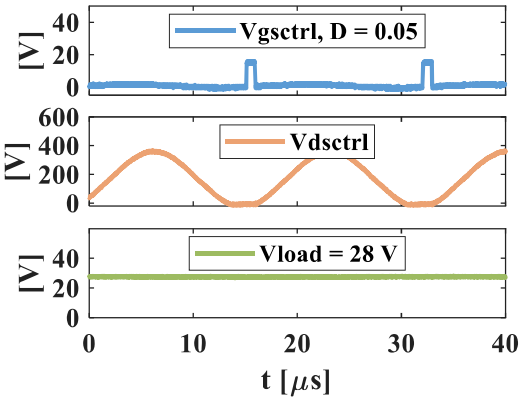

(c) Vin = 150 V, Po = 50 W

Figure 3.17: Experimental Waveforms.

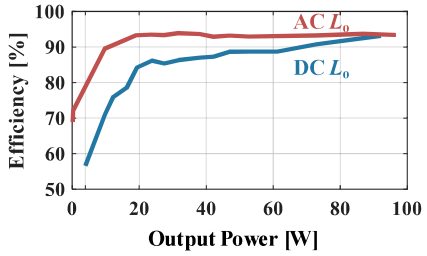

Figure 3.18: Measured efficiency comparison.

converter prototype to validate the design.

In addition, the design with dc output inductor and AC output inductor are compared. The AC output inductor works together with the input LC tank and output capacitor to form a LC-Series-CL topology to provide better regulation ability for the converter. Meanwhile, smaller external control capacitor is required. The AC output inductor also works as the output impedance matching network to compensate the circulating current of the output capacitor of the PT, which improves the efficiency of the converter. The trade off is that the design with AC output inductor requires larger input inductor based on the parameters of the given tunable PT sample if no extra input capacitor is used. The analysis is verified by the experiment.

Chapter 4

Rosen-type PT-Based High Step-Down Voltage-Ratio Dc-dc Converter

4.1 Introduction

In medium-/high-voltage power electronics systems, auxiliary power supplies are required to provide stable voltage and power for functional parts such as gate drivers, signal processors, and sensors. The required supply voltages range from several volts to tens of volts, which can be generated from either the internal dc bus of the converter, or an external low-voltage power supply. For the auxiliary power supply fed from the dc bus, although no external low-voltage bus is required, the high input voltage and high step-down ratio will bring challenges. In addition, a wide input range design is also preferable in order to achieve a lower wake-up voltage.

To achieve the high step-down voltage ratio, the most straightforward option is to use cascaded buck converters [112], as displayed in Fig. 4.1a. By rearranging the positions and connections of the switches in cascaded buck converter, quadratic buck converter can be derived [112, 113] as shown in Fig. 4.1b. With a cascaded or quadratic structure, the voltage conversion ratio equals D^2, where D is the duty ratio of the main switch. But the extreme low duty cycle is still unavoidable in order to achieve a step-down ratio higher than 100. To further increase the step-down ratio, switched capacitor and switched inductor cells are proposed to be inserted

into the buck or the quadratic buck converter [114–123]. The step-down ratio of the classical buck converter is doubled when combined with one switched capacitor or inductor cell. Fig. 4.1c is the example with one switched inductor cell. However, the step-down ratios of these methods are limited to 200.

By using coupled inductors (including flyback transformer which works as a coupled inductor), the voltage conversion ratio is modified to D/n, where n is the turns ratio. Fig. 4.1d displays the step-down converter with a coupled-inductor. In [122–125], coupled-inductors are used in the classical buck converter or the buck converter with switched capacitor cell. However, there are two issues with these types of converters. The first one is that wider voltage conversion ratio means a higher turns ratio, which leads to a larger size, higher conduction loss, and more complex inductor structure. In addition, in some leakage-inductance-sensitive typologies, such as the flyback converter, high leakage inductance brought by high turns winding requires careful design to avoid high voltage ringing. For example, [126] employs the two-switch flyback topology, as shown in Fig. 4.1e, to reduce the voltage stress of the switch and to eliminate the need for snubber circuits. The second issue is that, for these types of typologies, low voltage side output voltage or current needs to be sensed and compared to a reference value to control the main switch(es) at the high voltage side. This requires electromagnetic interference immunity for the control loop so that the control signals will not be interfered by the noise generated from the high voltage, high $\mathrm{d}v/\mathrm{d}t$ environment.

To avoid issues and drawbacks coming with high turns ratio coupled inductor and/or transformer, many researches have been done utilizing multilevel converter, modular input-series structure, and switched capacitor structure etc. The multilevel converter concept is used in [127–130] to provide a high step-down voltage ratio. One typical topology with flying capacitors is presented in Fig. 4.1f. Modular input-series structure, shown in Fig. 4.1g in [131–139], can be used to reduce the turns ratio of the transformer. Resonant voltage balancing circuit is another method to achieve a high conversion ratio featuring high power density [140–144] as shown in Fig. 4.1h. Reference [145] uses a stacked voltage balancing circuit to achieve open-loop auto voltage balancing. However, in this structure, the switches of the

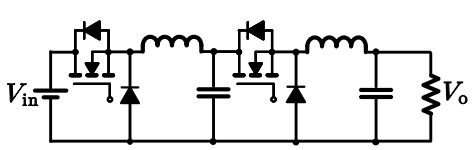

(a) Cascaded buck.

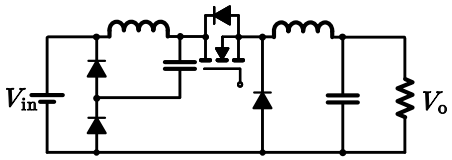

(b) Quadratic buck.

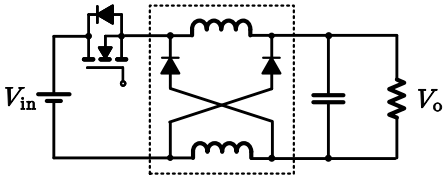

(c) Buck with switched inductor cell.

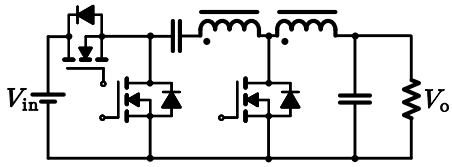

(d) Step-down with coupled inductors.

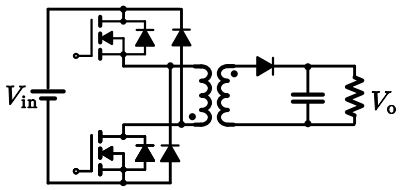

(e) Two-switch flyback.

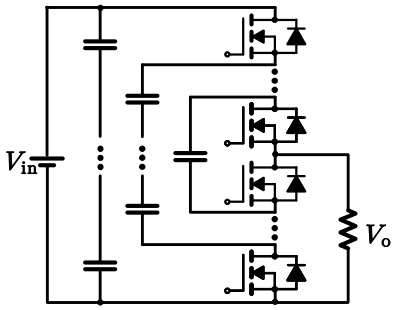

(f) Multilevel converter.

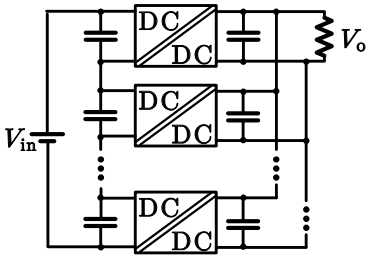

(g) Modular input-series structure.

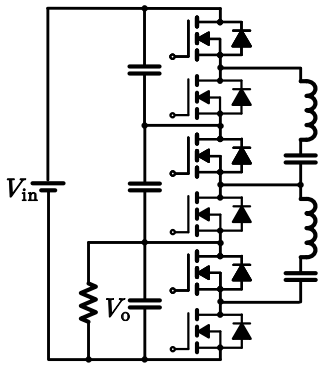

(h) Switched capacitor converter.

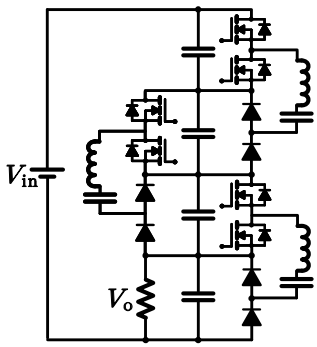

(i) Improved switched capacitor converter.

Figure 4.1: High step-down voltage-ratio solution examples in previous literature.

balancing circuit have to be controlled synchronously for the proper operation of the system. To eliminate this requirement, [146,147] propose a new interleaved structure to further simplify the control. The proposed structure of [147] is displayed in Fig. 4.1i. However, to achieve a step-down ratio of N, $2(N-1)$ switches are needed.

An alternative solution is to use a Rosen-type piezoelectric transformer (PT) to facilitate the voltage conversion with a high voltage conversion ratio. Among many types of PTs, Rosen-type PT features natural mechanisms for a high voltage conversion ratio in a compact planar form. It has been widely used in step-up configuration to provide high output voltage given low input voltage for applications such as plasma generator [148] and cold cathode fluorescent lamp driver [149]. Contrary to traditional applications, this work uses the Rosen-type PT reversely to provide a high step-down voltage ratio so that high turns-ratio transformers or complex cascaded converter structures can be eliminated. A 1:1 magnetic transformer can be used to provide isolation since the high and low voltage ports of commercially available Rosen-type PTs share a common ground. A low voltage buck-boost stage is used afterwards to regulate the output voltage. The control of the buck-boost stage locates at the low voltage side without crossing the insulation barrier.

The remaining sections of this article are organized as follows: section 4.2 illustrates the detailed design procedure of the proposed converter. The proposed design is validated by a prototype with experimental results in section 4.3. Finally, the conclusions of this article are drawn in section 4.4.

4.2 Design Procedure

Fig. 4.2 displays the overall block diagram of the proposed high voltage, high step-down voltage-ratio converter, taking the advantage of the low-profile Rosen-type PT. First, a dc-ac stage is needed after the DC bus to generate the AC input for the PT. The dc-ac stage is operated under constant switching frequency. By doing so, two advantages can be achieved. One is that it does not require control on high voltage side. The other is that high efficiency of the PT stage can be ensured since PT's efficiency would drop significantly if operating away from its fundamental

frequency of the intrinsic mechanical resonance based on the analysis in previous chapters. After the PT steps down the voltage, a planar magnetic transformer can be used to provide the isolation since the current commercial Rosen-type PT is non-isolated. Since the low profile PT has already stepped down the high bus voltage, instead of using a bulky high turns ratio magnetic transformer, a planar PCB transformer with 1:1 transfer ratio is implemented. After the isolation stage, a regulated AC/DC stage is used before the load. The control can be realized at the low voltage side without crossing the insulation barrier. The following parts of this section illustrates the detailed design procedure.

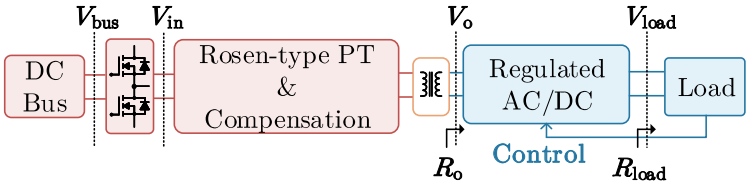

Figure 4.2: Block diagram of proposed Rosen-type PT-based high input voltage, high step-down voltage-ratio dc-dc converter.

4.2.1 Selection of Compensation Network and Operation Frequency

As stated in the previous section, PT can provide better performance if additional compensation component(s) is(are) used.

For the application of the bus-fed auxiliary power supply in medium-/high-voltage power electronics systems, no input compensation components will be used. The reasons are stated as follows. First of all, the resonance of series input inductor and input capacitor of the PT will cause PT's input voltage higher than the dc bus, which requires PT with a higher voltage rating. Therefore, a series input inductor is not desired. Secondly, even though parallel input inductor doesn't increase the PT's voltage rating and can enlarge operation range with inductive impedance, the small C_{in} of the sample Rosen-type PT requires an input inductor with several henries. Additional external input capacitor could help to reduce the required parallel input compensation inductance but would lead to high current in the parallel inductor,

which would cause undesired extra loss. In addition, for this application, zero voltage turn-on is not an essential requirement since the input current is in the milli-amperes range, which leads to small switching loss.

Therefore, only output compensation will be used. For the compensation inductor, there are two options, series or parallel. Both of them can improve PT's efficiency. As stated in section 2.4.2, the difference lies in that the series inductor provides better efficiency at heavier load with a narrower high-efficiency load range while the parallel one provides better efficiency at lighter load with a wider high-efficiency load range. For the proposed converter, a 1:1 magnetic transformer will be applied after the PT stage, which contributes to a magnetizing inductor physically connected in parallel to the output of the PT. This magnetizing inductor can be used as the output parallel compensation inductor of the PT, so that no extra physical component is needed. Therefore, parallel compensation is selected.

In addition, when operating at the series resonant frequency, with the parallel output inductor also in resonance with the output capacitor, the PT can provide constant voltage gain when the effect of the loss resistances in the system is neglected, which makes the control of the subsequent circuit easier. For the sample PT, the series resonant frequency equals to $\frac{1}{2\pi\sqrt{LC}} = 49\,\text{kHz}$. Even if this point is not the maximum efficiency point, it still can ensure high-efficiency operation of the PT, which can be predicted by Fig. 2.12d. Therefore, the switching frequency, as well as the resonance frequency of L_{op} and C_{o}, is selected as the series resonant frequency, which is $\omega^2 = L_{\text{op}}C_{\text{o}} = LC$.

Additional external output capacitor C_{oext} is not selected. In order to achieve $\omega^2 = L_{\text{op}}C_{\text{o}} = LC$, the required L_{op} is $54\,\mu\text{H}$, which is a reasonable value. Extra C_{oext} contributes to smaller L_{op} but smaller L_{op} means higher current of L_{op} which will cause extra loss.

In summary, only the parallel output inductor L_{op} is employed for this application because it can be physically realized by the magnetizing inductance of the next stage 1:1 transformer. In addition, it can provide wide high efficiency range and approximately constant voltage gain when its value and the value of the operation

frequency meets $\omega^2 = L_{\text{op}}C_{\text{o}} = LC$.

4.2.2 Selection of Input Dc-ac Stage

Once the compensation network is fixed, the input dc-ac stage can be decided. Two common choices are full bridge and half bridge. From the voltage gain point of view, the difference between full bridge and half bridge is that, if only fundamental component is considered,

$$V_{\text{in}} = \begin{cases} \frac{4}{\pi} V_{\text{bus}} \sin \omega t, & \text{if full bridge,} \\ \frac{2}{\pi} V_{\text{bus}} \sin \omega t, & \text{if half bridge.} \end{cases} \tag{4.1}$$

With parallel output inductor L_{op} selected as the compensation component and $\omega^2 = L_{\text{op}}C_{\text{o}} = LC$, output power of the PT P_{o} versus the equivalent output resistance of the PT R_{o} under different bus voltages with full bridge and half bridge can be plotted as Fig. 4.3a and Fig. 4.3b respectively. Usually there are four operation corners need to be considered, that are high line with full load, light line with full load, high line with light load, and low line with light load. These four operation corners are marked in Fig. 4.3, with 10% of the load taken as the lightest load in this work.

According to Fig. 4.3, with full bridge, the lowest input voltage is 335 V and the range of R_{o} is [2 Ω, 1430 Ω] with respect to the bus voltage range of [335 V, 1500 V]. While with half bridge, the lowest input voltage is 670 V and the range of R_o is [2 Ω, 355 Ω] with respect to the bus voltage range of [670 V, 1500 V]. Full bridge is selected as the input dc-ac stage since it has wider input range, which is important for a auxiliary power supply in medium-/high-voltage systems, though it requires a larger range of R_{o} and two more MOSFETs than half bridge.

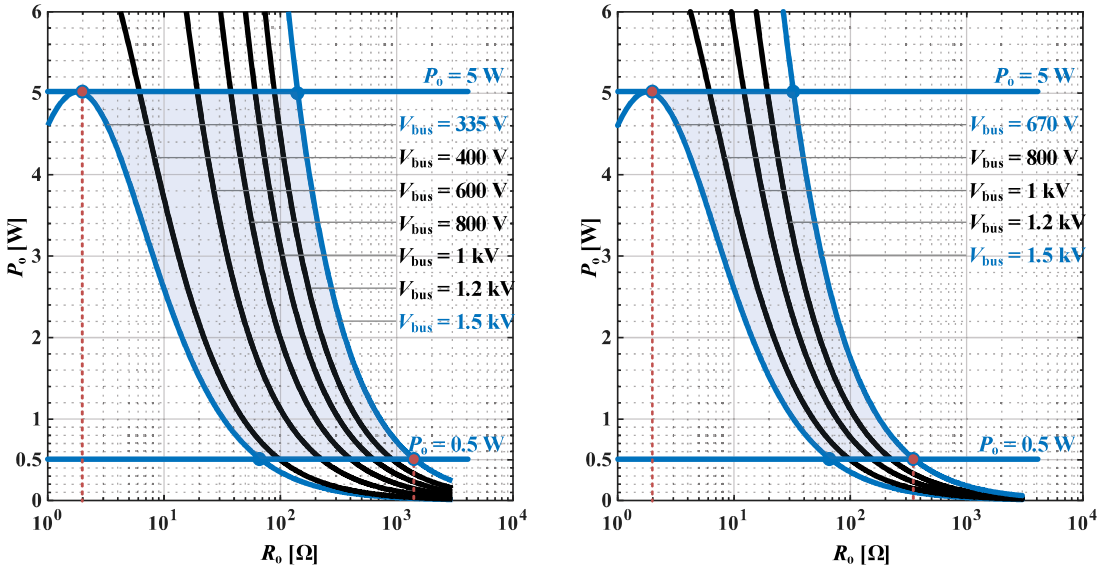

(a) Full bridge. (a) Half bridge.

Figure 4.3: PT output power vs. equivalent load resistance.

4.2.3 Selection of Output Ac-dc Stage

Assuming an ideal ac-dc stage, which means the loss is zero and the power factor equals one, the following equations can be derived,

$$g = \frac{V_{\text{load}}}{V_{\text{o,rms}}} = \sqrt{\frac{R_{\text{o}}}{R_{\text{load}}}}, \tag{4.2}$$

where g is the voltage gain of the ac-dc stage, V_{load} is the output voltage of the ac-dc stage, $V_{\text{o,rms}}$ is RMS value of the output voltage of the PT, R_{o} is the equivalent output resistance of the PT, and R_{load} is the load resistance of the ac-dc stage, as marked in Fig. 4.2.

Two extreme operation corners are low line with full load and high line with light load, marked as red dots in Fig. 4.3a. For low line full load,

$$R_{\text{load,LF}} = \frac{V_{\text{load}}^2}{P_{\text{load,nominal}}}. \tag{4.3}$$

For high line 10% light load,

$$R_{\text{load,HL}} = \frac{V_{\text{load}}^2}{0.1P_{\text{load,nominal}}}. \tag{4.4}$$

The nominal output power for the sample PT is 5 W. If the desired load output voltage is 5 V, then according to (4.3) and (4.4), $R_{\text{load,LF}} = 5\,\Omega$ and $R_{\text{load,HL}} = 50\,\Omega$. Based on the simulation result shown in Fig. 4.3a, the corresponding equivalent load resistance of the PT $R_{\text{o,LF}} = 2\,\Omega$ and $R_{\text{o,HL}} = 1430\,\Omega$. The corresponding required voltage gain range can be calculated using (4.2), which is $g \in [0.6, 5.3]$. This means a buck-boost type ac-dc stage is needed.

Continuous conduction mode (CCM) is selected since the voltage gain is only dependent on the duty cycle of the main control switch which reduces control complexity, while for discontinuous conduction mode (DCM) the voltage gain also depends on the circuit parameters. One-stage, a.k.a. bridge-less ac-dc topology, is not selected because extra current control loop is required for bridge-less ac-dc running in CCM in conventional control scheme [150, 151]. Therefore, two-stage solution, which is composed of a diode bridge cascaded with a buck-boost type circuit, is selected. For the buck-boost type circuit, the four switch buck-boost circuit is selected. The control of the system can be realized at the low voltage side, which is isolated from the noise at the high voltage side ground.

4.2.4 Design Criteria of 1:1 Transformer

For the design of 1:1 planar transformer, these aspects need to be considered: a) insulation voltage, b) magnetizing inductance, and c) leakage inductance.

- *Insulation voltage*

Considering the highest bus voltage, which is 1.5 kV with additional voltage ringing, a 4.5 kV voltage rating is selected to provide safe insulation.

- *Magnetizing inductance*

According to the analysis in section4.2.1, the desired magnetizing inductance equals to 54 µH. Based on the simulation result in Fig. 4.3a, for 1 kV nominal bus voltage and the load ranging from full to 10% load, the range of R_{o} is [60 Ω, 640 Ω]. Fig. 4.4a shows the voltage gain and efficiency curves with magnetizing inductance

L_m has a plus/minus 20% deviation for R_o ranging from 60 Ω to 640 Ω. It can be seen that the deviation of L_m has more significant effect on efficiency than gain. And negative deviation causes larger drops of gain and efficiency. For the operation under nominal bus voltage 1 kV and full output power 5 W, which correspond to 60 Ω R_o, the efficiency of the PT is 92.5% if with exactly matching magnetizing inductance. When operating at nominal bus voltage and nominal output power, to achieve PT's efficiency which is higher than 90%, the allowable range of the magnetizing inductance is from 43 µH to 75 µH.

- *Leakage inductance*

The effects on gain and efficiency caused by the leakage inductance are plotted in Fig. 4.4b and Fig. 4.4c. Different from magnetizing inductance, leakage inductance has more significant effect on gain than efficiency. In addition, primary side leakage is more critical. To maintain gain error within 1%, the primary leakage inductance should be smaller than 500 nH.

In summary, the design criteria for the planar 1:1 transformer is to achieve a) insulation voltage larger than 4.5 kV, b) magnetizing inductance in the range of [43 µH, 75 µH], with the target equals to 54 µH, and c) leakage inductance as small as possible, with primary leakage inductance no larger than 500 nH.

4.3 Experimental Results

Based on the analysis in 4.2, the overall converter schematic is drawn in Fig. 4.5, with components marked on the photo of the hardware. After the dc bus, a full bridge is operating with complementary gate signals at a constant frequency of 49 kHz to generate the AC input voltage for the Rosen-type PT. A 1:1 PCB winding planar magnetic transformer is used afterward to provide isolation. The magnetizing inductance is built to meet $\omega^2 = L_{op}C_o = LC$ so that two benefits can be achieved. One is to improve the efficiency of the PT and the other one is to provide approximately constant voltage gain, as analyzed in 4.2. Diode bridge cascaded with a four switch buck-boost is used as the output regulation stage. The four

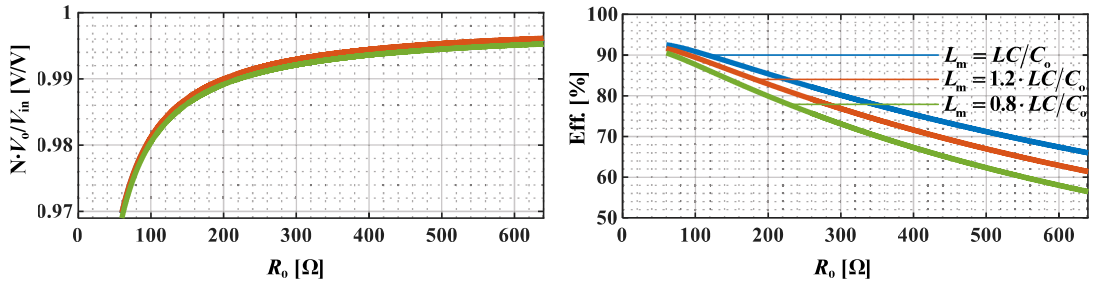

(a) Impacts of deviation of magnetizing inductance.

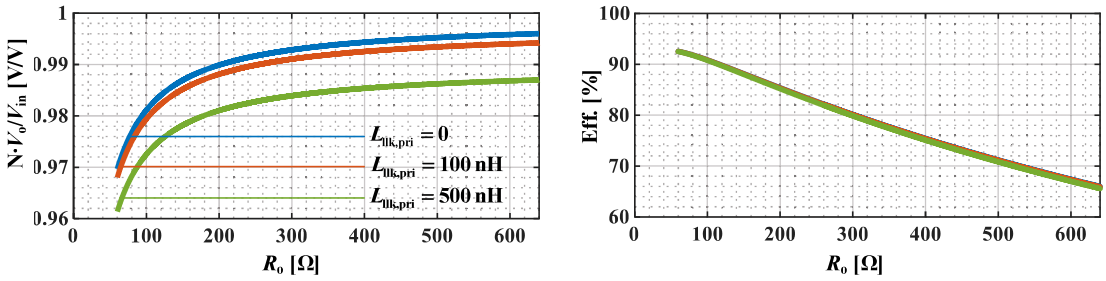

(b) Impacts of primary leakage inductance.

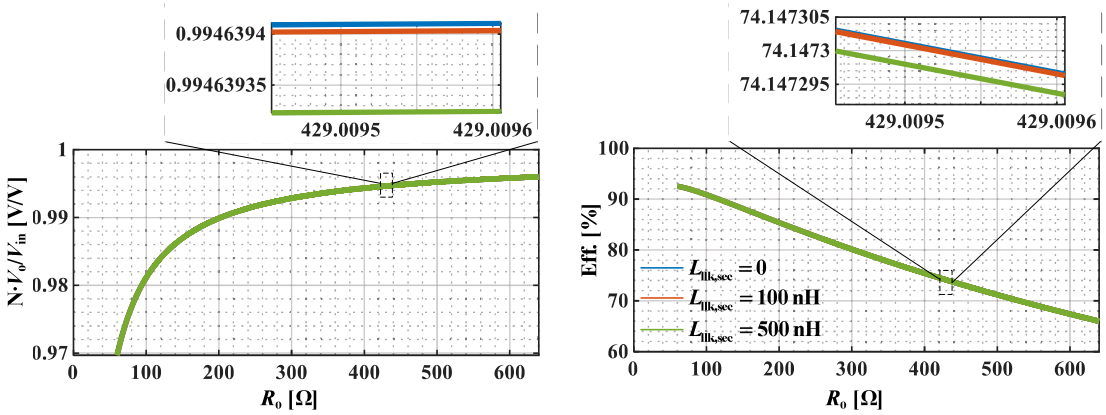

(c) Impacts of secondary leakage inductance.

Figure 4.4: Impacts of parameters of 1:1 planar transformer.

switch buck-boost is composed of the LTC3115 controller with integrated switches and an external inductor, working at 750 kHz in CCM with voltage-mode control. The control loop is completely isolated from the high voltage side.

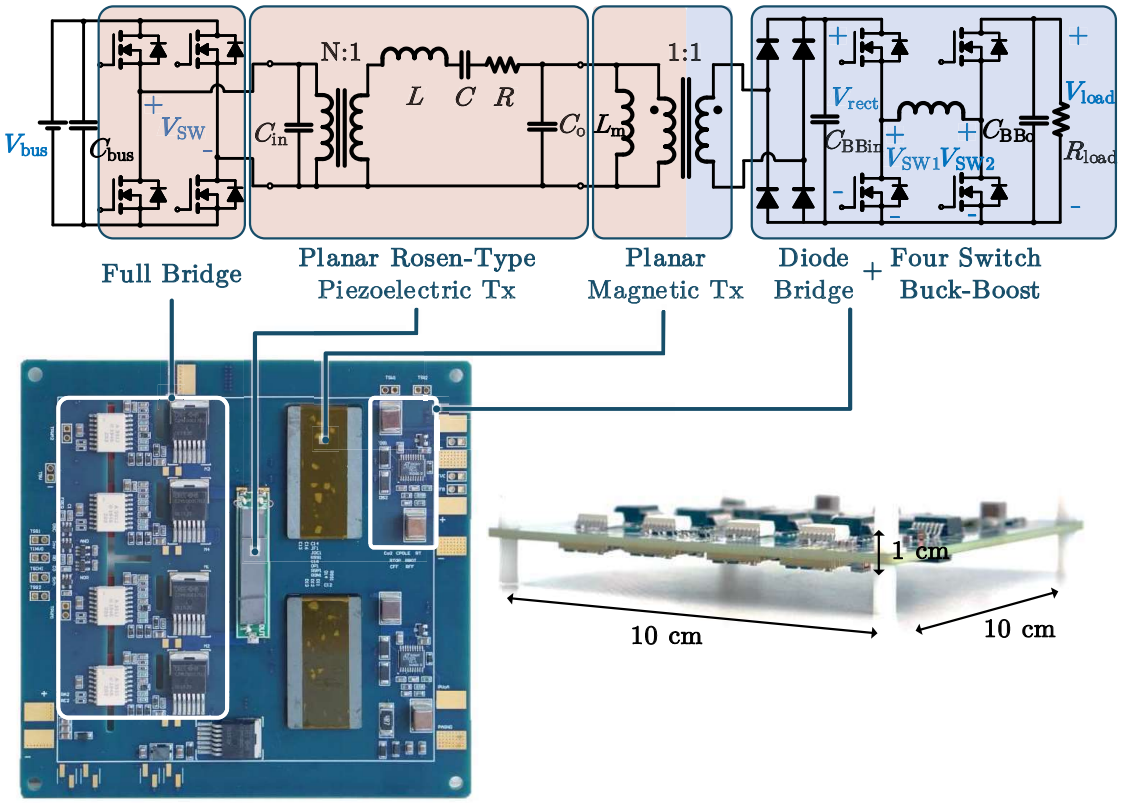

Figure 4.5: Schematic and prototype photo of proposed Rosen-type PT-based high step-down voltage-ratio dc-dc converter.

Fig. 4.6 shows the winding structure of the planar transformer. Width and thickness of the trace are selected as 2 mm and 0.035 mm to meet the power rating requirement. Interleaved primary and secondary windings are utilized to ensure small leakage inductance. Using Isola 370HR (54 kV/mm dielectric strength) as the PCB dielectric material, the insulation voltage larger than 4.5 kV with aging of the material considered can be achieved with the thickness of 0.15 mm, which helps to ensure the small leakage inductance.

The core material is HITACHI ML29D. To achieve the desired magnetizing inductance, each side has 12 turns of the winding and the air gap is controlled to be 0.24 mm with the core size shown in Fig. 4.6. The measured magnetizing inductance is 56 µH and the primary side leakage inductance is 90 nH, which meet the

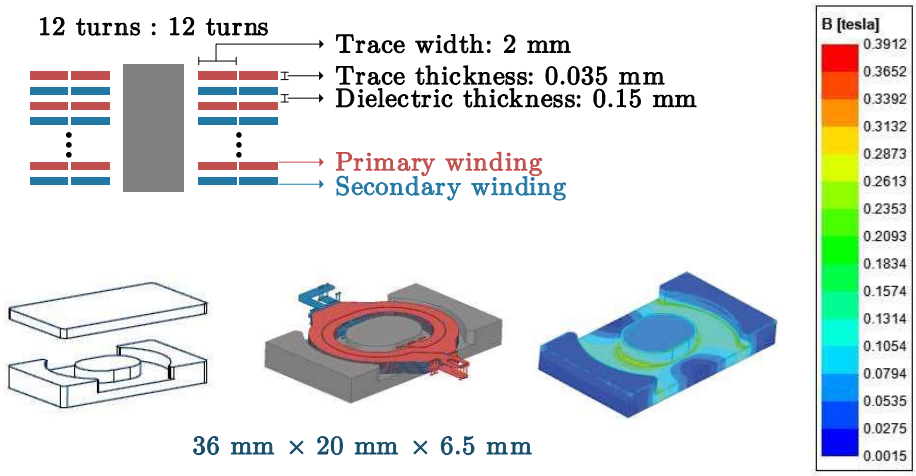

Figure 4.6: Customized 1:1 planar PCB winding transformer.

requirements listed in 4.2.4. Fig. 4.6 also shows the simulated flux density distribution when the converter is operated under the case with maximum magnetizing current. From this result, no saturation will happen in the core, whose saturation flux density is 430 mT at the temperature of 100 °C.

Fig. 4.7 displays the operational waveforms of the proposed converter working under different operating conditions as illustrated in the picture. In all four sets of waveforms, the first column shows the input voltage of the PT, whose higher platform value indicates the bus voltage; the second column shows the left switching node voltage V_{SW1} of the buck-boost stage, whose higher platform value indicates the output voltage of the diode bridge V_{rect}; and the final column shows the right switching node voltage V_{SW2} of the buck-boost stage, whose higher platform value indicates the output voltage of the converter V_{load}. Fig. 4.8 presents the output voltage regulation with less than 5% error for the bus voltages from 350 V to 1 kV.

For different load conditions, the achievable lowest and highest bus voltages are different, which are shown in Fig. 4.9. For load ranging from 0.5 W 10% load to 5 W full load, the achievable lowest bus voltage ranges from 200 V to 350 V and the achievable highest bus voltage ranges from 1 kV to 1.5 kV.

Fig. 4.10 shows the overall efficiency curve of the proposed converter working at nominal 1 kV input. Fig. 4.11 is the thermal figure for the proposed converter

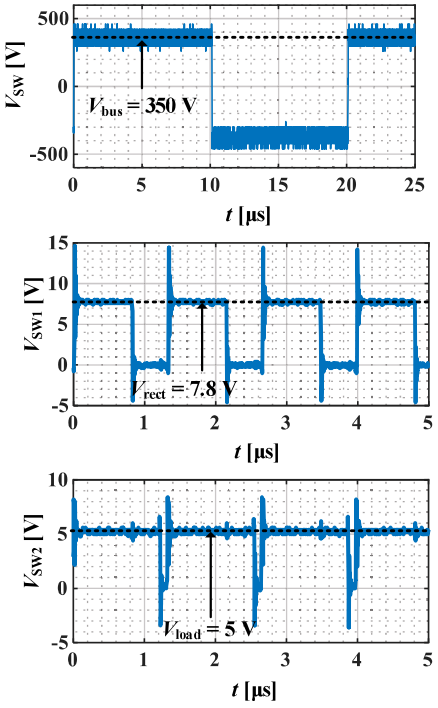

(a) 350 V input, 0.5 W output.

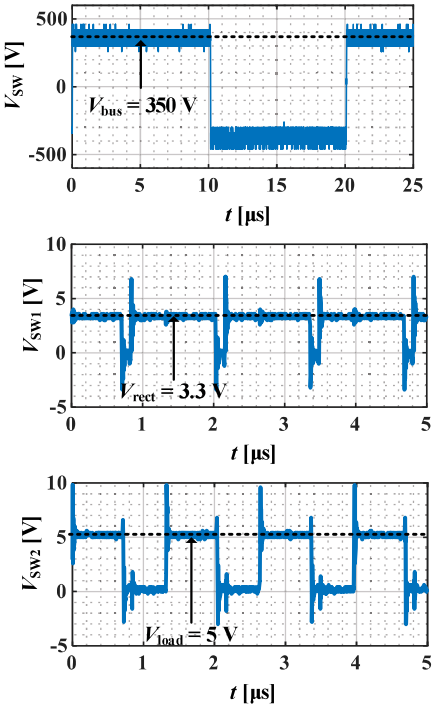

(b) 350 V input, 5 W output.

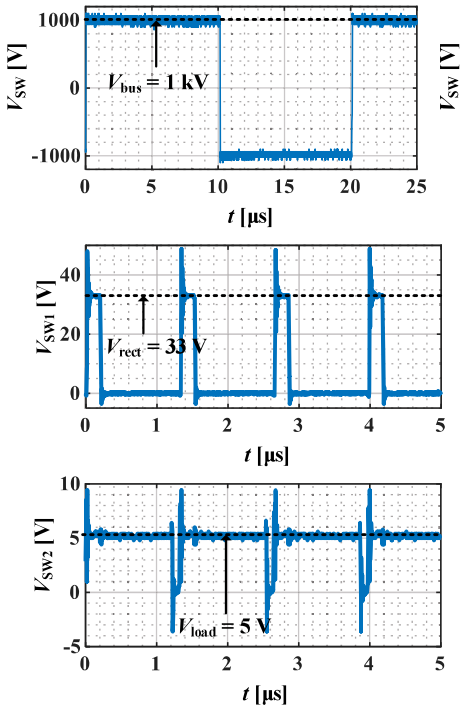

(c) 1 kV input, 0.5 W output.

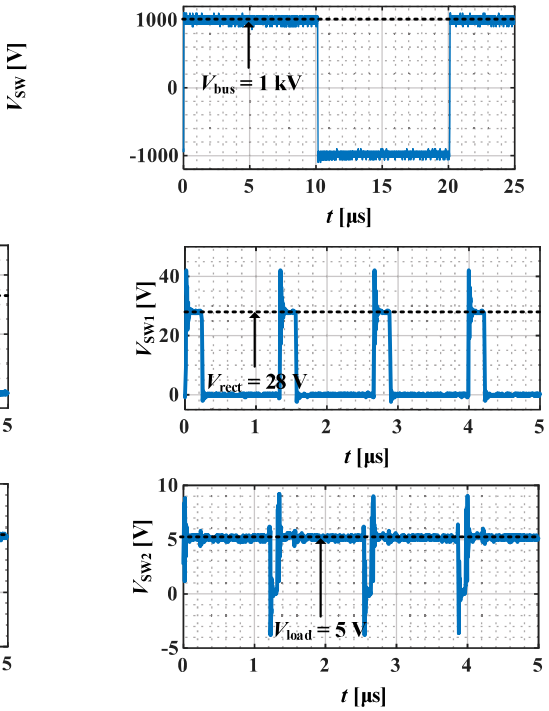

(d) 1 kV input, 5 W output.

Figure 4.7: Operational waveforms of proposed converter.

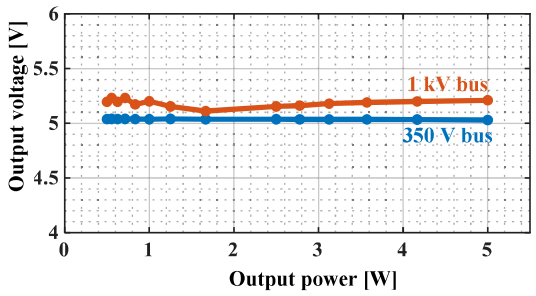

Figure 4.8: Output voltage regulation under 350 V and 1 kV bus voltages.

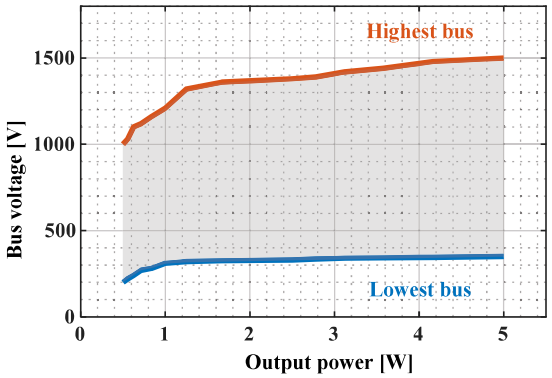

Figure 4.9: Dc bus voltage range with regulated output for different load conditions.

working continuously at nominal 1 kV input, 5 W output at room temperature. The highest temperature spot exits on the MOSFETs, whose temperature is 51.4 °C, which indicates no heat dissipation issue in the proposed converter.

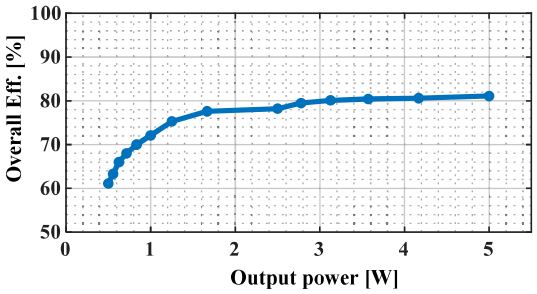

Figure 4.10: Overall efficiency under 1 kV bus voltage.

4.4 Conclusion

To the best of author's knowledge, Rosen-type PT is first proposed and verified to be applied in the step-down configuration in this work. Thanks to the physical

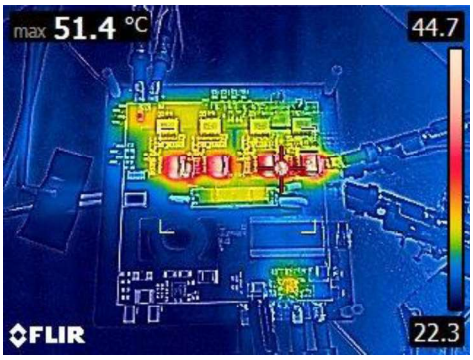

Figure 4.11: Working continuously at nominal 1 kV input, 5 W output at room temperature.

working mechanisms, Rosen-type PT provides high voltage conversion ratio in a compact planar form. This advantage can be taken into the design of converters that needs high step-down voltage ratio, i.e., dc bus-fed auxiliary power supplies in medium-/high-voltage systems. By eliminating bulky high turns ratio magnetic transformers, planar design can be achieved.

This work provides an example design of Rosen-type PT-based high step-down voltage-ratio dc-dc converter. The electrical characteristics of, by not limited to, the sample Rosen-type PT are first analyzed. Closed-form expressions of characteristic points are given. Impacts of the compensation components are also derived to improve the performance of a standalone PT. The detailed design procedure is then provided. Before the PT, a full bridge is used to provide lower star-up voltage of the system. After the PT, a 1:1 PCB winding magnetic transformer is used to provide the isolation, whose magnetizing inductance is utilized as the compensation inductor for a higher efficiency and an approximately constant voltage gain. A low voltage buck-boost stage is implemented afterwards to regulate the output voltage. This design does not require any closed-loop control at high voltage side. The proposed converter is verified by a 5 W prototype with the height of 10 mm.

Chapter 5

Power Converter for the Reversed Pyroelectric Thermodynamic Systems

5.1 Introduction

In recent years, several emerging technologies in the domain of solid-state physics have been investigated as alternatives for future refrigeration, heat pumping, or power generation applications. Solid-state heating/cooling technology is attractive because it avoids the use of refrigerants with large global warming potential which are widely used in traditional vapor compression systems and enables the development of compact devices for efficient thermal managements of buildings, vehicles, and optoelectronic devices. Of these technologies, the most developed technology in the field of small-scale refrigerators is magnetic refrigeration [152–161]. However, the disadvantages of this technology are the high costs associated with the magnetic field generation and the magnetic materials [162]. Reversed pyroelectric technology, revived by the discovery of giant reversed pyroelectric effect in [163] and [164] has quickly regained considerable attention from both academia and industry [23]. The major advantage of this technology over magnetic refrigeration is the fact that the high electric fields required for the reversed pyroelectric effect are much easier and less expensive to generate than magnetic fields. Furthermore, it is possible to produce a high electric field in a large volume that can be a good

advantage compared with permanent magnets. In the recent few years, significant research efforts have been made in the field of the reversed pyroelectric effect based thermodynamic systems [21, 23, 24, 159, 162, 165–223]. These research suggest the possibility for improvements in energy efficiency, compactness, noise level, as well as a reduction in environmental impacts, so it seems very probable that it may start to fill particular market niches as a replacement for vapor-compression technology in the future.

As stated in section 1.3, in the Brayton thermal cycle, an adiabatically applied electric field results in an increase in the temperature of a pyroelectric material because of the lattice vibration entropy compensation of the reduction of the dipolar subsystem entropy. After that, heat is released due to the temperature difference. In contrast, the adiabatic removal of the field causes cooling of the pyroelectric material; that is, the temperature of the pyroelectric material decreases because of the decrease of the lattice vibration entropy, which compensates for the increase of the dipolar subsystem entropy. The material will absorb heat to be back to the origin state. In practice, there are two different approaches that have been in use to describe the theory and calculate the physical quantities in reversed pyroelectric effect [21, 224]: (a) the Maxwell approach and (b) the Landau phenomenological approach. In principle, these two approaches are equivalent and which of them is more suitable depends on the particular problem under investigation.

- Maxwell approach

  A solid material that is subjected to a small change in strain $\mathrm{d}\varepsilon_{\mathrm{m}}$, electric displacement $\mathrm{d}D$ and entropy $\mathrm{d}S$, is described by the first and second law of thermodynamics by a change in the integral energy $\mathrm{d}U$ as follows

$$\mathrm{d}U = \sigma \mathrm{d}\varepsilon_{\mathrm{m}} + E\mathrm{d}D + T\mathrm{d}S, \tag{5.1}$$

  where σ, E, and T are stress, electric field and temperature, respectively. Since in most experimental situations temperature, electric field and stress are independent variables, a Legendre transformation can be performed by

defining Gibbs free energy, G, as follows [225, 226]:

$$G = U - \sigma\varepsilon_{\mathrm{m}} - ED - TS, \tag{5.2}$$

whose differential form can be written as

$$\mathrm{d}G = -\varepsilon_{\mathrm{m}}\mathrm{d}\sigma - D\mathrm{d}E - S\mathrm{d}T. \tag{5.3}$$

Therefore, the reversed pyroelectric effect can be described by the adiabatic temperature change as follows

$$\mathrm{d}T = -\frac{T}{C}\left(\frac{\partial D}{\partial T}\right)_{\sigma,\mathrm{E}}\mathrm{d}E, \tag{5.4}$$

where C is the heat capacity per unit volume. By formally integrating (5.4), one obtains the adiabatic temperature change as

$$\Delta T = \int_{E_1}^{E_2} -\frac{T}{C}\left(\frac{\partial D}{\partial T}\right)_{\sigma,\mathrm{E}}\mathrm{d}E. \tag{5.5}$$

- Landau phenomenological approach

  A typical system investigated in the reversed pyroelectric experiments consists of a set of dipolar degrees of freedom embedded in a weakly polarizable environment, such as a crystalline or ceramic insulating material. The entropy of the system can be written as the sum of the entropy of the weakly polarizable lattice $S_{\mathrm{latt}}(T)$ and the entropy of the dipolar part $S_{\mathrm{dip}}(E,T)$. The total change of entropy in an adiabatic reversed pyroelectric process must be zero, which implies

$$\Delta S(E,T) = \Delta S_{\mathrm{latt}}(T) + \Delta S_{\mathrm{dip}}(E,T) = 0. \tag{5.6}$$

  By assumption $S_{\mathrm{latt}}(T)$ does not depend on the field; thus, its change on going from T_1 to T_2 can be evaluated as an integral over the lattice heat capacity C_{latt}, that is,

$$\Delta S_{\mathrm{latt}}(T) = \int_{T_1}^{T_2} \frac{C_{\mathrm{latt}}(T)}{T}\,dT \approx C_{\mathrm{latt}}(T_1)\log\left(\frac{T_2}{T_1}\right). \tag{5.7}$$

Based on (5.6) and (5.7),

$$T_2 = T_1 \exp\left[\frac{S_{\text{dip}}(E_1, T_1) - S_{\text{dip}}(E_1, T_2)}{C_{\text{latt}}(T_1)}\right]. \tag{5.8}$$

The dipolar entropy $S_{\text{dip}}(E, T)$ can be calculated by considering the Landau free energy of the dipolar subsystem:

$$F = F_0 + \frac{1}{2}aP^2 + \frac{1}{4}bP^4 + \frac{1}{6}bP^6 + \frac{1}{8}bP^8 + ... - EP, \tag{5.9}$$

and

$$S_{\text{dip}} = -\left(\frac{\partial F}{\partial T}\right)_{\text{E}}, \tag{5.10}$$

where F_0 is the field-independent configurational part and $P = P(E, T)$ is a scalar order parameter representing the dielectric polarization [?,?]. In general, the parameter $a = a(T)$ is temperature dependent and its precise form is related to the type of system under consideration. The remaining parameters b, c, d, and so on are commonly assumed to be temperature independent [227]. Therefore, (5.8) can also be expressed as

$$T_2 = T_1 \exp\left\{\frac{1}{2C_{\text{latt}}(T_1)}\left[a_1(T_2)P^2(E_2, T_2) - a_1(T_1)P^2(E_1, T_1)\right]\right\}, \tag{5.11}$$

where $a_1 = \mathrm{d}a/\mathrm{d}T$ and P satisfies the equation of state, that is $(\partial F/\partial P)_{\text{T}} = 0$.

(5.11) indicates that to realize large reversed pyroelectric effect, it is necessary that there is a large entropy change associated with the polarization change in the material. Moreover, the dielectric material should be able to support large polarization change and these polarization changes can be induced effectively by external field. Of 10 crystal classes which are pyroelectric, some types of materials whose spontaneous polarization can be reversed by the application of an external electric field are called as ferroelectric. Ferroelectric material provides good reversed pyroelectric effect because of strong polarization as well as the strong dependence of dielectric properties on temperature. In addition, in ferroelectric materials, the change of polarization is large at the vicinity of the ferroelectric (polarization ordered)-paraelectric (polarization disordered) phase transition, which is

a significant benefit for reversed pyroelectric applications. Furthermore, in first-order phase transition ferroelectric materials, external electric filed can induce phase transition, which will lead to a latent heat, which is desired for large reversed pyroelectric temperature change. Therefore, it is advantageous to use these ferroelectric materials for the reversed pyroelectric applications and operate these materials at temperatures just above the ferroelectric-paraelectric phase transition where the largest electric field induced polarization change in the material can be achieved. Among many types of ferroelectric materials, relaxor ferroelectric offer several advantages for reversed pyroelectric devices, e.g., infinite states without applying electric field, field-induced large polarization, no-hysteresis of heating and cooling, small-hysteresis polarization loss, room temperature phase transition, and broad temperature range [228]. Specifically, high-energy electron irradiated poly(vinylidene fluoride–trifluoroethylene-chlorofluoroethylene) (P(VDF–TrFE-CFE)) or P(VDF–TrFE-CTFE)(chlorotrifluoroethylene) terpolymers or irradiated P(VDF-TrFE) relaxor copolymers ferroelectric thin films are promising for realizing large reversed pyroelectric responses because of additional advantages such as strong electric field achieved under voltages normally used in commercial heating or cooling devices, light weight and fracture tolerance.

Heat can be transferred from/to the heat source and the heat sink or via thermal switches or by a secondary regenerator. In the first case, there is not an external regenerator because the regeneration process can be realized by direct heat transfer between contacting pyroelectric elements moving in opposite directions with different applied fields [172, 229]. The system can be realized with a set of pyroelectric materials and thermal switches. The latter absorbs/ rejects the heat to/from the pyroelectric material. Despite the discontinuous operation of thermal switches, the high frequency of the switching enables the continuous operation of the device, without the need for an oscillatory fluid flow. Thermal switches may be divided into two domains: solidstate and microfluidics. The second case is also called as active regenerator. Active regeneration is common in heat pumps that are based on materials with a low intrinsic temperature change because it permits the device to display a temperature difference between the hot and cold side of the regenerator

larger than the adiabatic reversed pyroelectric temperature change of the material. In the active regenerator concept, the pyroelectric material acts as a refrigerant as well as a regenerator. Many prototypes have been proposed following this same principle of regeneration [159,162,174,178,179]. The active regenerator can be solid or fluid.

Taken the fluid active regenerator as an example, as shown in Fig. 5.1 [178], The secondary fluid is used to transfer heat from the cold to the hot end of the regenerator. Substantially every section of the regenerator experiments its active regenerator cycle, according to the proper working temperature. Through an active regenerator one can appreciate a larger temperature span between the regenerator material and the auxiliary fluid. During the entire cycle, the electric field varies between a minimum value and a maximum one. The regenerator works between a warm reservoir T_{H} and a cold one T_{C}. The active regenerator cycle consists of four processes. During polarization (Fig. 5.1a), the electric field is increased with no fluid flow, which causes the increase of the temperature of the electric material due to reversed pyroelectric effect. In the cold-to-hot flow process (Fig. 5.1b) the secondary fluid blows from the cold to the hot end of the regenerator when the field has kept at a constant maximum value. The fluid absorbs heat from the bed, reaching a temperature above T_{H} and rejects it through a warm heat transfer. The next process is depolarization (Fig. 5.1c) where, with no fluid flow, the electric field is removed and the pyroelectric material temperature decreases as a consequence of the reversed pyroelectric effect. Finally (Fig. 5.1d), the heat transfer fluid flows through the bed from the hot to the cold end without an applied electric field. This hotter fluid cools the bed and reaches a temperature lower than T_{C}. At this stage the secondary fluid absorbs heat from a cold heat transfer, producing a cooling load.

During the reversed pyroelectric thermal cycle, as stated in section 1.3, part of the work done to drive representative cycles does not pump heat and may therefore be recovered to increase the coefficient of performance. Therefore, a reversed pyroelectric based thermodynamic system utilizing two sets of pyroelectric modules can be built. Once the system has been initialized, when pyroelectric module 1 is

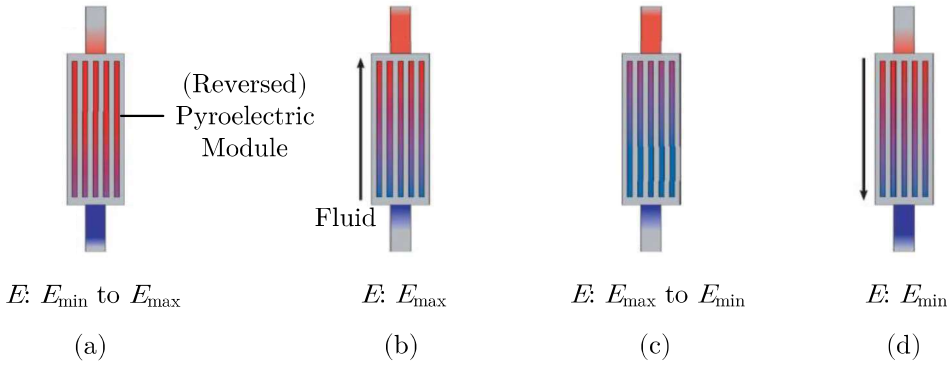

Figure 5.1: Active regenerator cycle with fluid regenerator.

discharged, pyroelectric module 2 can be charged utilizing the charge in pyroelectric module 1 and vice versa, as shown in Fig. 5.2.

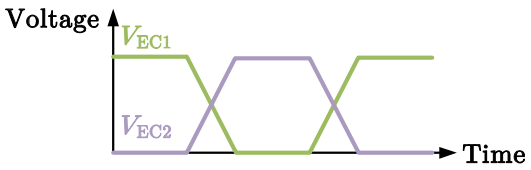

Figure 5.2: Voltage profile of dual module system.

To build a power converter for the dual module reversed pyroelectric effect based thermodynamic system, a circuit model is needed to provide sufficient information to devise a power conversion solution capable of driving the device. Most of existing literature focus on the steady state modelling of the temperature-dependent and voltage-dependent non-linearity of the ferroelectric capacitor [188–190, 192, 193, 197, 199, 230, 231], which only provides the information of the pyroelectric material during polarization and de-polarization process while lacks the information during heat exchange process. [232, 233] provide the transient modelling of ferroelectric capacitors. However the link between the mathematical expression and the practical phenomenon, which is the physical meaning of the model is absent. In addition, despite many pyroelectric devices have been proposed, the driving electrical field are provided by function generator cascaded by bulky power amplifier. This work proposes a circuit model to characterize both the static and dynamic behavior of the material based on the physical behavior. A power converter is then designed and implemented to provide desired driving and energy recycling capabilities for

the dual module reversed pyroelectric effect based thermodynamic system.

The remaining sections of this article are organized as follows: section 5.2 presents the electrical characterization of the material and proposed the behavior circuit model for the material. Based on the circuit model, section 5.3 proposed a circuit for the reversed pyroelectric effect based thermodynamic system, featuring system initializing, energy recovering, and loss compensation functions. The proposed design is validated by a prototype with experimental results in section 5.4. Finally, the conclusions of this article are drawn in section 5.5.

5.2 Electrical Characterization of the Material in Reversed Pyroelectric Effect

The voltage profile for the pyroelectric module is shown in Fig. 5.2. The voltage across the pyroelectric module steps from zero to the maximum value in a short time period, which is typically in the range of from several hundred milliseconds to several seconds. After being hold for several tens of seconds, waiting for the completion of the heat transfer, the voltage steps back to zero. The characterization of the electrical behavior of the pyroelectric module is conducted at low power with a single pyroelectric film sample. The thickness of the pyroelectric film is approximately equal to 10 µm. The length and width of the active region of the pyroelectric film are 9 cm and 7 cm respectively.

The desired driving voltage of the pyroelectric film is provided by the circuit in Fig. 5.3. A function generator is employed to control the drive voltage profile, which includes the time lengths for both polarization/depolarization and the heat transfer periods. High voltage amplifier is used afterwards to provide the desired excitation pulse voltage for the pyroelectric film. For the sample used in this work, the peak voltage value is limited to 400 V.

To measure the voltage-current characteristic of the pyroelectric film, the Sawyer-Tower circuit can be used. It was first proposed in [234], and has been widely used to measure ferroelectric hysteresis characteristic. The original circuit consists of

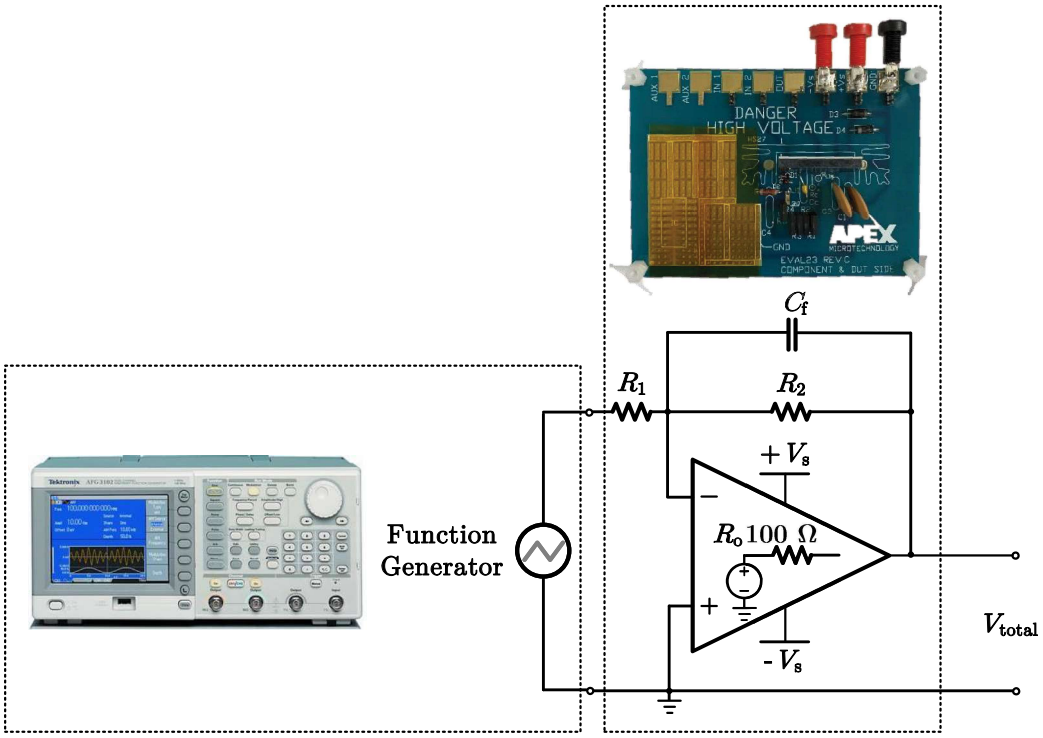

Figure 5.3: Drive circuit of the sample pyroelectric film.

two capacitors connected in series, as depicted in Fig. 5.4. One is the sample under test C_{EC} and the other one is a linear-known-valued sense capacitor C_{sense}. C_{sense} is chosen much greater than C_{EC} so that voltage drop across C_{sense} is much less than that across C_{EC}. So the total drive voltage V_{tot} is almost equal to voltage across C_{EC}. Since C_{EC} and C_{sense} are in series, the current flowing in C_{EC} equals that of C_{sense}, that is

$$I_{\mathrm{EC}} = I_{\mathrm{sense}} = C_{\mathrm{sense}} \cdot \frac{\mathrm{d}V_{\mathrm{sense}}}{\mathrm{d}t}. \tag{5.12}$$

However, when a oscilloscope is used to measure the voltage across C_{sense}, the resistance of the probes and leads to a higher order system, which increases the complexity of calculation. As depicted in Fig. 5.4, for example, C_{EC} is around 200 nF, so a 11 µF C_{sense} is selected. The equivalent impedance of the probe can be represented by a 10 MΩ resistance in parallel with a 3.9 pF capacitance. Compared to 11 µF C_{sense}, 3.9 pF C_{probe} is neglectable. Nevertheless, the existence of R_{probe}

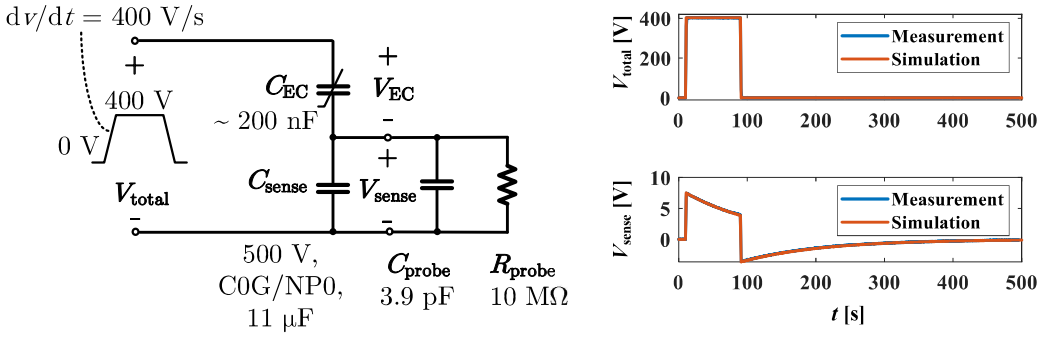

Figure 5.4: Origin Sawyer-Tower circuit.

leads to the inaccuracy if (5.12) is not modified to

$$I_{\mathrm{EC}} = I_{\mathrm{sense}} + I_{\mathrm{probe}} \approx C_{\mathrm{sense}} \cdot \frac{\mathrm{d}V_{\mathrm{sense}}}{\mathrm{d}t} + \frac{V_{\mathrm{sense}}}{R_{\mathrm{probe}}}. \tag{5.13}$$

A modification on the original Sawyer-Tower circuit can reduce the calculation complexity, that is a sense resistor R_{sense} can be used to replace C_{sense}, as presented in Fig. 5.5. The value of R_{sense} is selected such that the voltage across R_{sense} is much smaller than the voltage across C_{EC}. For example, for the 200 nF C_{EC} sample, 15 kΩ R_{sense} can be used so that with 400 V total applied voltage V_{total} and whose $\mathrm{d}v/\mathrm{d}t$ = 400 V s^{-1}, the peak value of the voltage across R_{sense} V_{sense} is less than 10 V. Therefore, the current flowing in the 3.9 pF C_{probe} can be neglected. The current flowing in C_{EC} can be simply calculated as

$$I_{\mathrm{EC}} \approx \frac{V_{\mathrm{sense}} \cdot (R_{\mathrm{sense}} + R_{\mathrm{probe}})}{R_{\mathrm{sense}} R_{\mathrm{probe}}}. \tag{5.14}$$

The Brayton reversed pyroelectric thermal cycle is depicted in Fig. 1.8 and redrawn here in Fig. 5.6 for the reader's convenience. It can be found from Fig. 5.6 that there are two sources for the charge movement during one thermal cycle: one is the voltage change during the periods from status 1 to status 2 and from status 3 to status 4; the other one is the entropy change during the periods from status 2 to status 3 and from status 4 back to status 1 when the voltage are kept constant. Therefore, without considering the resistive loss, the current flowing through the

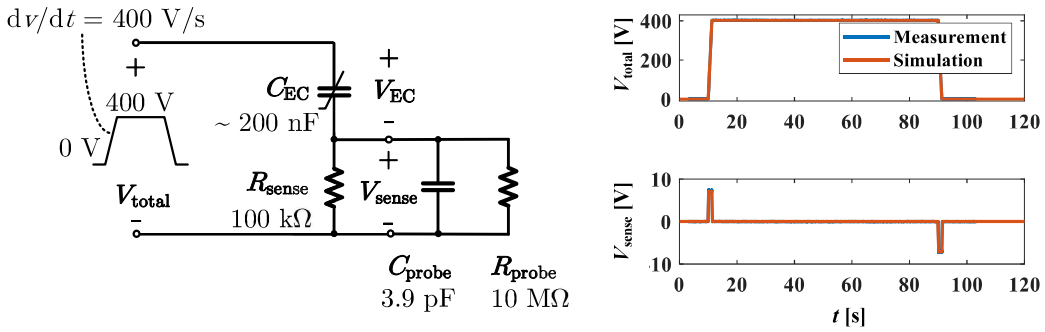

Figure 5.5: Measurement circuit of the sample pyroelectric film.

pyroelectric material can be modeled as

$$I_{\mathrm{EC}} = \frac{\mathrm{d}(q_{\mathrm{EC}}(V_{\mathrm{EC}}, S_{\mathrm{EC}})}{\mathrm{d}t} = \frac{\partial q_{\mathrm{EC}}}{\partial V_{\mathrm{EC}}} \cdot \frac{\mathrm{d}V_{\mathrm{EC}}}{\mathrm{d}t} + \frac{\partial q_{\mathrm{EC}}}{\partial S_{\mathrm{EC}}} \cdot \frac{\mathrm{d}S_{\mathrm{EC}}}{\mathrm{d}t}. \tag{5.15}$$

Therefore, if considering the resistive loss, the behavior of the pyroelectric material in the Brayton cycle can be modeled as Fig. 5.7. What is noteworthy is that the pyroelectric material during periods from status 2 to status 3 and from status 4 back to status 1 behaves like a pyroelectric generator, that is a charge change can be induced by the temperature change. In gernal, the pyroelectric generator is modeled as current source in parallel with a capacitor [235–237]. Since the pyroelectric effect is physically reversible. Therefore, it is reasonable to model the material used for reversed pyroelectric effect as the equivalent circuit in Fig. 5.7, which can be verified by the measured voltage and the current of the sample film presented in Fig. 5.8.

From status 1 to status 2, the zoomed-in waveforms are shown in the blue box in Fig. 5.8. The voltage-dependent capacitance can be calculated using the equation

$$C_{\mathrm{EC}}(V_{\mathrm{EC}}) = \frac{\mathrm{d}q_{\mathrm{EC}}}{\mathrm{d}V_{\mathrm{EC}}} = \frac{I_{\mathrm{EC}}}{\mathrm{d}V_{\mathrm{EC}}/\mathrm{d}t}. \tag{5.16}$$

The current waveform from status 2 to status 3 (in the red box in Fig. 5.8) verifies the existence of the entropy change induced current source. From status 2 to status 3, decrease of the entropy causes larger polarization of the material. Therefore, the charge increases. After the heat transfer is completed, the remaining current in the green box in Fig. 5.8 verifies the existence of the loss resistor. Ac-

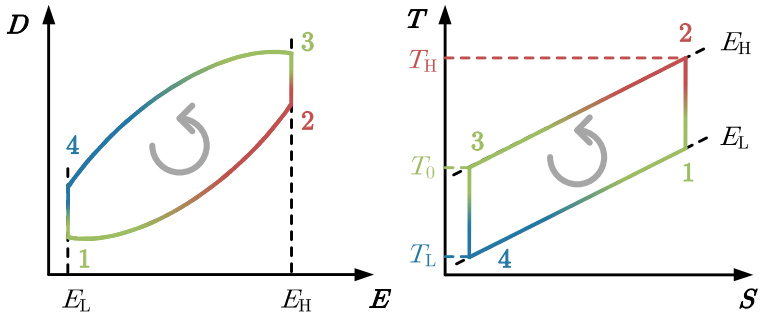

	1 to 2	2 to 3	3 to 4	4 to 1
Electric field E	↑	-	↓	-
Electric displacement D	↑	↑	↓	↓
Entropy S	-	↓	-	↑
Temperature T	↑	↓	↓	↑

Figure 5.6: The behavior of the reversed pyroelectric material in the Brayton cycle.

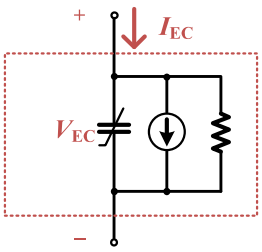

Figure 5.7: Proposed equivalent circuit model of the material in the reversed pyroelectric Brayton cycle.

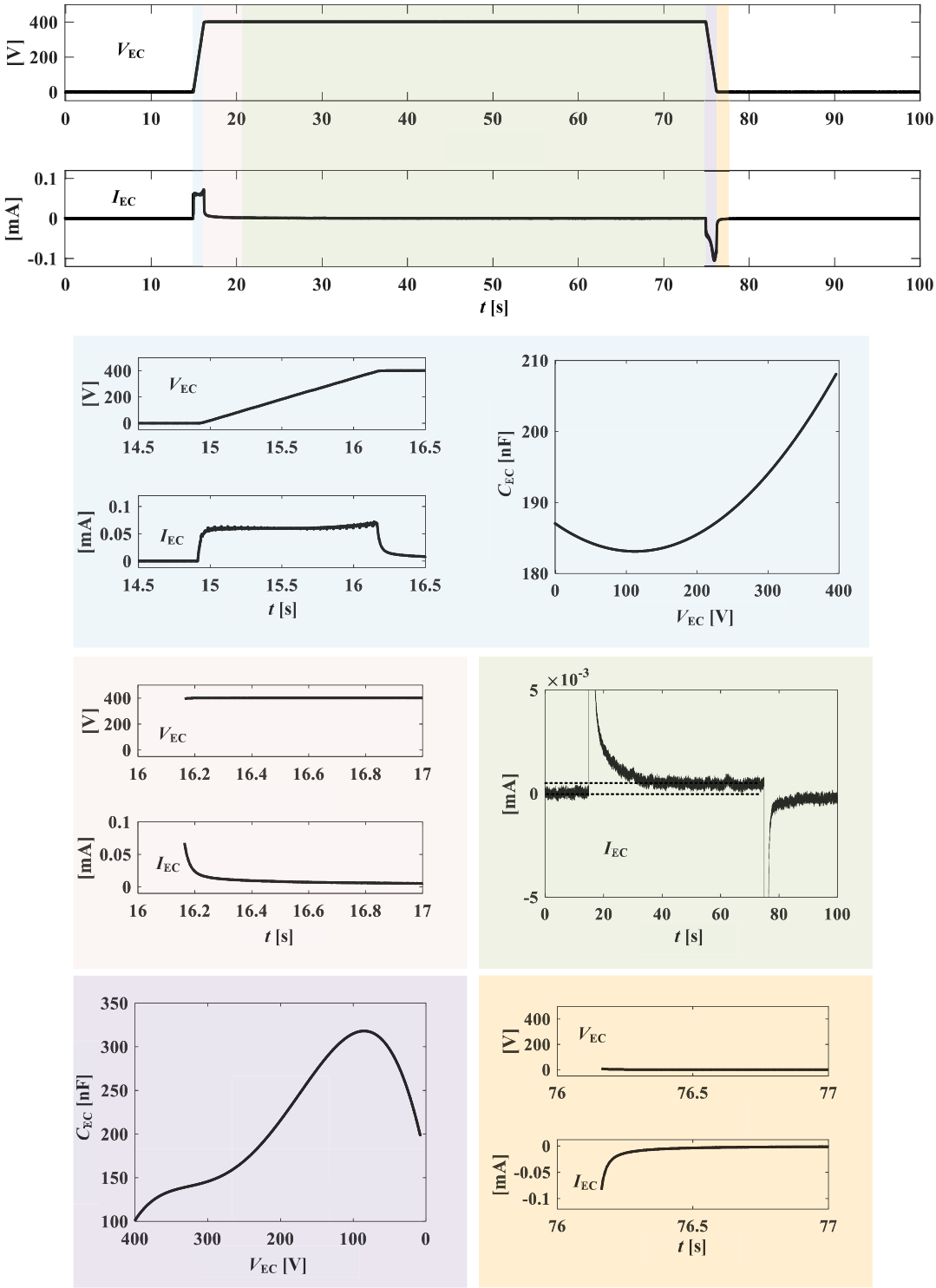

Figure 5.8: Measured voltage and current of the sample film in one Brayton cycle.

cording to the measured current in this period, which is approximately 0.6 µA, the equivalent leakage resistance can be calculated as

$$R_{\text{leakage}} = \frac{V_{\text{total}}}{I_{\text{leakage}}} - R_{\text{sense}} = 600\,\text{M}\Omega. \tag{5.17}$$

From status 3 to status 4, the capacitance can be calculated using (5.16). The calculation result is shown in the purple box in Fig. 5.8. It can be found that the pyroelectric material under test shows asymmetric characteristic during polarization and depolarization by comparing the capacitance in blue box and that in purple box.

After the heat transfer from status 4 back to status 1, whose zoomed-in waveforms are shown in the yellow box in Fig. 5.8, there is no leakage current as shown in the green box since the applied voltage is zero.

5.3 Design of the Power Converter for the Thermodynamic System

Based on the above electrical characterization of the pyroelectric material, the power converter for the reversed pyroelectric effect based thermodynamic system needs to be capable of performing the following functions:

- Initialization: providing the initial charge for one of the pyroelectric modules.
- Providing desired power to hold the maximum voltage during heat transfer.
- Charge recycling: transferring the charge of the discharging pyroelectric module to the one needs to be charged.
- Compensating the loss during charge recycling.

5.3.1 Design and Operation of the Power Stage

The proposed power stage is presented in Fig. 5.9. MOSFETs M_1 and M_2 and inductor L_1 are connected as a bidirectional buck-boost converter. L_1 is employed as the medium to transfer charge between pyroelectric module 1 C_{EC1} and pyroelectric

module 2 C_{EC2}. MOSFETs M_3 and M_4 and inductor L_2 are connected as a boost converter to provide the initial charge as well as to compensate the loss during operation for the system. MOSFETs M_5 and resistor $R_{\mathrm{precharge}}$ are used to limit the inrush current of the boost converter. A dc source is used in this work to represent the filtered AC voltage, whose equivalent value is from 120 V to 373 V for universal 50 kHz or 60 kHz ac voltage ranges from 85 V to 264 V.

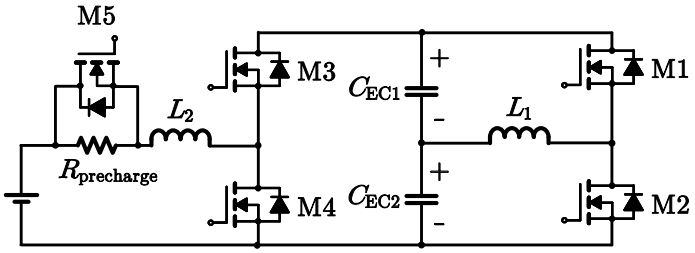

Figure 5.9: Power stage of proposed power converter for the thermodynamic system.

The operation of the converter can be divided into the following steps.

1. Initial charge

   There are two periods in the initial charge step. In the first period, M_4 and M_5 are turned off while M_3 is turned on. The power source charges the pyroelectric module through $R_{\mathrm{precharge}}$, L_2 and M_3. Since the two pyroelectric modules are operated out of phase, which means only one of them should be charged during this step, M_1 and M_2 are switching so that the charge in C_{EC1}, for example, is transferred to C_{EC2} to make sure only C_{EC2} is charged up while the voltage across C_{EC1} is maintained near zero. To transfer charge from C_{EC1} to C_{EC2}, M_1 is turned on when the voltage across C_{EC1} V_{EC1} is larger than zero, so that L_1 is charged up as shown in Fig. 5.10a. Once the current of L_1 I_{L1} reaches the desired maximum value, 10 A for example, or V_{EC1} is less than zero, M_1 is turned off and M_2 is turned on after a deadtime so that the energy stored in L_1 is transferred into C_{EC2}. Once I_{L1} decreases to zero, one period of charge transfer ends and the next period will start once V_{EC1} is larger than zero again.

   Once the sum of the voltages of the pyroelectric modules $V_{\mathrm{EC1}} + V_{\mathrm{EC2}}$ reaches the voltage of the power source, the system enters the second period of the

initial charge step. M_5 is turned on and $R_{\text{precharge}}$ is bypassed to reduce the unnecessary conduction loss. During this period, the power source continues to provide initial charge to the pyroelectric module through the boost converter consisted by M_3, M_4, and L_2. For each period, M_4 is turned on and M_3 is turned off first so that the current of L_2 I_{L2} is charged up to a desired value. After that, M_4 is turned off and M_3 is turned on so that the energy stored in L_2 is released to the pyroelectric module. Once I_{L2} decreases back to zero, M_3 is turned off and M_4 is turned on again to start the next period. During this period, M_1, M_2, and L_1 are operated in the same way as that in the first period to make sure only one of the pyroelectric modules is charged up. The operation of the power stage during this period is shown in as shown in Fig. 5.10b.

This step ends when the voltage across one of the pyroelectric modules reaches desired value, 1 kV for example for this work. The simulated voltage waveforms of V_{EC1} and V_{EC2} and the current waveforms of I_{L1} and I_{L2} are shown in Fig. 5.11.

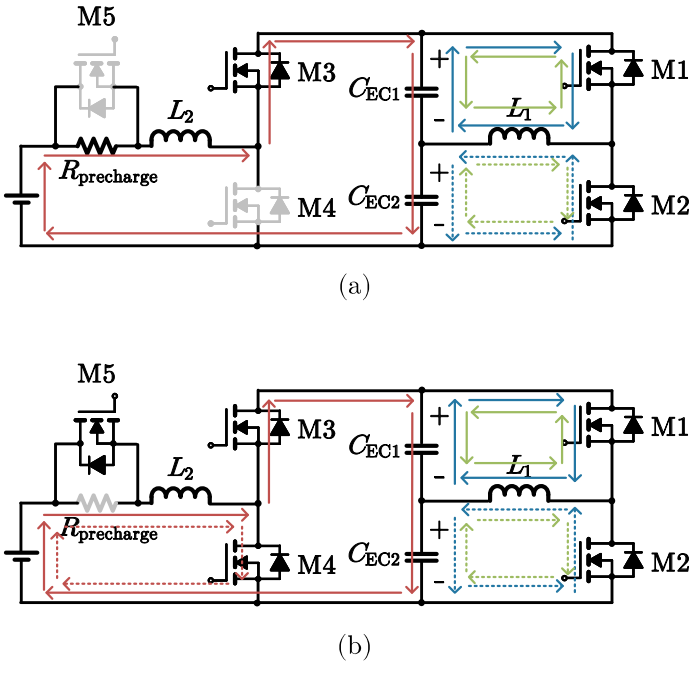

Figure 5.10: Operation of the power stage.

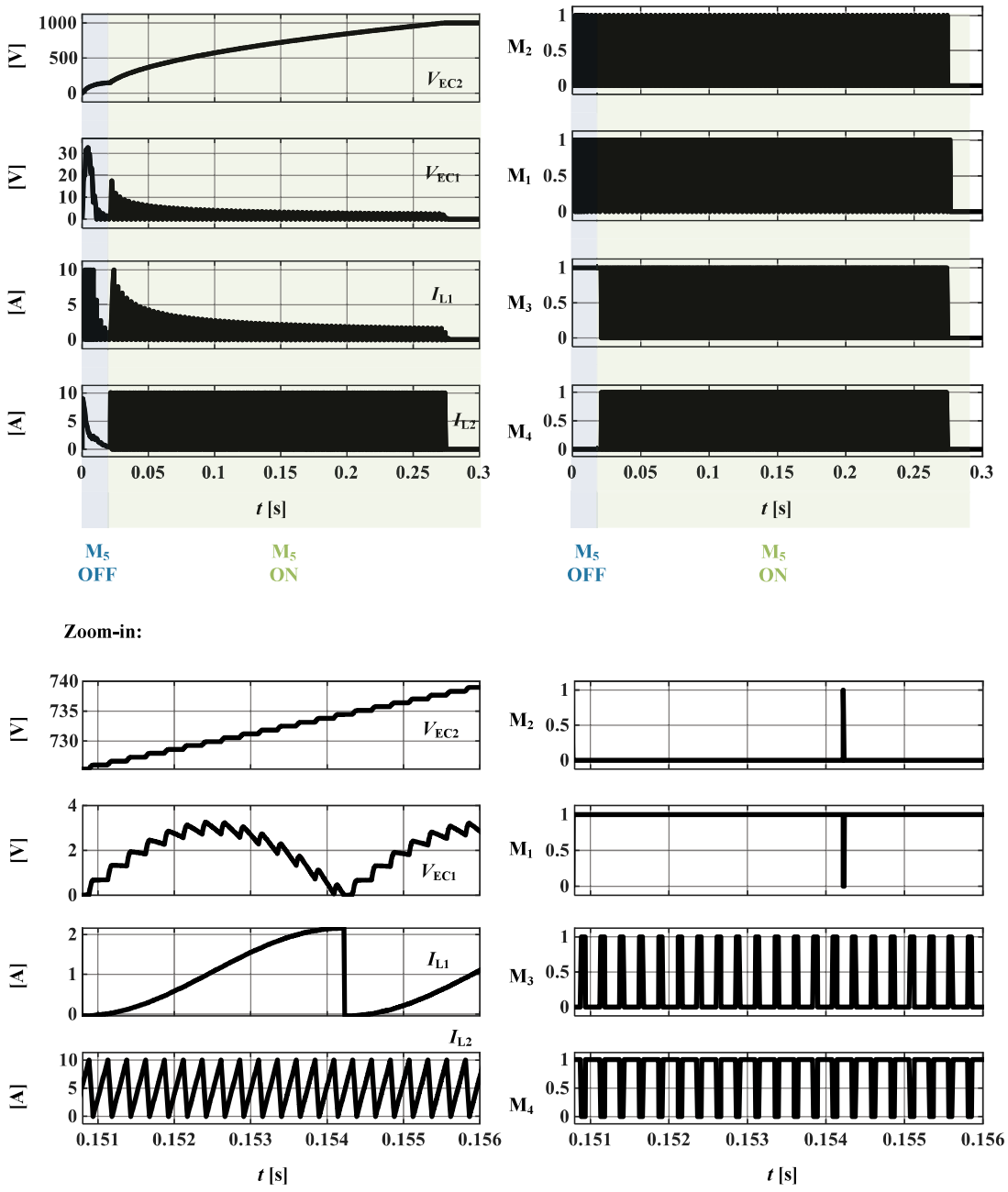

Figure 5.11: Simulated waveforms during initial charge step.

2. Heat transfer

   Once one of the pyroelectric modules is charged up (take C_{EC2} as an example), it enters the heat transfer step, which corresponds to the period from status 2 to status 3 for one of the pyroelectric modules (C_{EC2}) and from status 4 to status 1 for the other one (C_{EC1}) in Fig. 5.6. According to section 5.2, during this step, C_{EC2} needs to be injected more charge to maintain the voltage at the maximum value while C_{EC1} needs to release the entropy change induced charge so that the voltage can be kept at the minimum value. This can be achieved by the following operation: the front-end boost converter is operated to provide the charge needed by C_{EC2}; same as what happens during the initial charge step, once V_{EC1} is larger than zero, charge in C_{EC1} will be transferred to C_{EC2} by switching M_1 and M_2. This is the same operation for the second period in initial charge step, which is presented in Fig. 5.10b.

   Fig. 5.12 shows the example waveforms during this step. C_{EC2} is compensated to 1 kV whenever it is below 950 V for example due to heat transfer. And V_{EC1} is limited to several volts.

3. Charge transfer

   When the heat transfer step is completed, one of the pyroelectric modules needs to be discharged (take C_{EC2} as an example) while the other one (C_{EC1}) needs to be charged. The charge stored in C_{EC2} can be transferred to C_{EC1} to increase the system efficiency. In addition, the loss consumed by the system during charge transfer step needs to be compensate so that when this step is finished, C_{EC1} can be charged up to the desired value. During this step, the operation principle of the power stage is same as Fig. 5.10b. That is, the front-end boost converter is operated to compensate the loss of this step; charge in C_{EC2} is transferred to C_{EC1} by switching M_1 and M_2. For a high efficiency system, L_2 can be charged and discharged at a rate much slower than that for L_1. Or, for the same switching frequency, L_2 can be charged to a peak valued much less than that of L_1.

   Fig. 5.13 shows the example waveforms during this step. C_{EC2} is discharged

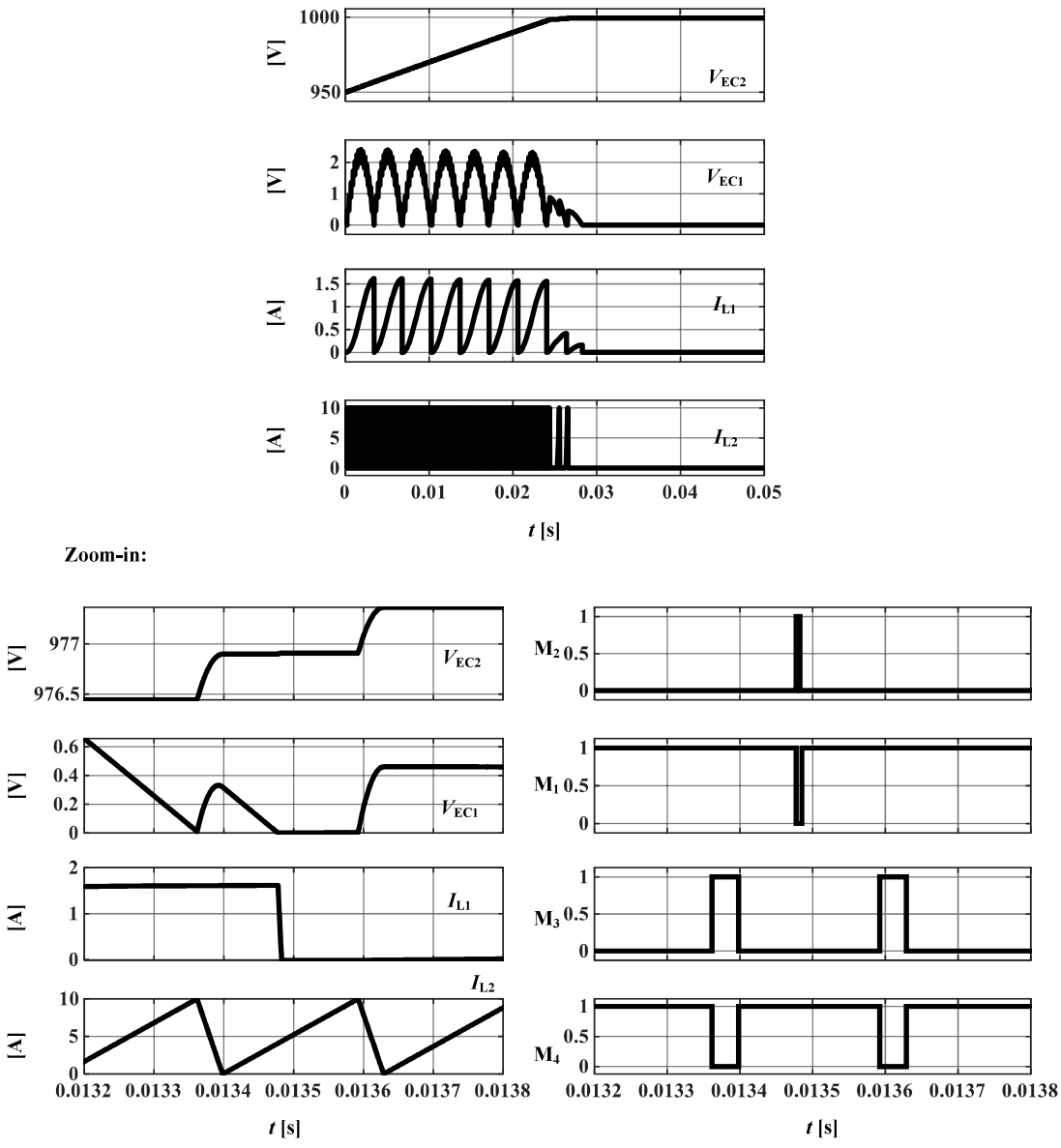

Figure 5.12: Simulated waveforms during heat transfer step.

from 950 V to 0 (50 V is used to represent the loss during charge transfer) while C_{EC1} is charged up from 0 to 1 kV. The switching loss as well as the conduction loss is compensated by the power source through the front-end boost converter. Fig. 5.13 is the example where the peak current value of L_2 is set to be the same as that of L_1 but L_2 is charged/discharged under discontinuous conduction mode while L_2 is charged/discharged under boundary conduction mode.

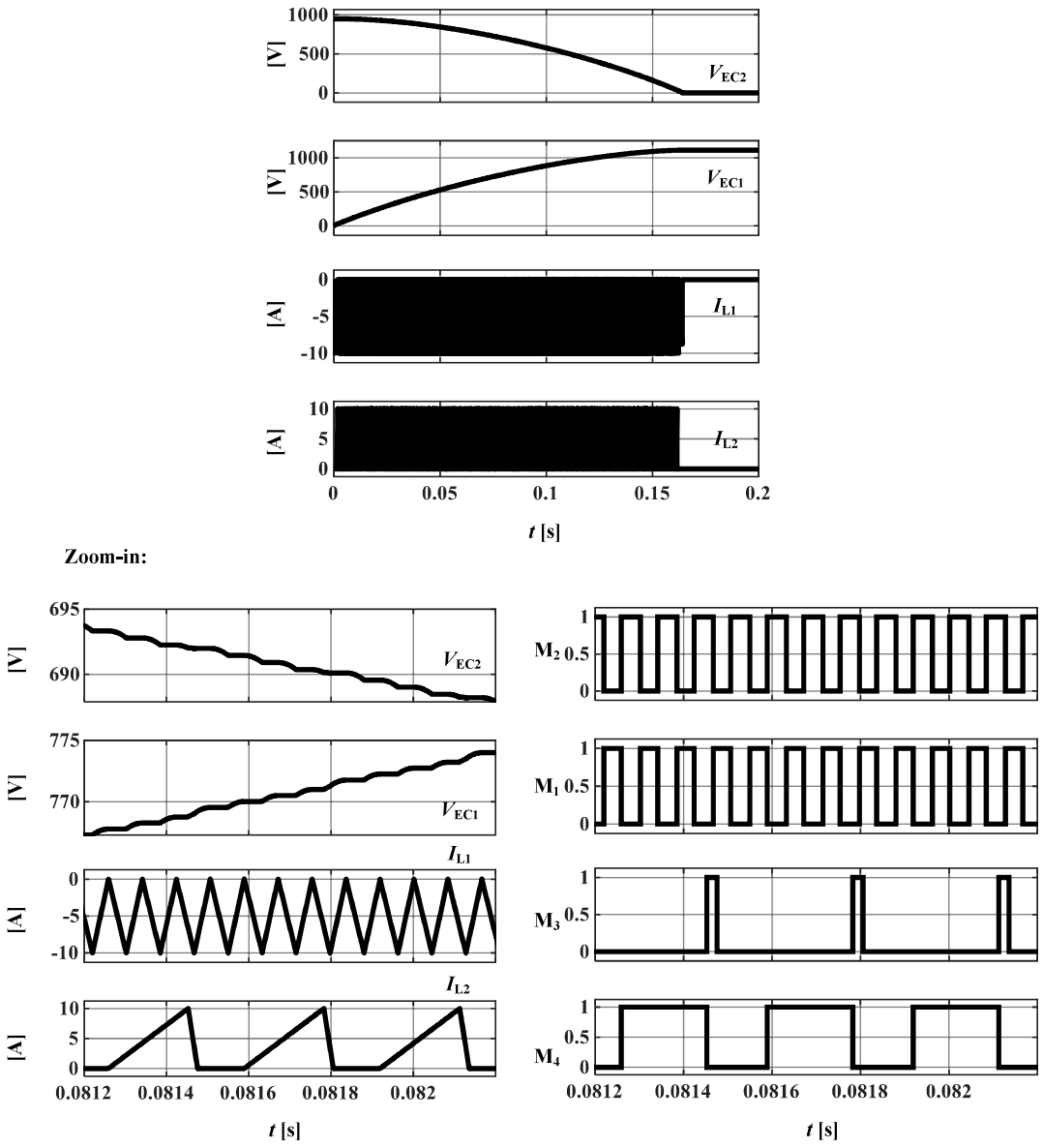

Figure 5.13: Simulated waveforms during charge transfer step.

According to the operation principle stated above, M_3 is always turned on at

zero drain-source voltage and turned off at zero current, M_4 is always turned on at zero current. For charge transfer from C_{EC1} to C_{EC2}, M_2 is always turned on at zero drain-source voltage and turned off at zero current, M_1 is always turned on at zero current. For charge transfer from C_{EC2} to C_{EC1}, M_1 is always turned on at zero drain-source voltage and turned off at zero current, M_2 is always turned on at zero current. Therefore, a low switching loss can be expected.

5.3.2 Design of the Control

Based on the operation of the power stage stated above, a digital-and-analog hybrid control is employed. MCU is employed to decide which step the system is in. Hysteresis control is employed for switches in both front-end boost converter and the charge recycle bidirectional buck-boost converter. In general, an analog hysteresis control has shorter propagation delay (in nanosecond range) than a digital one (in microsecond range) and the propagation delay decides the error between the practical peak current value and the desired one ΔI_L, which can be calculated as

$$\Delta I_L = \frac{V_L}{L} \cdot t_{pd}, \tag{5.18}$$

where t_{pd} is the propagation delay of the control path. Therefore, the analog hysteresis control is employed to achieve smaller inductance for same current error.

Fig. 5.14 shows the overall control scheme and Fig. 5.15 shows the detailed circuit of the analog hysteresis control path. V_{EC1} to V_{EC2} are sensed by resistive voltage divider and the sensed voltage are used by MCU to determine the system status, whether in initial charge, heat transfer, or charge transfer stage. I_{L1} and I_{L2} are sensed by hall effect based current sensors. After level-shifting and amplification, the post-conditioned current signals are fed into the hysteresis comparator. The gate signals are generated after a deadtime generation circuit to ensure safe operation of the phase legs. A multiplexer (MUX) is employed to select the gate signals generated by the analog hysteresis control path and those generated by the MCU, which are used to start up the system.

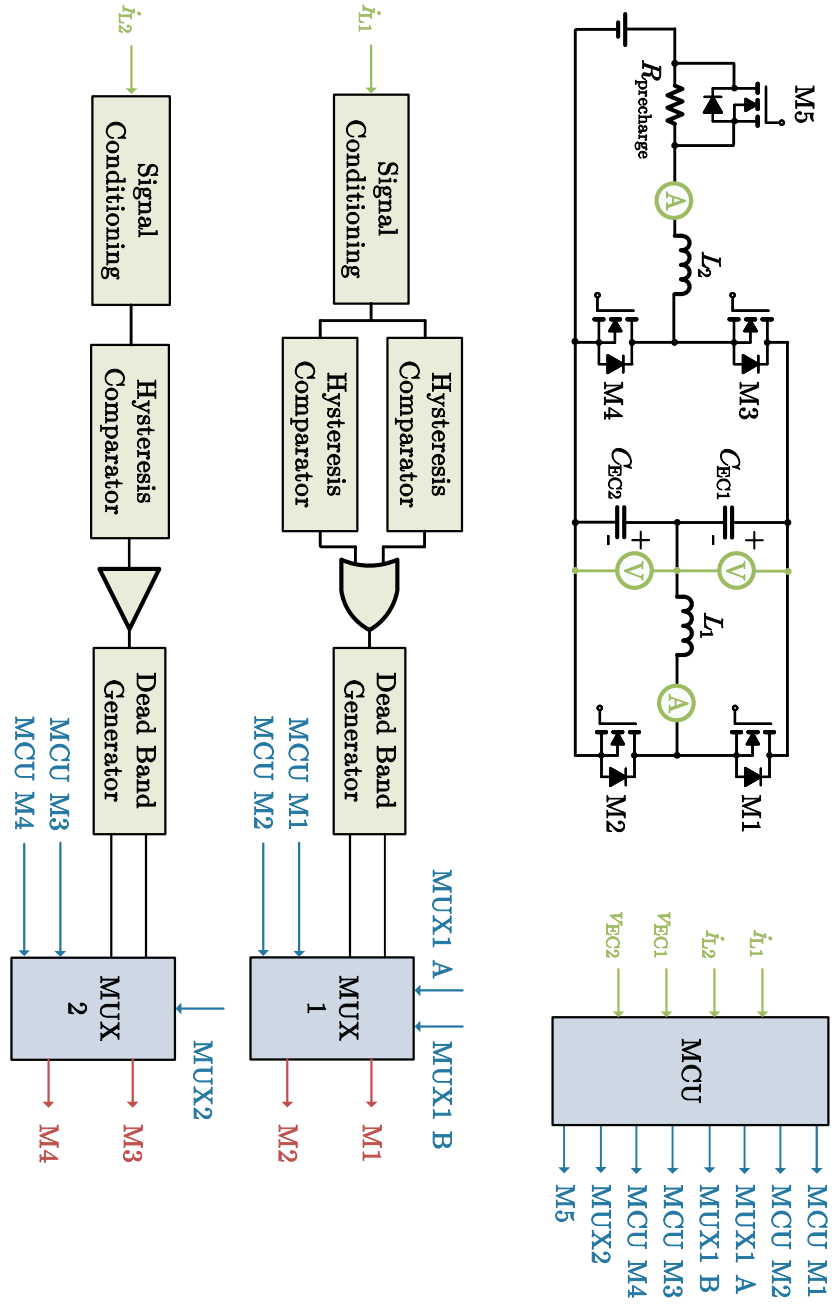

Figure 5.14: Control scheme of the proposed converter.

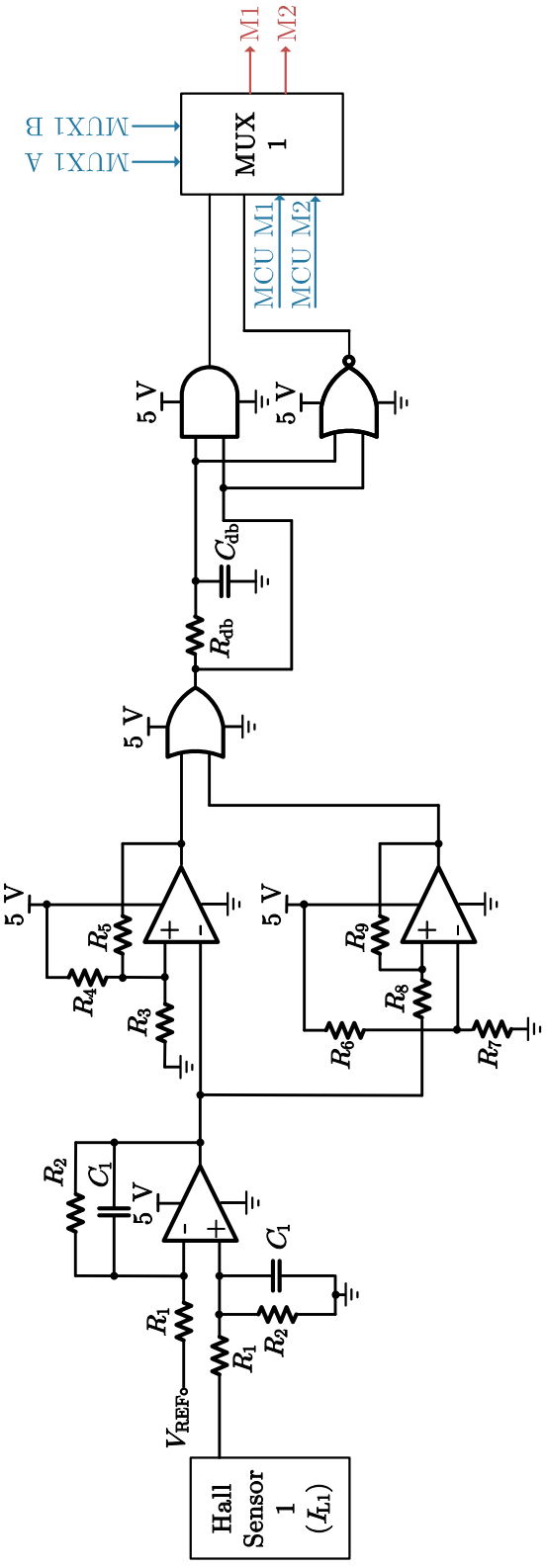

Figure 5.15: Circuit of analog control path.

5.4 Experimental Results

A prototype shown in Fig. 5.16 is built to verified the proposed converter and its control. The power stage and the analog control path are loacted on the horizontal board and the vertical board is the digital control board. Capacitor banks and inductors are connected off-the-board. The size of the active region of the power stage is 7.3 cm × 16.5 cm.

Fig. 5.17 shows the voltage waveforms of the pyroelectric modules and current waveforms of the inductors. V_{EC1} and V_{EC2} are voltages of pyroelectric modules C_{EC1} and C_{EC2} respectively. I_{L1} and I_{L2} are currents of inductors L_1 in charge-recycling buck-boost converter and L_2 in front-end boost converter respectively. Fig. 5.17a is illustrative operational waveform. Fig. 5.17b and Fig. 5.17c are zoomed waveforms during initial charge and charge transfer periods respectively. Fig. 5.17d shows the desired waveforms for practical reversed pyroelectric effect based system. The proposed operation can be verified:

1. The pyroelectric module C_{EC2} is precharged to the voltage of the power source first and is then charged to 1 kV. During this stage, M_1 and M_2 are switched to transfer any charge in C_{EC1} to C_{EC2} so that only C_{EC2} is charged up during this stage. This stage take several hundred of miliseconds, which can be treated as a adiabatic process. This time length can be adjusted by tuning the peak current value of I_{L1} and I_{L2}. Higher peak current value leads to shorter charge time.

2. V_{EC2} is hold at 1 kV for tens of seconds to wait for the heat transfer between the pyroelectric module and the regenerator. Power source provides the power needed in this stage to C_{EC2} through the front-end boost converter. M_1 and M_2 are switched to transfer any charge in C_{EC1} to C_{EC2} to keep V_{EC1} at zero volt. The time length is programmable via the MCU.

3. V_{EC2} is discharged from 1 kV to 0 and the charge is transferred to C_{EC1}. The front-end boost converter is operated at discontinuous conduction mode to

compensate the loss during this stage so that at the end of this stage V_{EC1} is charged from 0 to 1 kV.

4. V_{EC1} is hold at 1 kV for tens of seconds to wait for the heat transfer between the pyroelectric module and the regenerator. Power source provides the power needed in this stage to C_{EC1} through the front-end boost converter. M_1 and M_2 are switched to transfer any charge in C_{EC2} to C_{EC1} to keep V_{EC2} at zero volt. The time length is programmable via the MCU.

5. V_{EC1} is discharged from 1 kV to 0 and the charge is transferred to C_{EC2}. The front-end boost converter is operated at discontinuous conduction mode to compensate the loss during this stage so that at the end of this stage V_{EC2} is charged from 0 to 1 kV.

6. The converter will enter step 2 and repeat from step 2 to step 5 as needed.

Fig. 5.18 shows the thermal picture for the converter operated under steady state without forced cooling. Since after each charge transfer period, the converter enters idle mode for several tens of seconds, the heat dissipation is not an issue. The maximum temperature spot is 40.5 °C, locating at the gate driving ICs.

The measured efficiency for the charge-recycling bidirectional buck-boost converter charging/discharging 310 µF capacitor banks within 0.13 s, whose equivalent average power equals 1.2 kW, is 98%. The loss breakdown is presented in Fig. 5.19.

5.5 Conclusion

Reversed pyroelectric effect based thermodynamic system provides an environmentally friendly solution compared to traditional vapor-compression technology since it does not require the use of green-house gas. To build the power converter for the thermodynamic system, a electrical behavior circuit model is firstly proposed based on the electrical characterization of the material. Based the electrical characteristic of the material, a power converter featuring system initializing, energy

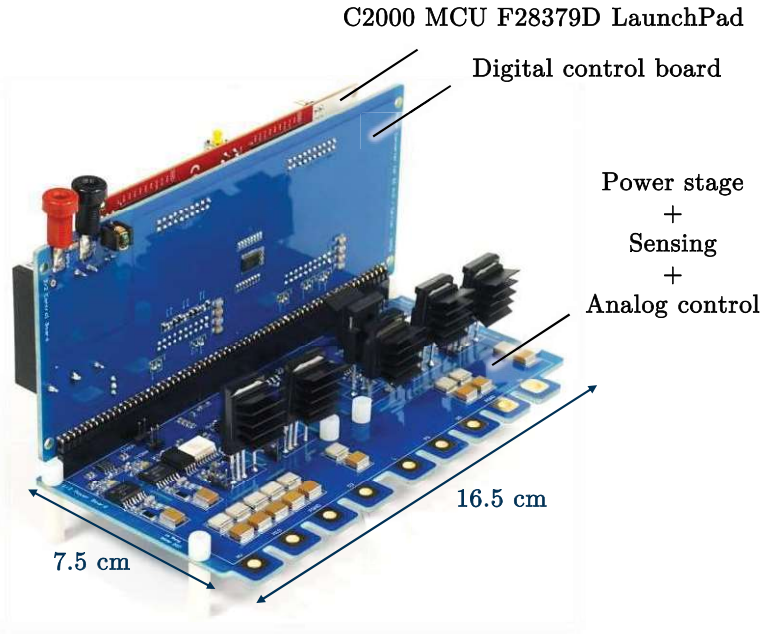

(a)

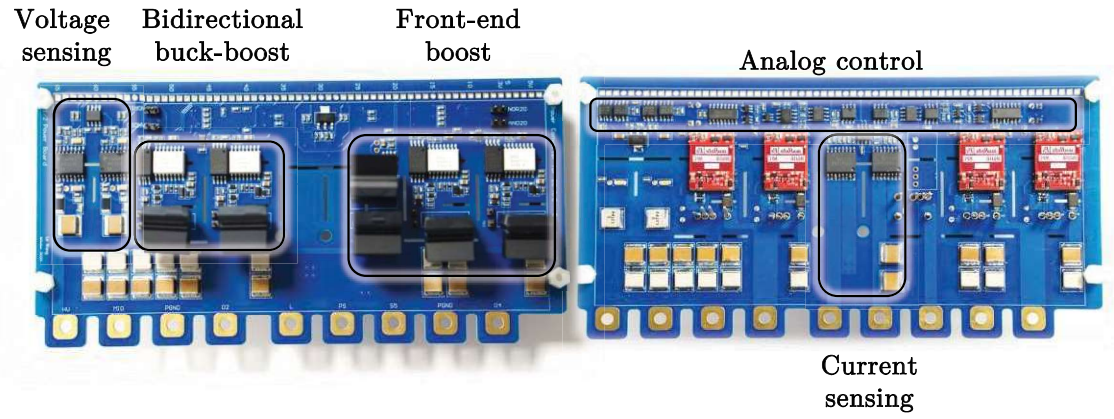

(b)

Figure 5.16: Prototype of the proposed power converter: (a) overall converter and (b) lateral board (left: front side; right: back side).

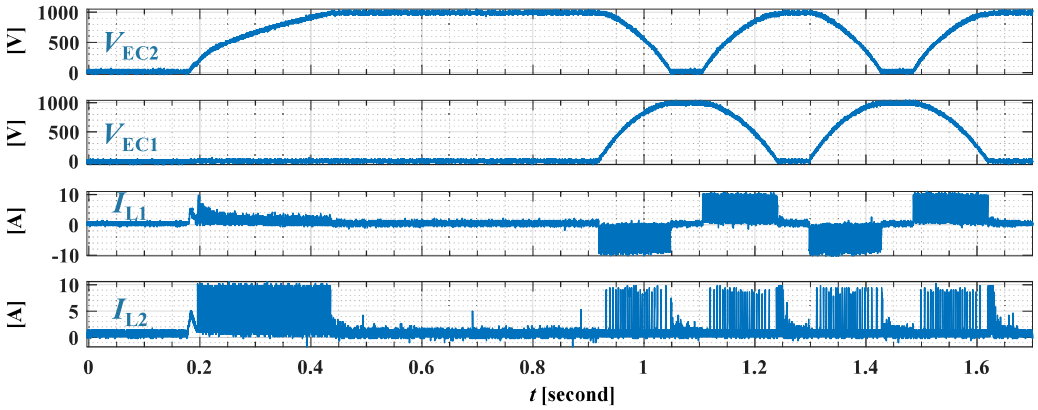

(a)

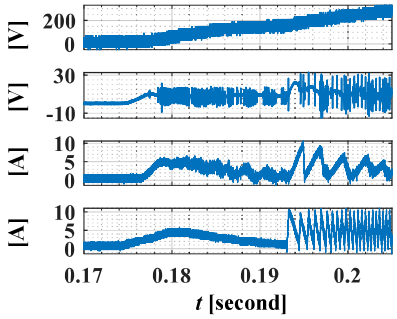

(b)

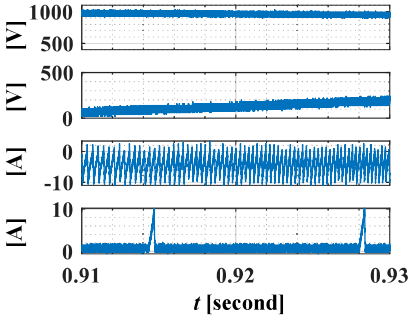

(c)

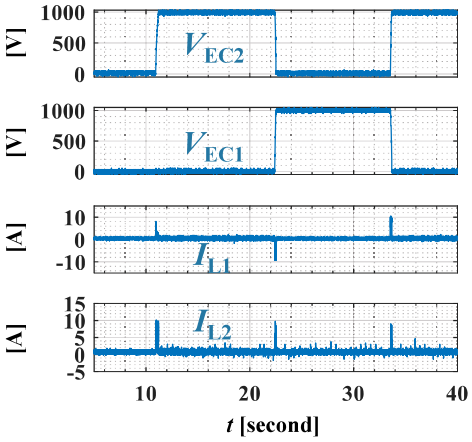

(d)

Figure 5.17: Experimental waveforms.

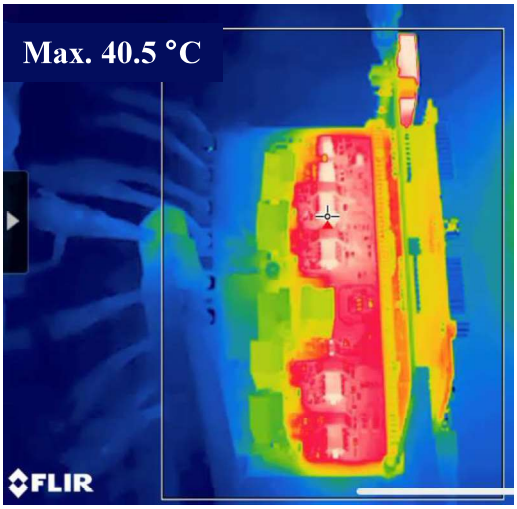

Figure 5.18: Thermal picture under steady state wich charge-recycling power at 1.2 kW.

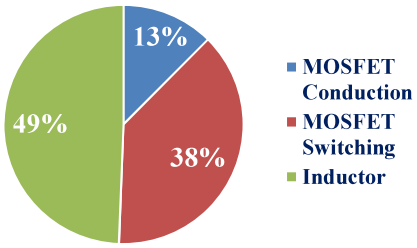

Figure 5.19: Loss breakdown of charge-recycling buck-boost at 1.2 kW.

recovering, and loss compensation functions is proposed, which is composed by a front-end boost converter and a bidirectional buck-boost converter. Analog-digital hybrid control is adopted to minimize the required inductance. The proposed converter is verified by a prototype which can provide 1 kV driving voltage and 1.2 kW charge-recycling power for the pyroelectric modules.

Chapter 6

Conclusions and Outlook

6.1 Conclusion

This work studied the electromechanical and electrothermal energy inter-conversions and proposed the design of power converters for piezoelectric and reversed pyroelectric materials.

To provide a guide for the design of PT-based converters, the electrical characteristics of PTs are first analyzed. This work reviewed and compared different models of PT. Closed-form expressions of characteristic points are given in this paper, which include mechanical resonant, series resonant, parallel resonant, unity-gain, peak-gain, maximum input impedance, minimum input impedance, maximum input impedance phase, and maximum efficiency points. They have different expressions even their locations may be close to each other and may merge together in some special cases.

Impedance matching is one of the methods that can be used to improve the efficiency of the PT. The effectiveness of this method depends on the type of the PT and/or the configuration of the PT. When designing a PT-based converter, extra compensation components can be used to modify the characteristic and/or improve the performance of the PT. The compensation network could be a series input inductor, a parallel input inductor, a series output inductor, a parallel output inductor or combination among these components. And for some types of PTs, extra input or output capacitor may be needed. This work provides a comprehensive analysis of the impacts of these compensation components on the characteristics

of a PT. Ideal input inductors and capacitor do not affect the efficiency of a PT. Input inductors modify the input impedance. The input parallel inductor does not change the gain but the series one changes the peak gain frequency and magnitude. When series input inductor is used, the input capacitor will affect the gain. Both output series and parallel inductors can be used to improve the PT efficiency but lead to different optimal load range. Output series inductor does not change the voltage gain much but the parallel one does. When the output series resonant inductor is applied, an external output capacitor can help reduce the size of the output inductor but decreases the efficiency. This will not happen if an ideal output parallel resonant inductor is applied. In addition, when both input and output series resonant inductors are used, an approximate constant voltage gain characteristic can be achieved. The non-idealities have also been analyzed.

This work also illustrates the working principle of the tunable PT and gives a design method of tunable PT based dc-dc converters. The gain characteristic of tunable PT changes with the impedance connected at the auxiliary control port of the tunable PT. A PWM controlled switched capacitor is connected at the control port. For different load or input conditions, this switched capacitor presents proper capacitance at the control port to regulate the output without changing the operation frequency. The fixed frequency operation allows the tunable PT to be operated near its optimum switching frequency, and renders the highest efficiency. A closed-loop control scheme for output voltage regulation is presented. Tunable PT samples whose power levels range from 30 W to 100 W are tested with the proposed dc-dc converter prototype to validate the design.

In addition, the benefits of the input inductor and the ac output inductor in a tunable PT based dc-dc converter are analyzed. The input inductor helps the input half bridge to achieve ZVS and compensates that circulating current of the input capacitor of the tunable PT. It also works together with the ac output inductor to form a LC-Series-CL tank to provide better regulation ability for the converter. Meanwhile, smaller external control capacitor is required. The ac output inductor also works as the output impedance matching network to compensate the circulating current of the output capacitor of the tunable PT, which improves the efficiency of

the converter. The analysis is verified by the experiment.

Rosen-type PT features natural mechanisms for high transform ratio in a compact planar form, which provide an alternative solution for dc bus-fed high step-down voltage-ratio auxiliary power supplies in medium-/high-voltage systems, i.e., power electronics building blocks and renewable energy applications, without using bulky magnetic transformer with high turns numbers. The design procedure of the Rosen-type PT-based high step-down voltage-ratio dc-dc converter is presented. To verify the design, a 5 W, 1 kV to 5 V prototype is built and tested.

The cross-coupling between thermal property and electrical property is called pyroelectric effect. The pyroelectric effect refers to the polarization change caused by temperature change, while the reversed pyroelectric effect is the reversed process, i.e., a temperature change will be generated when there is a electric field change. The reversed pyroelectric effect can be used for solid-state heating/cooling in a environmentally friendly manner. Electrical characterization is executed to facilitate the design of the reversed pyroelectric effect based thermodynamic system. In this system, the power converter needs to provide the desired electric field for the pyroelectric modules. In addition, charge recycling is needed to improve the system efficiency. The proposed design is verified by a prototype which can provide 1 kV driving voltage and 1.2 kW charge-recycling power for pyroelectric modules.

6.2 Potential Future Work

There is always more to explore. The following lists several potential future research topics related to this dissertation:

- Design of magnetics-free PT-based converter.

  For radial type tunable PT, parameters of the PT as well as the circuit can be optimized so that the input inductor can be eliminated for ZVS purpose. Trade-off between elimination of the output filter inductor and the performance of the converter can be further discussed.

  For rosen-type PT, isolation layer can be added to the PT so that the magnetic

transformer can be eliminated. Similarly, trade-off between elimination of the output compensation inductor and the performance of the converter can be further discussed.

- Modular design of rosen-type PT-based high step-down voltage-ratio converter

  The proposed converter can be further explored and connected into input-series-output-parallel/series structure so that input voltage and the power level can be expanded.

- Quantitative equivalent circuit model of the material in reversed pyroelectric process will be helpful for further system optimization.

- In the proposed power converter for the reversed pyroelectric effect based thermodynamic system, the currents of the inductors have high peak value while low overall average value. Therefore, an optimized inductor design with high saturating current and low rated dc current will improve the power density of the system.

Bibliography

[1] D.-S. Park, M. Hadad, L. Rimer, R. Ignatans, D. Spirito, V. Esposito, V. Tileli, N. Gauquelin, D. Chezganov, D. J. J. Verbeeck *et al.*, "Induced giant piezoelectricity in centrosymmetric oxides," *arXiv preprint arXiv:2111.00829*, 2021.

[2] M. Lethiecq, F. Levassort, D. Certon, and L. P. Tran-Huu-Hue, "Piezoelectric and acoustic materials for transducer applications," *Chapter3*, vol. 10, pp. 39–58, 2008.

[3] R. K. Pandey, *Fundamentals of Electroceramics: Materials, Devices, and Applications*. John Wiley & Sons, 2019.

[4] W. R. Cook, H. Jaffe, and B. Jaffe, *Piezoelectric ceramics*, 1971.

[5] L. APC International, *Piezoelectric Ceramics: Principles and Applications*. APC International, 2011. [Online]. Available: https://books.google.com/books?id=nUafpwAACAAJ

[6] C. Zhou, J. Zhang, W. Su, and Y. Cao, "Large thickness-mode electromechanical coupling and good temperature stability of 1–3 pzt/epoxy composites," *Journal of Materials Science: Materials in Electronics*, vol. 32, no. 4, pp. 4705–4712, 2021.

[7] C.-y. Lin, *Design and analysis of piezoelectric transformer converters*. Virginia Polytechnic Institute and State University, 1997.

[8] W. P. Mason, *Electromechanical transducers and wave filters*. D. Van Nostrand Company, 1948.

[9] H. Katz, *Solid state magnetic and dielectric devices*. John Wiley & Sons, 1959.

[10] D. A. Berlincourt, D. R. Curran, H. Jaffe *et al.*, "Piezoelectric and piezomagnetic materials and their function in transducers," *Physical Acoustics: Principles and Methods*, vol. 1, no. Part A, pp. 202–204, 1964.

[11] A. Arjun, A. Sampath, S. Thiyagarajan, and V. Arvind, "A novel approach to recycle energy using piezoelectric crystals," *International Journal of Environmental Science and Development*, vol. 2, no. 6, p. 488, 2011.

[12] R. Bhavsar, N. Y. Vaidya, P. Ganguly, A. Humphreys, A. Robisson, H. Tu, N. Wicks, G. H. McKinley, and F. Pauchet, "Intelligence in novel materials," *Oilfield review*, vol. 20, no. 1, pp. 32–41, 2008.

[13] A. Erturk and D. J. Inman, *Piezoelectric energy harvesting*. John Wiley & Sons, 2011.

[14] G. Gautschi, "Piezoelectric sensors," in *Piezoelectric Sensorics*. Springer, 2002, pp. 73–91.

[15] K. Spanner and B. Koc, "Piezoelectric motors, an overview," in *Actuators*, vol. 5, no. 1. Multidisciplinary Digital Publishing Institute, 2016, p. 6.

[16] A. Abdullah, M. Shahini, and A. Pak, "An approach to design a high power piezoelectric ultrasonic transducer," *Journal of Electroceramics*, vol. 22, no. 4, pp. 369–382, 2009.

[17] E. M. Baker, W. Huang, D. Y. Chen, and F. C. Lee, "Radial mode piezoelectric transformer design for fluorescent lamp ballast applications," *IEEE Transactions on Power Electronics*, vol. 20, no. 5, pp. 1213–1220, 2005.

[18] M. S. Rødgaard, M. Weirich, and M. A. Andersen, "Forward conduction mode controlled piezoelectric transformer-based pfc led drive," *IEEE transactions on power electronics*, vol. 28, no. 10, pp. 4841–4849, 2012.

[19] M. Day and B. S. Lee, "Understanding piezoelectric transformers in ccfl backlight applications," *Analog Applications Journal, Texas Instruments Incorporated*, pp. 18–23, 2002.

[20] T. Kim, S. Choi, S. Lee, and B. Cho, "New piezoelectric transformer adapter with universal input voltage range," in *2005 International Conference on Power Electronics and Drives Systems*, vol. 2. IEEE, 2005, pp. 1223–1227.

[21] Z. Kutnjak, B. Rožič, and R. Pirc, "Electrocaloric effect: theory, measurements, and applications," *Wiley encyclopedia of electrical and electronics engineering*, pp. 1–19, 1999.

[22] S.-G. Lu, Q. Zhang, and Z. Kutnjak, "The electrocaloric effect (ece) in ferroelectric polymer films," in *Thin Film Growth*. Elsevier, 2011, pp. 364–383.

[23] J. Shi, D. Han, Z. Li, L. Yang, S.-G. Lu, Z. Zhong, J. Chen, Q. Zhang, and X. Qian, "Electrocaloric cooling materials and devices for zero-global-warming-potential, high-efficiency refrigeration," *Joule*, vol. 3, no. 5, pp. 1200–1225, 2019.

[24] G. Suchaneck, O. Pakhomov, and G. Gerlach, *Electrocaloric cooling.* InTechOpen London, 2017.

[25] E. Defay, R. Faye, G. Despesse, H. Strozyk, D. Sette, S. Crossley, X. Moya, and N. Mathur, "Enhanced electrocaloric efficiency via energy recovery," *Nature communications*, vol. 9, no. 1, pp. 1–9, 2018.

[26] A. M. Nicolson, "Piezo-electric crystal transformer," U.S. Patent 1 829 234, 1931.

[27] C. Rosen, K. Fish, and H. Rothenberg, "Electromechanical transducer," U.S. Patent 2 830 274, 1958.

[28] C. Rosen, "Ceramic transformers and filters', 1956," in *Proc. Electronic Comp. Symp., pp205-211.*

[29] C. A. Rosen, *Analysis and design of ceramic transformers and filter elements.* Syracuse University, 1956.

[30] Y.-H. Hsu, C.-K. Lee, and W.-H. Hsiao, "Electrical and mechanical fully coupled theory and experimental verification of rosen-type piezoelectric transformers," *IEEE transactions on ultrasonics, ferroelectrics, and frequency control*, vol. 52, no. 10, pp. 1829–1839, 2005.

[31] J. Yang, "Comment on y.-h. hsu et al.," electrical and mechanical fully coupled theory and experimental verification of rosen-type piezoelectric transformers"," *IEEE transactions on ultrasonics, ferroelectrics, and frequency control*, vol. 54, no. 4, pp. 699–700, 2007.

[32] J. Yang and X. Zhang, "Extensional vibration of a nonuniform piezoceramic rod and high voltage generation," *International Journal of Applied Electromagnetics and Mechanics*, vol. 16, no. 1-2, pp. 29–42, 2002.

[33] C. Nadal and F. Pigache, "Multimodal electromechanical model of piezoelectric transformers by hamilton's principle," *IEEE transactions on ultrasonics, ferroelectrics, and frequency control*, vol. 56, no. 11, pp. 2530–2543, 2009.

[34] J. Yang, *Analysis of piezoelectric devices.* World Scientific, 2006.

[35] Y. Fuda, K. Kumasaka, M. Katsuno, H. Sato, and Y. Ino, "Piezoelectric transformer for cold cathode fluorescent lamp inverter," *Japanese journal of applied physics*, vol. 36, no. 5S, p. 3050, 1997.

[36] H. Kawai, Y. Sasaki, T. Inoue, T. Inoi, and S. Takahashi, "High power transformer employing piezoelectric ceramics," *Japanese journal of applied physics*, vol. 35, no. 9S, p. 5015, 1996.

[37] S.-T. Ho, "Design of the longitudinal mode piezoelectric transformer," in *2007 7th International Conference on Power Electronics and Drive Systems*. IEEE, 2007, pp. 1639–1644.

[38] Y. Sasaki, M. Yamamoto, A. Ochi, T. Inoue, and S. Takahashi, "Small multilayer piezoelectric transformers with high power density–characteristics of second and third-mode rosen-type transformers–," *Japanese journal of applied physics*, vol. 38, no. 9S, p. 5598, 1999.

[39] K. Kanayama and N. Maruko, "Properties of alternately poled piezoelectric transformers," *Japanese journal of applied physics*, vol. 36, no. 5S, p. 3048, 1997.

[40] L. Li, N. Zhang, C. Bai, X. Chu, and Z. Gui, "Multilayer piezoelectric ceramic transformer with low temperature sintering," *Journal of materials science*, vol. 41, no. 1, pp. 155–161, 2006.

[41] M. Shoyama, K. Horikoshi, T. Ninomiya, T. Zaitsu, and Y. Sasaki, "Steady-state characteristics of the push-pull piezoelectric inverter," *IEICE transactions on communications*, vol. 82, no. 8, pp. 1318–1325, 1999.

[42] K. Sakurai, K. Ohnishi, and Y. Tomikawa, "Presentation of a new equivalent circuit of a piezoelectric transformer under high-power operation," *Japanese journal of applied physics*, vol. 38, no. 9S, p. 5592, 1999.

[43] S. Dong, A. V. Carazo, and S. H. Park, "Equivalent circuit and optimum design of a multilayer laminated piezoelectric transformer," *IEEE transactions on ultrasonics, ferroelectrics, and frequency control*, vol. 58, no. 12, pp. 2504–2515, 2011.

[44] J. Hu, Y. Fuda, T. Yoshida *et al.*, "A study on the rectangular-bar-shaped multilayer piezoelectric transformer using length extensional vibration mode," *Japanese journal of applied physics*, vol. 38, no. 5S, p. 3208, 1999.

[45] T. Zaitsu, Y. Fuda, Y. Okabe, T. Ninomiya, S. Hamamura, and M. Katsuno, "New piezoelectric transformer converter for ac-adapter," in *Proceedings of APEC 97-Applied Power Electronics Conference*, vol. 2. IEEE, 1997, pp. 568–572.

[46] S. Hamamura, T. Zaitsu, T. Ninomiya, and M. Shoyama, "Noise characteristics of piezoelectric-transformer dc-dc converter," in *PESC 98 Record. 29th Annual IEEE Power Electronics Specialists Conference (Cat. No. 98CH36196)*, vol. 2. IEEE, 1998, pp. 1262–1267.

[47] T. Zaitsu, "Power conversion using piezoelectric transformer," Ph.D. dissertation, Ph. D. Dissertation, Kyushu University, Fukuoka, Japan, 1997.

[48] M. Guo, X. Jiang, K. H. Lam, S. Wang, C. Sun, H. L. Chan, and X. Zhao, "Lead-free multilayer piezoelectric transformer," *Review of scientific instruments*, vol. 78, no. 1, p. 016105, 2007.

[49] O. Stuetzer, "Linear theory of piezoelectric power transformers." Sandia Labs., Albuquerque, N. Mex., Tech. Rep., 1966.

[50] A. M. Sánchez, M. Sanz, R. Prieto, J. A. Oliver, P. Alou, and J. A. Cobos, "Design of piezoelectric transformers for power converters by means of analytical and numerical methods," *IEEE transactions on industrial electronics*, vol. 55, no. 1, pp. 79–88, 2008.

[51] J. Oliver, R. Prieto, M. Sanz, J. Cobos, and J. Uceda, "1d modeling of multi-layer piezoelectric transformers," in *2001 IEEE 32nd Annual Power Electronics Specialists Conference (IEEE Cat. No. 01CH37230)*, vol. 4. IEEE, 2001, pp. 2097–2102.

[52] O. Ohnishi, H. Kishie, A. Iwamoto, Y. Sasaki, T. Zaitsu, and T. Inoue, "Piezoelectric ceramic transformer operating in thickness extensional vibration mode for power supply," in *IEEE 1992 Ultrasonics Symposium Proceedings.* IEEE, 1992, pp. 483–488.

[53] J.-H. Kim, D.-Y. Han, M.-H. Nam, and S.-M. Kang, "Analysis of a three-layered piezoelectric ceramic transformer filter," *IEEE Transactions on Circuits and Systems I: Fundamental Theory and Applications*, vol. 42, no. 6, pp. 307–313, 1995.

[54] T. Bove, W. Wolny, E. Ringgaard, and K. Breboel, "New type of piezoelectric transformer with very high power density," in *ISAF 2000. Proceedings of the 2000 12th IEEE International Symposium on Applications of Ferroelectrics (IEEE Cat. No. 00CH37076)*, vol. 1. IEEE, 2000, pp. 321–324.

[55] R. Prieto, M. Sanz, J. Cobos, P. Alou, O. Garcia, and J. Uceda, "Design considerations of multi-layer piezoelectric transformers," in *APEC 2001. Sixteenth Annual IEEE Applied Power Electronics Conference and Exposition (Cat. No. 01CH37181)*, vol. 2. IEEE, 2001, pp. 1258–1263.

[56] A. Sanchez, M. Sanz, R. Prieto, J. Oliver, and J. Cobos, "Mixed analytical and numerical design method for piezoelectric transformers," in *IEEE 34th Annual Conference on Power Electronics Specialist, 2003. PESC'03.*, vol. 2. IEEE, 2003, pp. 841–846.

[57] Y. Sasaki, K. Uehara, and T. Inoue, "Piezoelectric ceramic transformer being driven with thickness extensional vibration," Aug. 31 1993, uS Patent 5,241,236.

[58] M. Sanz, A. Sanchez, J. Oliver, R. Prieto, J. Cobos, and J. Uceda, "Fea based model of multi-layer piezoelectric transformer working in thickness mode," in *2004 IEEE 35th Annual Power Electronics Specialists Conference (IEEE Cat. No. 04CH37551)*, vol. 6. IEEE, 2004, pp. 4819–4824.

[59] A. Sanchez, M. Sanz, P. Alou, R. Prieto, and J. Cobos, "Experimental validation of an optimized piezoelectric transformer design with interleaving of electrodes," in *2004 IEEE 35th Annual Power Electronics Specialists Conference (IEEE Cat. No. 04CH37551)*, vol. 2. IEEE, 2004, pp. 841–846.

[60] A. Sanchez, R. Prieto, M. Sanz, J. Oliver, and J. Cobos, "Modeling and design of piezoelectric transformers for low power applications," in *9th IEEE International Power Electronics Congress, 2004. CIEP 2004.* IEEE, 2004, pp. 15–20.

[61] M. Sanz, A. Sanchez, P. Alou, R. Prieto, J. Cobos, and J. Uceda, "Step by step multilayer piezoelectric transformer design procedure," in *2004 IEEE 35th Annual Power Electronics Specialists Conference (IEEE Cat. No. 04CH37551)*, vol. 6. IEEE, 2004, pp. 4669–4675.

[62] T. Zaitsu, O. Ohnishi, T. Inoue, M. Shoyama, T. Ninomiya, F. Lee, and G. Hua, "Piezoelectric transformer operating in thickness extensional vibration and its application to switching converter," in *Proceedings of 1994 Power Electronics Specialist Conference-PESC'94*, vol. 1. IEEE, 1994, pp. 585–589.

[63] M. Sanz, P. Alou, J. Oliver, R. Prieto, J. Cobos, and J. Uceda, "Interleaving of electrodes in piezoelectric transformers," in *2002 IEEE 33rd Annual IEEE Power Electronics Specialists Conference. Proceedings (Cat. No. 02CH37289)*, vol. 2. IEEE, 2002, pp. 567–572.

[64] M. Sanz, P. Alou, A. Soto, R. Prieto, J. Cobos, and J. Uceda, "Magnetic-less converter based on piezoelectric transformers for step-down dc/dc and low power application," in *Eighteenth Annual IEEE Applied Power Electronics Conference and Exposition, 2003. APEC'03.*, vol. 2. IEEE, 2003, pp. 615–621.

[65] T. Zaitsu, T. Inoue, O. Ohnishi, and A. Iwamoto, "2 mhz power converter with piezoelectric ceramic transformer," in *[Proceedings] Fourteenth International Telecommunications Energy Conference-INTELEC'92*. IEEE, 1992, pp. 430–437.

[66] T. Inoue, O. Ohnishi, and N. Ohde, "Thickness mode vibration piezoelectric transformer," Jun. 2 1992, uS Patent 5,118,982.

[67] J. Navas, T. Bove, J. Cobos, F. Nuno, and K. Brebol, "Miniaturised battery charger using piezoelectric transformers," in *APEC 2001. Sixteenth Annual IEEE Applied Power Electronics Conference and Exposition (Cat. No. 01CH37181)*, vol. 1. IEEE, 2001, pp. 492–496.

[68] K. Brebøl, "Piezoelectric transformer," U.S. Patent 6 707 235, 2004.

[69] E. L. Horsley, "Modelling and analysis of radial mode piezoelectric transformers and inductor-less resonant power converters." Ph.D. dissertation, University of Sheffield, 2011.

[70] R.-L. Lin, *Piezoelectric transformer characterization and application of electronic ballast*. Virginia Polytechnic Institute and State University, 2001.

[71] K. Uchino, S. Priya, S. Ural, A. Vazquez-Carazo, and T. Ezaki, "High power piezoelectric transformers—their applications to smart actuator systems," in *Proceedings of Symposium of Developments in Dielectric Materials and Electronic Devices (Am. Ceram. Soc. 2005)*, 2005, pp. 383–395.

[72] T. Hemsel and S. Priya, "Model based analysis of piezoelectric transformers," *Ultrasonics*, vol. 44, pp. e741–e745, 2006.

[73] S. Priya, S. Ural, H. W. Kim, K. Uchino, and T. Ezaki, "Multilayered unipoled piezoelectric transformers," *Japanese journal of applied physics*, vol. 43, no. 6R, p. 3503, 2004.

[74] S.-T. Ho, "Modeling of a disk-type piezoelectric transformer," *IEEE transactions on ultrasonics, ferroelectrics, and frequency control*, vol. 54, no. 10, pp. 2110–2119, 2007.

[75] E. Munk, "Equivalent electrical circuit for radial modes of a piezoelectric ceramic disc with concentric electrodes," *Philips Research Reports*, vol. 20, no. 2, p. 170, 1965.

[76] M. Guo, D. Lin, K. H. Lam, S. Wang, H. L. Chan, and X. Zhao, "A lead-free piezoelectric transformer in radial vibration modes," *Review of scientific instruments*, vol. 78, no. 3, p. 035102, 2007.

[77] S. Priya, "High power universal piezoelectric transformer," *IEEE transactions on ultrasonics, ferroelectrics, and frequency control*, vol. 53, no. 1, pp. 23–29, 2006.

[78] H. L. Li, J. H. Hu, and H. L. W. Chan, "Finite element analysis on piezoelectric ring transformer," *ieee transactions on ultrasonics, ferroelectrics, and frequency control*, vol. 51, no. 10, pp. 1247–1254, 2004.

[79] S. Choi, T. Kim, S. Lee, and B. H. Cho, "Modeling and characterization of radial-mode disk-type piezoelectric transformer for ac/dc adapter," in *2005 IEEE 36th Power Electronics Specialists Conference*. IEEE, 2005, pp. 624–629.

[80] P. Laoratanakul, A. V. Carazo, P. Bouchilloux, and K. Uchino, "Unipoled disk-type piezoelectric transformers," *Japanese journal of applied physics*, vol. 41, no. 3R, p. 1446, 2002.

[81] P. Plpán and J. Erhart, "Transformation ratio of "ring-dot" planar piezoelectric transformer," *Sensors and Actuators A: Physical*, vol. 140, no. 2, pp. 215–224, 2007.

[82] I. Kim, H. Joo, J. Song, S. Jeong, and M. Kim, "Ring-dot-shaped multilayer piezoelectric step-down transformers using pzt-based ceramics," *Journal of the Korean Physical Society*, vol. 57, no. 41, pp. 963–966, 2010.

[83] M. Guo, K. H. Lam, S. Wang, K. W. Kwok, H. L. Chan, and X. Zhao, "A study on the disk-shaped piezoelectric transformer with multiple outputs," *Review of scientific instruments*, vol. 78, no. 12, p. 125103, 2007.

[84] K.-T. Chang, H.-C. Chiang, and K.-S. Lyu, "Effects of electrode layouts on voltage gain characteristics for ring-shaped piezoelectric transformers," *Sensors and Actuators A: Physical*, vol. 141, no. 1, pp. 166–172, 2008.

[85] J. H. Hu, H. L. Li, H. L. W. Chan, and C. L. Choy, "A ring-shaped piezoelectric transformer operating in the third symmetric extensional vibration mode," *Sensors and Actuators A: Physical*, vol. 88, no. 1, pp. 79–86, 2001.

[86] J. Yoo, K. Yoon, Y. Lee, S. Suh, J. Kim, and C. Yoo, "Electrical characteristics of the contour-vibration-mode piezoelectric transformer with ring/dot electrode area ratio," *Japanese Journal of Applied Physics*, vol. 39, no. 5R, p. 2680, 2000.

[87] M. Yamamoto, Y. Sasaki, A. Ochi, T. Inoue, and S. Hamamura, "Step-down piezoelectric transformer for ac-dc converters," *Japanese Journal of Applied Physics*, vol. 40, no. 5S, p. 3637, 2001.

[88] K. Tseng, J. Du, and J. Hu, "Piezoelectric transformer with high power density and multiple outputs," *Electronics Letters*, vol. 40, no. 12, pp. 786–788, 2004.

[89] J. Hu, K. H. Chan, and B. S. Ng, "Output voltage regulation of a k15 mode piezoelectric transformer by an external l/c component," *Ultrasonics*, vol. 49, no. 6-7, pp. 532–537, 2009.

[90] J. Yang and W. Zhang, "A thickness-shear high voltage piezoelectric transformer," *International Journal of Applied Electromagnetics and Mechanics*, vol. 10, no. 2, pp. 105–121, 1999.

[91] J. Du, J. Hu, and K.-J. Tseng, "High-power, multioutput piezoelectric transformers operating at the thickness-shear vibration mode," *ieee transactions on ultrasonics, ferroelectrics, and frequency control*, vol. 51, no. 5, pp. 502–509, 2004.

[92] J. Du, J. Hu, and K. J. Seng, "Modeling of the dual-output piezoelectric transformer operating at thickness shear vibration mode," in *14th IEEE International Symposium on Applications of Ferroelectrics, 2004. ISAF-04. 2004.* IEEE, 2004, pp. 225–228.

[93] J. Du, J. Hu, K.-J. Tseng, C. S. Kai, and G. C. Siong, "Modeling and analysis of dual-output piezoelectric transformer operating at thickness-shear vibration mode," *IEEE transactions on ultrasonics, ferroelectrics, and frequency control*, vol. 53, no. 3, pp. 579–585, 2006.

[94] J. Yang and X. Zhang, "Analysis of a thickness-shear piezoelectric transformer," *International Journal of Applied Electromagnetics and Mechanics*, vol. 21, no. 2, pp. 131–141, 2005.

[95] M. K. Kahalerras, F. Pigache, J. Regnier, and F. Mosser, "Analyses of temperature influence in piezoelectric transformers dedicated to plasma generation," in *2015 IEEE International Workshop of Electronics, Control, Measurement, Signals and their Application to Mechatronics (ECMSM)*, 2015, pp. 1–5.

[96] R. L. Lin, F. C. Lee, E. M. Baker, and D. Y. Chen, "Inductor-less piezoelectric transformer electronic ballast for linear fluorescent lamp," in *APEC 2001. Sixteenth Annual IEEE Applied Power Electronics Conference and Exposition (Cat. No. 01CH37181)*, vol. 2. IEEE, 2001, pp. 664–669.

[97] T. Ezaki, S. Manuspiya, P. Moses, K. Uchino, and V. Caraz, "Piezoelectric transformers for a high power module," *Materials Technology*, vol. 19, no. 2, pp. 79–83, 2004.

[98] W. Huang, "Design of a radial mode piezoelectric transformer for a charge pump electronic ballast with high power factor and zero voltage switching," Ph.D. dissertation, Virginia Tech, 2003.

[99] E. Horsley, A. Carazo, M. Foster, and D. Stone, "A lumped equivalent circuit model for the radial mode piezoelectric transformer," in *2009 Twenty-Fourth Annual IEEE Applied Power Electronics Conference and Exposition*. IEEE, 2009, pp. 1747–1753.

[100] T. Endow, S. Hirose, and T. Kanno, "Precise measurement of losses in piezoelectric transducer and its application to evaluation of piezoelectric transformer efficiency," *Japanese journal of applied physics*, vol. 43, no. 5S, p. 2976, 2004.

[101] Y. Wang, Y. Yao, X. Liu, D. Xu, and L. Cai, "An lc/s compensation topology and coil design technique for wireless power transfer," *IEEE Transactions on Power Electronics*, vol. 33, no. 3, pp. 2007–2025, 2017.

[102] T. Zaitsu, T. Shigehisa, T. Inoue, M. Shoyama, and T. Ninomiya, "Piezoelectric transformer converter with frequency control," in *Proceedings of INTELEC 95. 17th International Telecommunications Energy Conference*. IEEE, 1995, pp. 175–180.

[103] S. Ben-Yaakov and S. Lineykin, "Maximum power tracking of piezoelectric transformer hv converters under load variations," *IEEE Transactions on power electronics*, vol. 21, no. 1, pp. 73–78, 2006.

[104] S. Nakashima, T. Ninomiya, H. Ogasawara, and H. Kakehashi, "Piezoelectric-transformer inverter with maximum-efficiency tracking and dimming control," in *APEC. Seventeenth Annual IEEE Applied Power Electronics Conference and Exposition (Cat. No. 02CH37335)*, vol. 2. IEEE, 2002, pp. 918–923.

[105] J. M. Alonso, C. Ordiz, and M. A. Dalla Costa, "A novel control method for piezoelectric-transformer based power supplies assuring zero-voltage-switching operation," *IEEE Transactions on Industrial Electronics*, vol. 55, no. 3, pp. 1085–1089, 2008.

[106] J. A. Martin-Ramos, M. A. J. Prieto, F. N. García, J. D. González, and F. F. Linera, "A new full-protected control mode to drive piezoelectric transformers in dc-dc converters," *IEEE Transactions on Power Electronics*, vol. 17, no. 6, pp. 1096–1103, 2002.

[107] J. Diaz, J. Martin-Ramos, M. Prieto, and F. Nuno, "A double-closed loop dc/dc converter based on a piezoelectric transformer," in *Nineteenth Annual IEEE Applied Power Electronics Conference and Exposition, 2004. APEC'04.*, vol. 3. IEEE, 2004, pp. 1423–1428.

[108] M. Khanna, R. Burgos, Q. Wang, K. D. Ngo, and A. V. Carazo, "New tunable piezoelectric transformers and their application in dc–dc converters," *IEEE Transactions on Power Electronics*, vol. 32, no. 12, pp. 8974–8978, 2017.

[109] M. Khanna, "Design of dc-dc converters using tunable piezoelectric transformers," Ph.D. dissertation, Virginia Tech, 2017.

[110] R. L. Steigerwald, "A comparison of half-bridge resonant converter topologies," *IEEE transactions on Power Electronics*, vol. 3, no. 2, pp. 174–182, 1988.

[111] S. Chung, B. Kang, and M. Kim, "Constant frequency control of llc resonant converter using switched capacitor," *Electronics Letters*, vol. 49, no. 24, pp. 1556–1558, 2013.

[112] D. Maksimovic and S. Cuk, "Switching converters with wide dc conversion range," *IEEE Transactions on Power Electronics*, vol. 6, no. 1, pp. 151–157, 1991.

[113] K. Karaket and C. Bunlaksananusorn, "Modeling of a quadratic buck converter," in *The 8th Electrical Engineering/Electronics, Computer, Telecommunications and Information Technology (ECTI) Association of Thailand-Conference 2011.* IEEE, 2011, pp. 764–767.

[114] O. Pelan, N. Muntean, O. Cornea, and F. Blaabjerg, "High voltage conversion ratio, switched c & l cells, step-down dc-dc converter," in *2013 IEEE Energy Conversion Congress and Exposition.* IEEE, 2013, pp. 5580–5585.

[115] B. Axelrod, Y. Berkovich, and A. Ioinovici, "Switched-capacitor/switched-inductor structures for getting transformerless hybrid dc–dc pwm converters," *IEEE Transactions on Circuits and Systems I: Regular Papers*, vol. 55, no. 2, pp. 687–696, 2008.

[116] C.-F. Chuang, C.-T. Pan, and H.-C. Cheng, "A novel transformer-less interleaved four-phase step-down dc converter with low switch voltage stress and automatic uniform current-sharing characteristics," *IEEE Transactions on Power Electronics*, vol. 31, no. 1, pp. 406–417, 2015.

[117] M. Esteki, B. Poorali, E. Adib, and H. Farzanehfard, "Interleaved buck converter with continuous input current, extremely low output current ripple, low switching losses, and improved step-down conversion ratio," *IEEE transactions on industrial electronics*, vol. 62, no. 8, pp. 4769–4776, 2015.

[118] C.-T. Pan, C.-F. Chuang, and C.-C. Chu, "A novel transformerless interleaved high step-down conversion ratio dc–dc converter with low switch voltage stress," *IEEE transactions on industrial electronics*, vol. 61, no. 10, pp. 5290–5299, 2014.

[119] Y.-T. Yau, W.-Z. Jiang, and K.-I. Hwu, "Step-down converter with wide voltage conversion ratio," *IET Power Electronics*, vol. 8, no. 11, pp. 2136–2144, 2015.

[120] J. A. Reyes-Malanche, N. Vázquez, and J. Leyva-Ramos, "Switched-capacitor quadratic buck converter for wider conversion ratios," *IET Power Electronics*, vol. 8, no. 12, pp. 2370–2376, 2015.

[121] R. Khambuya and S. Khwan-on, "A new high step-down dc-dc converter for renewable energy system applications," *Procedia Computer Science*, vol. 86, pp. 349–352, 2016.

[122] K. Hwu, W. Jiang, and Y. Yau, "Ultrahigh step-down converter," *IEEE Transactions on Power Electronics*, vol. 30, no. 6, pp. 3262–3274, 2014.

[123] D. Cheshmdehmam, E. Adib, and H. Farzanehfard, "Soft-switched nonisolated high step-down converter," *IEEE transactions on industrial electronics*, vol. 66, no. 1, pp. 183–190, 2018.

[124] M. Hajiheidari, H. Farzanehfard, and E. Adib, "High-step-down dc–dc converter with continuous output current using coupled-inductors," *IEEE Transactions on Power Electronics*, vol. 34, no. 11, pp. 10 936–10 944, 2019.

[125] K. Yao, M. Ye, M. Xu, and F. C. Lee, "Tapped-inductor buck converter for high-step-down dc-dc conversion," *IEEE Transactions on Power Electronics*, vol. 20, no. 4, pp. 775–780, 2005.

[126] G. Rizzoli, L. Zarri, J. Wang, Z. Shen, R. Burgos, and D. Boroyevich, "Design of a two-switch flyback power supply using 1.7 kv sic devices for ultra-wide input-voltage range applications," in *2016 IEEE Energy Conversion Congress and Exposition (ECCE)*. IEEE, 2016, pp. 1–5.

[127] F. Z. Peng, "A generalized multilevel inverter topology with self voltage balancing," *IEEE Transactions on industry applications*, vol. 37, no. 2, pp. 611–618, 2001.

[128] H. D. Torresan, D. Holmes, and I. Shraga, "Auxiliary power supplies for high voltage converter systems," in *2004 IEEE 35th Annual Power Electronics Specialists Conference (IEEE Cat. No. 04CH37551)*, vol. 1. IEEE, 2004, pp. 645–651.

[129] H. Torresan and D. Holmes, "A high voltage converter for auxiliary supply applications using a reduced flying capacitor topology," in *2005 IEEE 36th Power Electronics Specialists Conference*. IEEE, 2005, pp. 1220–1226.

[130] F. Z. Peng, W. Qian, and D. Cao, "Recent advances in multilevel converter/inverter topologies and applications," in *The 2010 International Power Electronics Conference-ECCE ASIA-*. IEEE, 2010, pp. 492–501.

[131] R. Giri, V. Choudhary, R. Ayyanar, and N. Mohan, "Common-duty-ratio control of input-series connected modular dc-dc converters with active input voltage and load-current sharing," *IEEE Transactions on Industry Applications*, vol. 42, no. 4, pp. 1101–1111, 2006.

[132] R. Ayyanar, R. Giri, and N. Mohan, "Active input-voltage and load-current sharing in input-series and output-parallel connected modular dc-dc converters using dynamic input-voltage reference scheme," *IEEE Transactions on Power Electronics*, vol. 19, no. 6, pp. 1462–1473, 2004.

[133] W. Chen, K. Zhuang, and X. Ruan, "A input-series-and output-parallel-connected inverter system for high-input-voltage applications," *IEEE Transactions on Power Electronics*, vol. 24, no. 9, pp. 2127–2137, 2009.

[134] W. Chen, G. Wang, X. Ruan, W. Jiang, and W. Gu, "Wireless input-voltage-sharing control strategy for input-series output-parallel (isop) system based on positive output-voltage gradient method," *IEEE Transactions on Industrial Electronics*, vol. 61, no. 11, pp. 6022–6030, 2014.

[135] A. J. Bottion and I. Barbi, "Input-series and output-series connected modular output capacitor full-bridge pwm dc–dc converter," *IEEE Transactions on Industrial Electronics*, vol. 62, no. 10, pp. 6213–6221, 2015.

[136] J.-W. Kim, J.-S. Yon, and B. Cho, "Modeling, control, and design of input-series-output-parallel-connected converter for high-speed-train power system," *IEEE Transactions on industrial electronics*, vol. 48, no. 3, pp. 536–544, 2001.

[137] T. Meng, C. Li, H. Ben, and J. Zhao, "An input-series flyback auxiliary power supply scheme based on transformer-integration for high-input voltage applications," *IEEE Transactions on Power Electronics*, vol. 31, no. 9, pp. 6383–6393, 2015.

[138] T. Meng, Y. Song, Z. Wang, H. Ben, and C. Li, "Investigation and implementation of an input-series auxiliary power supply scheme for high-input-voltage low-power applications," *IEEE Transactions on Power Electronics*, vol. 33, no. 1, pp. 437–447, 2017.

[139] A. Rodriguez, M. R. Rogina, M. Saeed, D. G. Lamar, M. Arias, M. Lopez, and F. Briz, "Auxiliary power supply based on a modular isop flyback configuration with very high

input voltage," in *2016 IEEE Energy Conversion Congress and Exposition (ECCE)*. IEEE, 2016, pp. 1–7.

[140] H. Schmidt and C. Siedle, "The charge equalizer-a new system to extend battery lifetime in photovoltaic systems, ups and electric vehicles," in *Proceedings of Intelec 93: 15th International Telecommunications Energy Conference*, vol. 2. IEEE, 1993, pp. 146–151.

[141] N. H. Kutkut, "A modular nondissipative current diverter for ev battery charge equalization," in *APEC'98 Thirteenth Annual Applied Power Electronics Conference and Exposition*, vol. 2. IEEE, 1998, pp. 686–690.

[142] F. H. Khan and L. M. Tolbert, "A multilevel modular capacitor-clamped dc–dc converter," *IEEE Transactions on Industry Applications*, vol. 43, no. 6, pp. 1628–1638, 2007.

[143] M. D. Seeman and S. R. Sanders, "Analysis and optimization of switched-capacitor dc–dc converters," *IEEE transactions on power electronics*, vol. 23, no. 2, pp. 841–851, 2008.

[144] K. Sano and H. Fujita, "Voltage-balancing circuit based on a resonant switched-capacitor converter for multilevel inverters," *IEEE Transactions on industry applications*, vol. 44, no. 6, pp. 1768–1776, 2008.

[145] J. Liu, S. Zhong, J. Zhang, Y. Ai, N. Zhao, and J. Yang, "Auxiliary power supply for medium-/high-voltage and high-power solid-state transformers," *IEEE Transactions on Power Electronics*, vol. 35, no. 5, pp. 4791–4803, 2019.

[146] M. Kasper, D. Bortis, and J. W. Kolar, "Novel high voltage conversion ratio "rainstick" dc/dc converters," in *2013 IEEE Energy Conversion Congress and Exposition*. IEEE, 2013, pp. 789–796.

[147] K. Sun, X. Lin, J. Wang, R. Burgos, and D. Boroyevich, "A scalable voltage-balancing-circuit based non-isolated high-step-down-ratio auxiliary power supply," in *2021 IEEE Applied Power Electronics Conference and Exposition (APEC)*. IEEE, 2021, pp. 1803–1808.

[148] H. Kim, A. Brockhaus, and J. Engemann, "Atmospheric pressure argon plasma jet using a cylindrical piezoelectric transformer," *Applied Physics Letters*, vol. 95, no. 21, p. 211501, 2009.

[149] Y.-K. Lo and K.-J. Pai, "Feedback design of a piezoelectric transformer-based half-bridge resonant ccfl inverter," in *2007 International Aegean Conference on Electrical Machines and Power Electronics*. IEEE, 2007, pp. 162–167.

[150] B. Cai, X. Shao, Y. Liu, X. Kong, H. Wang, H. Xu, and W. Ge, "Remaining useful life estimation of structure systems under the influence of multiple causes: Subsea pipelines as a case study," *IEEE Transactions on Industrial Electronics*, vol. 67, no. 7, pp. 5737–5747, 2019.

[151] P. Fang and Y.-F. Liu, "A innovative current sensor-less continuous conduction mode pfc control," in *2013 IEEE Energy Conversion Congress and Exposition*. IEEE, 2013, pp. 2155–2161.

[152] C. Aprea, A. Greco, and A. Maiorino, "Modelling an active magnetic refrigeration system: a comparison with different models of incompressible flow through a packed bed," *Applied Thermal Engineering*, vol. 36, pp. 296–306, 2012.

[153] C. Aprea, A. Greco, A. Maiorino, R. Mastrullo, and A. Tura, "Initial experimental results from a rotary permanent magnet magnetic refrigerator," *International journal of refrigeration*, vol. 43, pp. 111–122, 2014.

[154] C. Aprea, A. Greco, A. Maiorino, and C. Masselli, "The energy performances of a rotary permanent magnet magnetic refrigerator," *International Journal of Refrigeration*, vol. 61, pp. 1–11, 2016.

[155] B. Yu, Q. Gao, B. Zhang, X. Meng, and Z. Chen, "Review on research of room temperature magnetic refrigeration," *International Journal of Refrigeration*, vol. 26, no. 6, pp. 622–636, 2003.

[156] B. Yu, M. Liu, P. W. Egolf, and A. Kitanovski, "A review of magnetic refrigerator and heat pump prototypes built before the year 2010," *International Journal of refrigeration*, vol. 33, no. 6, pp. 1029–1060, 2010.

[157] K. K. Nielsen, J. Tusek, K. Engelbrecht, S. Schopfer, A. Kitanovski, C. R. H. Bahl, A. Smith, N. Pryds, and A. Poredos, "Review on numerical modeling of active magnetic regenerators for room temperature applications," *International Journal of Refrigeration*, vol. 34, no. 3, pp. 603–616, 2011.

[158] A. Kitanovski and P. W. Egolf, "Thermodynamics of magnetic refrigeration," *International Journal of Refrigeration*, vol. 29, no. 1, pp. 3–21, 2006.

[159] A. Kitanovski, U. Plaznik, U. Tomc, and A. Poredoš, "Present and future caloric refrigeration and heat-pump technologies," *International Journal of Refrigeration*, vol. 57, pp. 288–298, 2015.

[160] A. Kitanovski, J. Tušek, U. Tomc, U. Plaznik, M. Ožbolt, and A. Poredoš, "Magnetic field sources," in *Magnetocaloric Energy Conversion*. Springer, 2015, pp. 39–95.

[161] J. Tušek and A. Kitanovski, "Magnetocaloric energy conversion: From theory to applications," 2015.

[162] C. Aprea, A. Greco, A. Maiorino, and C. Masselli, "A comparison between different materials in an active electrocaloric regenerative cycle with a 2d numerical model," *International Journal of Refrigeration*, vol. 69, pp. 369–382, 2016.

[163] A. Mischenko, Q. Zhang, J. Scott, R. Whatmore, and N. Mathur, "Giant electrocaloric effect in thin-film pbzr0. 95ti0. 05o3," *Science*, vol. 311, no. 5765, pp. 1270–1271, 2006.

[164] B. Neese, B. Chu, S.-G. Lu, Y. Wang, E. Furman, and Q. Zhang, "Large electrocaloric effect in ferroelectric polymers near room temperature," *Science*, vol. 321, no. 5890, pp. 821–823, 2008.

[165] A. Mielke and A. M. Timofte, "Modeling and analytical study for ferroelectric materials," *Mechanics of Advanced Materials and Structures*, vol. 13, no. 6, pp. 457–462, 2006.

[166] G. Suchaneck, "Upper bounds in electrocaloric cooling," in *2016 Joint IEEE International Symposium on the Applications of Ferroelectrics, European Conference on Application of Polar Dielectrics, and Piezoelectric Force Microscopy Workshop (ISAF/ECAPD/PFM)*. IEEE, 2016, pp. 1–4.

[167] H. Gu, X. Li, S. Lu, M. Lin, X. Qian, J. Cheng, Q. Zhang, A. Cheng, and B. Craven, "Compact cooling devices based on giant electrocaloric effect dielectrics," in *Heat Transfer Summer Conference*, vol. 44786. American Society of Mechanical Engineers, 2012, pp. 635–639.

[168] K. Brahim, C. Younes, H. Noureddine, and T. Abdelhalim, "Electrocaloric refrigeration near room temperature," in *2018 International Conference on Applied Smart Systems (ICASS)*. IEEE, 2018, pp. 1–4.

[169] G. Akcay, S. Alpay, J. Mantese, G. Rossetti, and J. Scott, "Electrocaloric response of the ferroelectrics," in *2008 17th IEEE International Symposium on the Applications of Ferroelectrics*, vol. 2. IEEE, 2008, pp. 1–4.

[170] Y.-B. Ma, K. Albe, and B.-X. Xu, "Monte carlo simulations of the electrocaloric effect in relaxor ferroelectrics," in *2015 Joint IEEE International Symposium on the Applications of Ferroelectric (ISAF), International Symposium on Integrated Functionalities (ISIF), and Piezoelectric Force Microscopy Workshop (PFM)*. IEEE, 2015, pp. 203–206.

[171] I. A. Starkov, A. S. Anokhin, and A. S. Starkov, "Pulse shape effects in electrocaloric cooling," *IEEE Transactions on Ultrasonics, Ferroelectrics, and Frequency Control*, vol. 68, no. 3, pp. 865–871, 2020.

[172] Y. Wang, D. E. Schwartz, S. J. Smullin, Q. Wang, and M. J. Sheridan, "Silicon heat switches for electrocaloric cooling," *Journal of Microelectromechanical Systems*, vol. 26, no. 3, pp. 580–587, 2017.

[173] A. Khodayari and S. Mohammadi, "Solid-state cooling line based on the electrocaloric effect," *IEEE transactions on ultrasonics, ferroelectrics, and frequency control*, vol. 58, no. 3, pp. 503–508, 2011.

[174] H. Gu, X. Qian, X. Li, B. Craven, W. Zhu, A. Cheng, S. Yao, and Q. Zhang, "A chip scale electrocaloric effect based cooling device," *Applied Physics Letters*, vol. 102, no. 12, p. 122904, 2013.

[175] Y. Wang, S. Smullin, M. Sheridan, Q. Wang, C. Eldershaw, and D. Schwartz, "A heat-switch-based electrocaloric cooler," *Applied Physics Letters*, vol. 107, no. 13, p. 134103, 2015.

[176] Y. Jia and Y. Sungtaek Ju, "A solid-state refrigerator based on the electrocaloric effect," *Applied Physics Letters*, vol. 100, no. 24, p. 242901, 2012.

[177] D. Guo, "Design, analysis, modeling and testing of a micro-scale refrigeration system," Ph.D. dissertation, Carnegie Mellon University, 2014.

[178] A. Torelló, P. Lheritier, T. Usui, Y. Nouchokgwe, M. Gérard, O. Bouton, S. Hirose, and E. Defay, "Giant temperature span in electrocaloric regenerator," *Science*, vol. 370, no. 6512, pp. 125–129, 2020.

[179] U. Plaznik, M. Vrabelj, Z. Kutnjak, B. Malič, B. Rožič, A. Poredoš, and A. Kitanovski, "Numerical modelling and experimental validation of a regenerative electrocaloric cooler," *International journal of refrigeration*, vol. 98, pp. 139–149, 2019.

[180] C. Wang, "Theories and methods of first order ferroelectric phase transitions," *Ferroelectrics*, 2010.

[181] D. Li and S. Lu, "Electrocaloric effect and phase transitions in ferroelectrics," *Int. J. Metall. Mater. Eng.*, vol. 4, no. 1, 2018.

[182] T. Correlia and Q. Zhang, "Electrocaloric materials: new generation of coolers," 2014.

[183] A. Bhalla, K. Nair, I. Lloyd, H. Yanagida, and D. Payne, "Ceramic transactions: Ferroic materials-design, preparation, and characteristics. volume 43," American Ceramic Society, Westerville, OH (United States), Tech. Rep., 1994.

[184] R. Cowley and G. Coombs, "Paraelectric, piezoelectric and pyroelectric crystals: Ii phase transitions," *Journal of Physics C: Solid State Physics*, vol. 6, no. 1, p. 143, 1973.

[185] A. L. Kholkin, N. A. Pertsev, and A. V. Goltsev, "Piezoelectricity and crystal symmetry," in *Piezoelectric and Acoustic Materials for Transducer Applications*. Springer, 2008, pp. 17–38.

[186] X. Li, S.-G. Lu, X.-Z. Chen, H. Gu, X.-s. Qian, and Q. Zhang, "Pyroelectric and electrocaloric materials," in *Progress in Advanced Dielectrics*. World Scientific, 2020, pp. 329–367.

[187] Y. Liu, J. F. Scott, and B. Dkhil, "Some strategies for improving caloric responses with ferroelectrics," *APL Materials*, vol. 4, no. 6, p. 064109, 2016.

[188] L. Wang, J. Yu, Y. Wang, G. Peng, F. Liu, and J. Gao, "Modeling ferroelectric capacitors based on the dipole switching theory," *Journal of applied physics*, vol. 101, no. 10, p. 104505, 2007.

[189] C.-g. Wei, T.-l. Ren, D. Xie, Z.-G. Zhang, J. Zhu, and L.-T. Liu, "A ferroelectric capacitor compact model for circuit simulation," in *Proceedings. 7th International Conference on Solid-State and Integrated Circuits Technology, 2004.*, vol. 1. IEEE, 2004, pp. 738–741.

[190] A. Sheikholeslami and P. G. Gulak, "A survey of behavioral modeling of ferroelectric capacitors," *IEEE transactions on ultrasonics, ferroelectrics, and frequency control*, vol. 44, no. 4, pp. 917–924, 1997.

[191] S. Sherrit, "Analytical model for the strain-field and polarization-field hysteresis curves for ferroic materials," in *Behavior and Mechanics of Multifunctional and Composite Materials 2007*, vol. 6526. International Society for Optics and Photonics, 2007, p. 652608.

[192] S. Miller, R. Nasby, J. Schwank, M. Rodgers, and P. Dressendorfer, "Device modeling of ferroelectric capacitors," *Journal of applied physics*, vol. 68, no. 12, pp. 6463–6471, 1990.

[193] E. Supriyanto, I. Schultz, M. Ullmann, and H. Goebel, "Ferroelectric capacitor compact model including dynamic and temperature behavior," in *Proceedings of the 13th IEEE International Symposium on Applications of Ferroelectrics, 2002. ISAF 2002.* IEEE, 2002, pp. 61–64.

[194] G. Sebald, L. Lebrun, and D. Guyomar, "Modeling of elastic nonlinearities in ferroelectric materials including nonlinear losses: application to nonlinear resonance mode of relaxors single crystals," *IEEE transactions on ultrasonics, ferroelectrics, and frequency control*, vol. 52, no. 4, pp. 596–603, 2005.

[195] C. G. Namboodri, "Experimental investigation and modeling of the electrostrictive relaxor ferroelectric lead magnesium niobate-lead titinate," Ph.D. dissertation, Virginia Tech, 1992.

[196] T. Liu, *Electromechanical behavior of relaxor ferroelectric crystals.* Georgia Institute of Technology, 2004.

[197] D. Szwagierczak and J. Kulawik, "Thick film capacitors with relaxor dielectrics," *Journal of the European Ceramic Society*, vol. 24, no. 7, pp. 1979–1985, 2004.

[198] C. L. Hom and N. Shankar, "Modeling time-dependent behavior in relaxor ferroelectrics," in *Smart Structures and Materials 1998: Mathematics and Control in Smart Structures*, vol. 3323. International Society for Optics and Photonics, 1998, pp. 287–298.

[199] Z.-Y. Cheng, R. Katiyar, X. Yao, and A. Bhalla, "Temperature dependence of the dielectric constant of relaxor ferroelectrics," *Physical Review B*, vol. 57, no. 14, p. 8166, 1998.

[200] L. Yang, X. Li, E. Allahyarov, P. L. Taylor, Q. Zhang, and L. Zhu, "Novel polymer ferroelectric behavior via crystal isomorphism and the nanoconfinement effect," *Polymer*, vol. 54, no. 7, pp. 1709–1728, 2013.

[201] M. Acosta, *Strain mechanisms in lead-free ferroelectrics for actuators.* Springer, 2016.

[202] C. W. Ahn, C.-H. Hong, B.-Y. Choi, H.-P. Kim, H.-S. Han, Y. Hwang, W. Jo, K. Wang, J.-F. Li, J.-S. Lee *et al.*, "A brief review on relaxor ferroelectrics and selected issues in

lead-free relaxors," *Journal of the Korean Physical Society*, vol. 68, no. 12, pp. 1481–1494, 2016.

[203] N. Novak and Z. Kutnjak, "Calorimetric study of field-induced ferroelectric transition in pb (mg 1/3 nb 2/3) o 3 relaxor ferroelectrics," in *Proceedings of ISAF-ECAPD-PFM 2012*. IEEE, 2012, pp. 1–4.

[204] A. A. Bokov and Z.-G. Ye, "Dielectric relaxation in relaxor ferroelectrics," *Journal of Advanced dielectrics*, vol. 2, no. 02, p. 1241010, 2012.

[205] N. Novak, R. Pirc, and Z. Kutnjak, "Diffuse critical point in plzt ceramics," *EPL (Europhysics Letters)*, vol. 102, no. 1, p. 17003, 2013.

[206] S. Zhang, C. Huang, R. Klein, F. Xia, D. Jeong, K. Ren, Q. Zhang, and F. Bauer, "Dynamics in relaxor ferroelectric polymers," in *14th IEEE International Symposium on Applications of Ferroelectrics, 2004. ISAF-04. 2004.* IEEE, 2004, pp. 138–142.

[207] R. Pirc, Z. Kutnjak, R. Blinc, and Q. Zhang, "Electrocaloric effect in relaxor ferroelectrics," *Journal of Applied Physics*, vol. 110, no. 7, p. 074113, 2011.

[208] A. Bokov and Z.-G. Ye, "Recent progress in relaxor ferroelectrics with perovskite structure," *Progress in Advanced Dielectrics*, pp. 105–164, 2020.

[209] J. Hao, Z. Xu, R. Chu, W. Li, P. Fu, and J. Du, "Field-induced large strain in lead-free (bi0. 5na0. 5) 1- xbaxti0. 98 (fe0. 5ta0. 5) 0.02 o3 piezoelectric ceramics," *Journal of Alloys and Compounds*, vol. 677, pp. 96–104, 2016.

[210] X. Qian, H.-J. Ye, T. Yang, W.-Z. Shao, L. Zhen, E. Furman, L.-Q. Chen, and Q. Zhang, "Internal biasing in relaxor ferroelectric polymer to enhance the electrocaloric effect," *Advanced Functional Materials*, vol. 25, no. 32, pp. 5134–5139, 2015.

[211] Y. Zhu, Y. Zhang, B. Xie, P. Fan, M. A. Marwat, W. Ma, C. Wang, B. Yang, J. Xiao, and H. Zhang, "Large electric field-induced strain in agnbo3-modified 0.76 bi0. 5na0. 5tio3-0.24 srtio3 lead-free piezoceramics," *Ceramics International*, vol. 44, no. 7, pp. 7851–7857, 2018.

[212] F. Li, S. Zhang, D. Damjanovic, L.-Q. Chen, and T. R. Shrout, "Local structural heterogeneity and electromechanical responses of ferroelectrics: learning from relaxor ferroelectrics," *Advanced Functional Materials*, vol. 28, no. 37, p. 1801504, 2018.

[213] H. Kliem and A. Leschhorn, "Modeling relaxor characteristics in systems of interacting dipoles," *Physica B: Condensed Matter*, vol. 503, pp. 167–173, 2016.

[214] H.-M. Bao, J.-F. Song, J. Zhang, Q.-D. Shen, C.-Z. Yang, and Q. Zhang, "Phase transitions and ferroelectric relaxor behavior in p (vdf- trfe- cfe) terpolymers," *Macromolecules*, vol. 40, no. 7, pp. 2371–2379, 2007.

[215] A. Zaman, Y. Iqbal, A. Hussain, M. Kim, and R. Malik, "Dielectric, ferroelectric, and field-induced strain properties of ta-doped 0.99 bi 0.5 (na 0.82 k 0.18) 0.5 tio 3–0.01 lisbo 3 ceramics," *Journal of Materials Science*, vol. 49, no. 8, pp. 3205–3214, 2014.

[216] R. Cowley, S. Gvasaliya, S. Lushnikov, B. Roessli, and G. Rotaru, "Relaxing with relaxors: a review of relaxor ferroelectrics," *Advances in Physics*, vol. 60, no. 2, pp. 229–327, 2011.

[217] X. Jian, X. Chen, and Q. Zhang, "Relaxor ferroelectric capacitors embrace polymorphic nanodomains," *Joule*, vol. 3, no. 10, pp. 2296–2298, 2019.

[218] W. Kleemann, "The relaxor enigma—charge disorder and random fields in ferroelectrics," in *Frontiers of ferroelectricity*. Springer, 2006, pp. 129–136.

[219] L.-L. Zhang and Y.-N. Huang, "Theory of relaxor-ferroelectricity," *Scientific reports*, vol. 10, no. 1, pp. 1–18, 2020.

[220] M. Hoffmann, F. P. Fengler, M. Herzig, T. Mittmann, B. Max, U. Schroeder, R. Negrea, P. Lucian, S. Slesazeck, and T. Mikolajick, "Unveiling the double-well energy landscape in a ferroelectric layer," *Nature*, vol. 565, no. 7740, pp. 464–467, 2019.

[221] W. Dong, "Characterization, modeling, and energy harvesting of phase transformations in ferroelectric materials," Ph.D. dissertation, UCLA, 2015.

[222] H. Ku and C. Shin, "Transient response of negative capacitance in p (vdf 0.75-trfe 0.25) organic ferroelectric capacitor," *IEEE Journal of the Electron Devices Society*, vol. 5, no. 3, pp. 232–236, 2017.

[223] B. Chu, *PVDF-based copolymers, terpolymers and their multi-component material systems for capacitor applications*. The Pennsylvania State University, 2008.

[224] E. Defay, S. Crossley, S. Kar-Narayan, X. Moya, and N. D. Mathur, "The electrocaloric efficiency of ceramic and polymer films," *Advanced Materials*, vol. 25, no. 24, pp. 3337–3342, 2013.

[225] X. Moya, E. Stern-Taulats, S. Crossley, D. González-Alonso, S. Kar-Narayan, A. Planes, L. Mañosa, and N. D. Mathur, "Giant electrocaloric strength in single-crystal batio3," *Advanced materials*, vol. 25, no. 9, pp. 1360–1365, 2013.

[226] M. C. Rose and R. E. Cohen, "Giant electrocaloric effect around t c," *Physical review letters*, vol. 109, no. 18, p. 187604, 2012.

[227] R. Pirc, B. Rožič, Z. Kutnjak, R. Blinc, X. Li, and Q. Zhang, "Electrocaloric effect and dipolar entropy change in ferroelectric polymers," *Ferroelectrics*, vol. 426, no. 1, pp. 38–44, 2012.

[228] S.-G. Lu and Q. Zhang, "Large electrocaloric effect in relaxor ferroelectrics," *Journal of Advanced Dielectrics*, vol. 2, no. 03, p. 1230011, 2012.

[229] H. Gu, X.-S. Qian, H.-J. Ye, and Q. Zhang, "An electrocaloric refrigerator without external regenerator," *Applied Physics Letters*, vol. 105, no. 16, p. 162905, 2014.

[230] R. A. Osman and A. R. West, "Electrical characterization and equivalent circuit analysis of (bi1. 5zn0. 5)(nb0. 5ti1. 5) o7 pyrochlore, a relaxor ceramic," *Journal of Applied Physics*, vol. 109, no. 7, p. 074106, 2011.

[231] N. Tsutsumi, K. Okumachi, K. Kinashi, and W. Sakai, "Re-evaluation of the origin of relaxor ferroelectricity in vinylidene fluoride terpolymers: An approach using switching current measurements," *Scientific reports*, vol. 7, no. 1, pp. 1–7, 2017.

[232] D. E. Dunn, "A ferroelectric capacitor macromodel and parameterization algorithm for spice simulation," *IEEE transactions on ultrasonics, ferroelectrics, and frequency control*, vol. 41, no. 3, pp. 360–369, 1994.

[233] A. Sheikholeslami and P. G. Gulak, "Transient modeling of ferroelectric capacitors for nonvolatile memories," *IEEE transactions on ultrasonics, ferroelectrics, and frequency control*, vol. 43, no. 3, pp. 450–456, 1996.

[234] C. B. Sawyer and C. Tower, "Rochelle salt as a dielectric," *Physical review*, vol. 35, no. 3, p. 269, 1930.

[235] A. Odon, "Processing of signal of pyroelectric sensor in laser energy meter," *Measurement Science Review*, vol. 1, no. 1, pp. 215–218, 2001.

[236] A. Thakre, A. Kumar, H.-C. Song, D.-Y. Jeong, and J. Ryu, "Pyroelectric energy conversion and its applications—flexible energy harvesters and sensors," *Sensors*, vol. 19, no. 9, p. 2170, 2019.

[237] J. Xie, X. Mane, C. Green, K. Mossi, and K. K. Leang, "Performance of thin piezoelectric materials for pyroelectric energy harvesting," *Journal of Intelligent Material Systems and Structures*, vol. 21, no. 3, pp. 243–249, 2010.